Inertial Sensor Motion Tracking

A method development and validation study on measurement of baseball pitching

Maryam Sharify

TU Delft

Inertial Sensor Motion Tracking

A method development and validation study on measurement of baseball pitching

MASTER OF SCIENCE THESIS

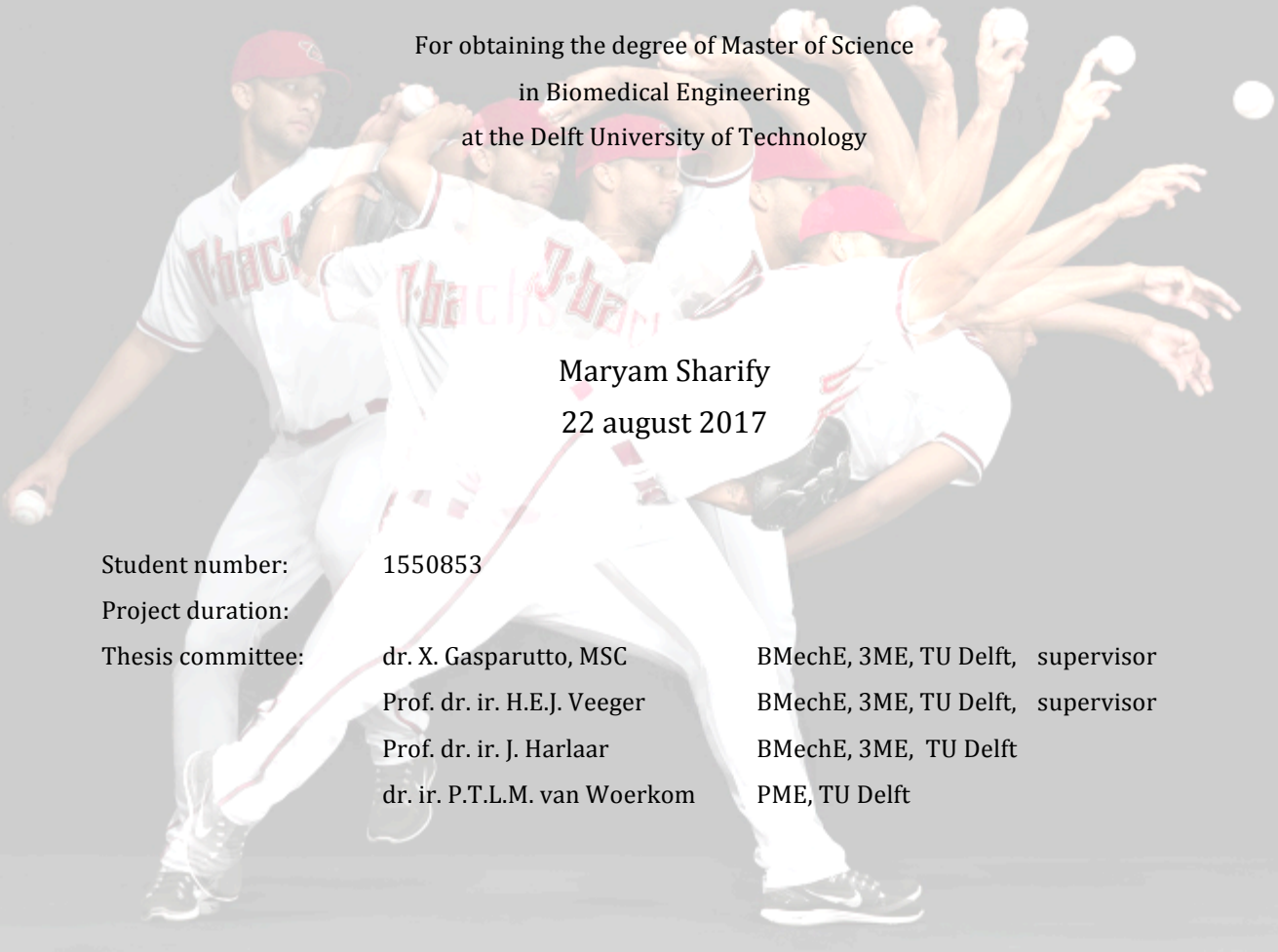

For obtaining the degree of Master of Science
in Biomedical Engineering
at the Delft University of Technology

Maryam Sharify

22 august 2017

Student number:	1550853	
Project duration:		
Thesis committee:	dr. X. Gasparutto, MSC	BMechE, 3ME, TU Delft, supervisor
	Prof. dr. ir. H.E.J. Veeger	BMechE, 3ME, TU Delft, supervisor
	Prof. dr. ir. J. Harlaar	BMechE, 3ME, TU Delft
	dr. ir. P.T.L.M. van Woerkom	PME, TU Delft

TU Delft

Summary

The recent advancements in inertial sensors technology and its promising results in motion tracking, catch the expert's eyes to these new horizons in sports engineering. In baseball, which is the interest of this study, almost 90% of the pitchers got injured once a year due to wrong training and pitching techniques. Screening and real-time feedback to players would help them to improve their training procedures and safely increase their pitching performance.

In the last decades many researches have been carried out on employing this new tool in field measurements, instead of the common marker-based motion tracking with their complexity for the in field measurements. Although it is promising that inertial sensors are the future of motion tracking systems in this area, there are still many technical issues like, IMU sensors measurement limit, drift and bias. Besides in human motion tracking which involves multiple IMU sensors, coinciding the sensors and defining a global coordinate system requires substantial concerns.

This study focuses on developing a valid motion tracking method for the baseball pitchers, having a marker-based motion capture measurement as the reference. In order to be able to do this first of all the two systems was needed to be synchronized and at the same time be able to record the same motion. Secondly, the measurements should be defined in the same coordinate system. For this purpose, a simple functional calibration method has been developed and applied on both systems. This method is validated against a previous method (Seel, Schauer et al. 2012). Finally, The kinematic results are estimated at joint and segment's angles, velocities and accelerations levels. The joint and segment's angles computed by IMU sensors are validated based on marker-based measurements. The sensitivity of IMU-based measurements in estimating the angular velocity and acceleration of movements with different rate of movements (slow vs. fast) is investigated. It has been observed that for baseball pitching applications, IUM sensors with less mass and wider range of measurements are required.

In order to compare the dynamics of the human body, a scalable anthropometric model from the literature is used to define the mass and inertia properties of the segments. An inverse dynamics method is used to compute the kinetics energy and finally the power flow in the segments and joints. Again, all these results from the IMU measurements are compared with the Marker-based method. The advantages and disadvantages of the IMU according to these results are discussed to establish a practical protocol for future measurements and data analysis. One of the major issues in the dynamic analysis is that for translating the velocity from IMU to human body, the measurement protocol needs to provide a known starting and ending velocity. This is done by starting and ending the measurements from a standing position.

The method of this project can be used in baseball pitching motion tracking using the suggested protocol improvements and more advanced IMU sensors.

Acknowledgements

Starting studying at TU Delft was for me a chance to make a better version of myself. The last years of my life in the Netherlands have been an utter metamorphosis. In this moderate evaluation of proficiency so many people have inspired me who I need to thank. And since this may be one and only opportunity to thank them all in a semi-public way, then I must take the opportunity to do so.

Naturally, my primary and sincere thanks go to my advisors, Xavier Gasparutto for his patient support and professional mentorship and Dirk Jan Veeger for being not only my supervisor who I benefited his expert comments during my thesis but also his kindness, sympathetic and encouragement. Beyond that, I would like to thank Paul van Woerkom for his revision and comments, which his positive view is inspiring. Also I would like to thank Jaap Harlaar for giving me a possible future career opportunity at TU Delft. Many thanks are owed to Arend Schwab who I was lucky being his teaching assistant a couple of years for Multibody dynamics B course and later during my thesis he provides me a place in his bicycle lab and did support me to the end of my thesis. They all helped me develop a true passion for science and education.

During my study I also got lot of support from other people. My dearest Patricia helped me always by listening, asking critical questions and guidance. She became my lifelong friend, who took my hand whenever I felt down without a second thought and never doubt my abilities. Thank you dear Mehrnoosh for giving me your unconditional friendship, a place to stay when I was tired of driving back home. Thank to my neighbors, Angela and Annadorien, Shifa, Masood and the late loved Mahpareh for being there for me when I was in need. I also enjoyed my time in the bicycle lab with other people there, like Pier, Tim, Goerge and Inge who we spend pressure moments of consultation and commiseration together. Thank you my dear classmates, Keyla, Nooshin, Farzad and Nazgol who became close friends, and made me believe that I can make it.

Thank you dear Mina, for your spiritual support and valuable advices pushing me forward, in the times when I lost the way. Thank you my dear Willem. I was lucky enough to have your support and patience in the last years and especially the difficult last few months. Thank you my brother Mehrdad, for giving me a shoulder to cry in my sadness and laughing loudly with me in my happiness. Thank you my all-family members, especially the closer than mother aunts Shamsi and Fariba and my uncles and cousins. I cannot imagine that I could have made it without you.

I dedicate this thesis to my mother Parvaneh who has always encouraged and supported me in my life. To my daughter Armita who mind and soul we are the same. Thank you for being both the sunlight and moonlight to me.

List of symbols and functions

φ	Orientation
v	Linear velocity
ω	Angular velocity
γ	Linear acceleration
α	Angular acceleration
m	Mass
I	Inertia matrix
g	Gravity
r	Vector
t	Time
M	Torque
F	Force
P	Power

LCS	Local coordinate system
GCS	Global coordinate system
MCS	IMU coordinate system
FCS	Functional coordinate system

R	Rotation matrix
q	Quaternion
$q_{A\to B}$	Quaternion represents rotation from coordinate system A to coordinate system B
$\overline{q}$	Complex conjugate of quaternion

$\|\|\cdot\|\|$	Euclidean norm
$\otimes$	Quaternion multiplication
$\times$	Vector cross product

ROM	Range of the movement (We did not used ROM as the range of motion)
RMSD	Root mean square deviation
MD	Maximum deviation

Table of contents:

1 INTRODUCTION 1

1.1 Motivation 1

1.2 Research objective 3

2 PREVIOUS WORKS AND CHALLENGES 5

2.1 Marker-based motion tracking method 5
2.1.1 Marker-based motion tracking limitation 6
2.1.1.1 Markers occlusions 6

2.2 IMU-based motion tracking method 7
2.2.1 Strap-down-integration algorithm 7
2.2.2 IMU's data considerations 9
2.2.2.1 Data clipping 9
2.2.2.2 Error characteristics of gyroscope and accelerometer 9
2.2.2.3 Drift compensation 10
2.2.2.3.1 Data fusion approaches 11
2.2.2.3.2 Specific assumptions 12
2.2.3 Human body motion tracking with IMU 13
2.2.3.1 Choice of coordinate system 13
2.2.3.2 Functional calibration 14
2.2.3.3 Simplifications assumptions 15
2.2.3.4 Choice of variables 16

2.3 Project overview 17

3 EXPERIMENTAL METHOD 19

3.1 Experimental setup 19
3.1.1 Marker-based motion capture system 19
3.1.1.1 OptiTrack system calibration 20
3.1.2 IMU-based motion tracking system 20
3.1.2.1 IMU system calibration 20
3.1.3 Connection between the two measurement devices 21

3.2 Method of measurement 21
3.2.1 Marker and IMU placements 22
3.2.2 Experimental protocol 23
3.2.3 Data acquisition 25
3.2.3.1 Limits and concerns 25
3.2.4 Synchronization 26
3.2.4.1 Limits and concerns 26

4 ANALYSIS METHOD 27

4.1 Kinematics analysis 27
4.1.1 Kinematic estimation for marker-based method 28
4.1.1.1 Segments local coordinate system 29
4.1.1.1.1 Joint centre 29
4.1.1.1.1.1 Cervical joint centre (CJC) and right Shoulder joint centre (RSJC) 29
4.1.1.1.1.2 Lumbar joint centre (LJC) and left hip joint centres (LHJC) 29
4.1.1.1.1.3 Elbow, Wrist, Knee and Ankle Joint Centres (REJC, RWJC, LKJC, LAJC) 30
4.1.1.1.2 Segments LCS 30
4.1.1.1.2.1 Thorax 30
4.1.1.1.2.2 Right upper arm 30
4.1.1.1.2.3 Right lower arm 31
4.1.1.1.2.4 Right hand 31
4.1.1.1.2.5 Pelvis 31
4.1.1.1.2.6 Left thigh 32
4.1.1.1.2.7 Left shank 32
4.1.1.2 Joints rotation 34
4.1.1.3 Joints angular velocity and acceleration 34
4.1.1.4 Segments angular velocity and acceleration 35
4.1.1.5 Overview 35
4.1.2 Kinematic estimation for IMU-based method 36
4.1.2.1 Segments local coordinate system 37
4.1.2.1.1 Joint centres and segment length 37
4.1.2.1.2 Functional calibration 39
4.1.2.1.2.1 Method1: Optimization 39
4.1.2.1.2.2 Method2: 50% ω_{max} 40
4.1.2.1.3 Orientation of IMU with respect to the segment 42
4.1.2.1.3.1 Thorax 42
4.1.2.1.3.2 Right upper arm 43
4.1.2.1.3.3 Right lower arm 43
4.1.2.1.3.4 Right hand 43
4.1.2.1.3.5 Pelvis 44
4.1.2.1.3.6 Left thigh 44
4.1.2.1.3.7 Left shank 44
4.1.2.2 Segment angular velocity and acceleration 45
4.1.2.3 Joints rotation 45
4.1.2.4 Joints angular velocity and acceleration 46
4.1.2.5 Overview 47

4.2 Anthropometric model & Power flow 48
4.2.1 Full body anthropometric model 48
4.2.1.1 Mass and Inertial Parameters 49
4.2.2 Inverse dynamics 50
4.2.3 Segment power 53
4.2.4 Joint power 53

5 RESULTS & DISCUSSION 55

5.1 Rotation angle 56
5.1.1 Segment angle 56
5.1.2 Joint angle 56

5.2 Angular velocity and acceleration 60
5.2.1 Segment's angular velocity and acceleration 60
5.2.2 Joint's angular velocity and acceleration 61

5.3 Segment length estimation 64

5.4 Pitching and Power flow **66**
5.4.1 Kinematic results 66
5.4.2 Kinetic results 69
5.4.2.1 Kinetic energy 69
5.4.2.2 Power 70
5.4.2.3 Velocity 72
5.4.2.4 Joint force and moment 73

6 CONCLUSION & RECOMMENDATIONS 75

7 APPENDICES 81

Appendix 1: Quaternion formulas **81**

Appendix 2: Anthropometric model **83**

Appendix 3: Description of the Optitrack system **85**

Appendix 4: Description of the Shimmer3 **88**

Appendix 5: Description of Xsens suit **90**

Appendix 6: Description of Analog devices IMU **92**

8 REFERENCES 95

Chapter 1

Introduction

1.1 Motivation

Fast and accurate pitches are critically important for the performance of a baseball team. For this purpose, the players should be strong enough, remain injury free and perform a good technique. The process of training a good baseball pitcher costs years of strength and technical training. The instructions for these trainings are mainly based on empirical knowledge.

It has been stated that there is a trade off between fast pitching and being injured. Recently, almost all pitchers complain about arm related injuries once a year and above 90% of them did undergo elbow or shoulder surgeries (Arthur 2015). Over use, muscle fatigue, joint flexibility and poor mechanics are the main causes of injuries. An arm injury is usually a cause of lowering the pitching velocity. After surgeries the chance of healing and regaining the original velocity depends on injury. Besides, most of the players who gain high records of fast pitching would usually later become on disabled players list.

However, fast pitching is not a predictor of a pitcher getting injured, since there are also injuries free pitchers with above twenty years of fast pitching career, like Randy Johnson. What makes these players superior to the others is more likely to be their pitching technique, frequency and resting time between pitches.

Theoretical analysis and screening of the fast pitcher movements would help the other players to improve their pitching techniques and training methods in order to perform better pitches. Besides screening in giving real-time feedback to players on key mechanical parameters like joint angles and velocity, would help the players to improve their training procedures and finally safely increase their pitching velocity.

Fastball pitching is the fastest pitch in baseball. It is a very fast movement in three-dimensional space comprising of a sequence of complex movements with large range of motions. Simplification of the kinematic analysis of pitching motion in two-dimensional space results in underestimating of the player profile (Knudson 2007). Therefore, the kinematic analysis of pitching motion is not a conventional analysis based on the standard human range of motion and cannot be evaluated in two-dimensional space.

Various complex methods and devices are available to measure the motion for biomechanical analysis. There are a number of different technologies used to either directly "capture" the motion based on anthropometric data, like position, or indirectly "track" the motion based on different kinematics data, like orientation, distance, velocity and acceleration.

The direct motion capture is usually recorded with imaging methods (Leardini, Chiari et al. 2005). These methods are generally based on construction of a three-dimensional model, having the positions of anatomical landmarks in several different photos. This method is the standard motion captures system in which the anatomical landmarks are tagged with markers known as marker-based method.

The most accurate version of marker-based methods is the use of intra-cortical pins to avoid the marker inaccuracy due to skin motion (Lafortune, Cavanagh et al. 1992). Yet, the pins may buckle or wobble and this method is highly invasive and has ethically concerns. Other medical imaging devices has been used for joint motion measurements, like high accuracy X-ray (Ackland, Keynejad et al. 2011). However, these methods have a narrow field of view since the motion is limited to the size of the imaging device and therefore only one or two joints can be imaged. Besides, these methods are too slow and expensive and have side effects due to radioactivity of X-ray imaging.

The marker-based motion capture methods are the current standard method to measure the baseball pitchers motion. However, the marker-based motion capture systems are very impractical to be used in the baseball field to measure the motions and provide online feedback to the players. The reason is that it is difficult and too time consuming to place many cameras in baseball field and the markers on player's body and tracking the data online. Besides, the markers fall down easily since players are sweating. Also the sunlight introduces noises to measurements and the pitcher needs to be in underwear.

The indirect tracking of motion is done with: ultrasonic receivers and transmitters to measure distance (Kim and Kim 2013), magnetic field measurements to measure orientation (Song, Li et al. 2014), or with the Inertial measurement units to measure orientation, angular velocity and acceleration (Wang, Zhang et al. 2015). The magnetic and ultrasonic systems are subjected to environmental noise and have limited range of measurements. The inertial measurement units (IMU's) are more practical to investigate kinematics of players in field.

IMU's contains accelerometer, gyroscope and magnetometer sensors. Each of these sensors or preferably a combination of them is used for motion tracking. IMU-based motion tracking algorithms are the latest advancement in motion tracking systems and did attract numerous researches due to its high reliability and independence. One of the main advantages of using IMU sensors is the fact that they are light and wearable. Thus the measurements can be done out of laboratories, on the field for sports and during daily life for clinical applications.

This technology is an adaptation of aerospace and military attitude heading reference system (AHRS), which was later used in sport engineering and medical rehabilitation for the estimation of the human body performance. However, as most new technologies, which are not yet explored in every aspect, IMU's motion tracking systems are also still subjected to several limitations and imperfections which needs to be improved.

There are a number of recent researches on developing IMU-based algorithms and techniques to estimate human body movement kinematics based on inertial sensor system (van den Noort, Ferrari et al. 2013, Li and Zhang 2014). There are full body IMU packages commercially available, like the Xsens suit. However, these packages are quite expensive and the accuracy of those commercially available packages for academic measurements is not established. For example, it is stated that the new Xsens suit in dynamic measurements has 1° RMS (Appendix 5). But it is not clear this error is estimated over which velocities of motions. Besides this error is based on repeated trials within the same system not in comparison with another motion tracking system. Also, the available pre-programed IMU's instructions and software algorithms for position and orientation tracking are difficult to reproduce and adapt for the subsequent application fields (Roetenberg, Luinge et al. 2009).

There are a few researches done on tracking the motion of baseball players using an IMU-based method comparing with a marker-based method. Lapinski et al. 2013 reported the IMU-based method angular velocity measurement on shoulder joint rotation during pitching asses 6%

STD, being better than the standard marker-based method with 15% STD. However, this seems more to be due to filtering of data than a reason to validate the data. Because the magnitude of the same measurements shows the marker-based method recorded an average angular velocity of 5080˚/s, while the IMU-based method observed an averaged velocity of 4431˚/s (which is around 13% lower than the marker-based one). In this study, the comparison between the maximum angular velocity of the two methods, which is the most important part for the baseball measurement, has not even been reported (Lapinski, Berkson et al. 2009, Lapinski 2013). There is not yet a validated tracking motion of fastball pitchers in baseball using IMU-based method compared to the standard motion tracking measurement established.

1.2 Research objective

The main purpose of this project is to develop a practical but also accurate experimental setup to measure the kinematics of the pitcher inside the baseball field and outline an IMU-based method to analyse the pitching motion. Since there is many researches available with the marker-based motion capture methods, we can use a marker-based measurement as reference to validate and analyse our IMU-based measurement. However, it is also important to keep in mind that having the marker-based motion capture system as a reference does not mean that the marker-based motion capture provides us the real accurate motion, but it is the standard method in motion capture method.

The main goal of this project can be formulated as:

"Development and validation of an IMU's motion tracking system
for measurements of baseball pitcher kinematics,
having the marker-based motion capture data as the reference."

In order to accomplish this research goal, in chapter 2, we will review shortly the main structures and limitations of marker and IMU-based methods that we need to know before developing a new method and measurements. Knowing this initial knowledge, at the end of chapter 2 the achievement to the above main goal would be formulated in smaller steps.

Chapter 2

Previous works and challenges

In this chapter, we briefly review the important characters of marker-based tracking methods. Then we would look into the important characters of presented IMU-based tracking methods and their limitations and imperfections. Beside we would also explore the available solutions to these problems and the ways to obtain best result, which we chose to use in our method.

2.1 Marker-based motion tracking method

Motion capture with marker-based methods is a technique to record the three-dimensional (3D) positioning of a subject in a global coordinate system (GCS). Several different technologies have been developed, like active and passive markers.

Passive markers are simple markers reflect infrared (IR) light. Such markers can be flat or spherical. Spherical markers may reflect light at each possible angle where the flat markers only reflect lights between 0 and 60° with respect to cameras. Passive markers have simple and flexible setup and are used for most of the applications.

Active markers are infrared (IR) light emitting diodes (LEDs), which requires wire or battery to operate. The advantaged of this kind of marker is that they do not rely on reflecting lights but they emit light themselves. Thus there can be tracked from larger distance and after measurements the markers are already identified. But the measurement preparation is complex and too time consuming with placements of al weird LED markers and cameras.

Vicon, Motion Analysis Corp, Qualysis and OptiTrack are the major commercial available systems, which are used in different areas like; medical researches, film industry and video games. In a motion capture measurement, markers are place on anatomical landmarks on body. The data taken by cameras are reconstructed to build the 3D path of markers positions. The path of several markers can be used to represent body segments and the local coordinate system of each segment (LCS).

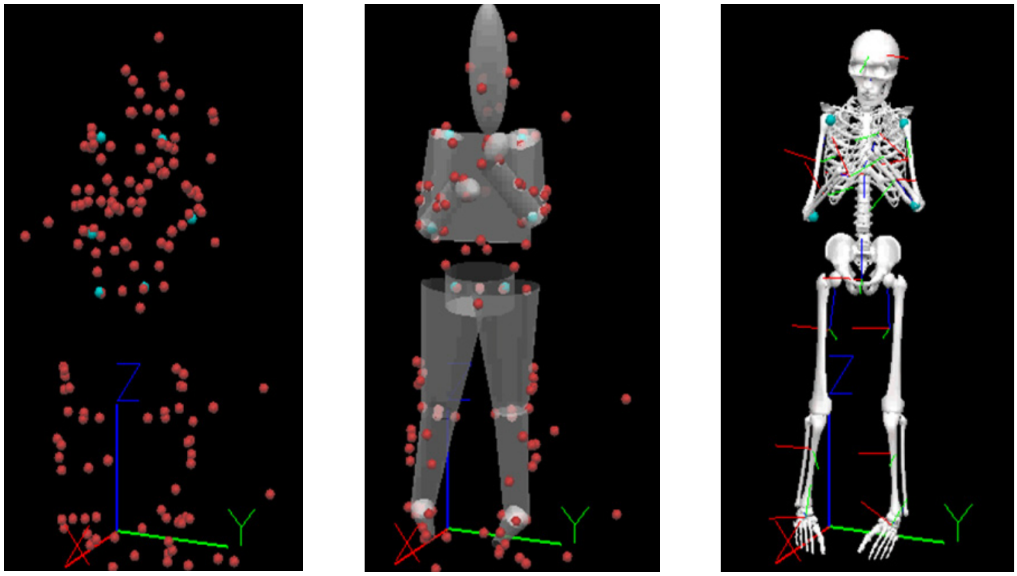

Figure 2-1 right: markers position in a global reference frame (GCS) are captured, middle: segments are defined based on markers position, left: segments local coordinate system (LCS) can be defined based on markers position (Lapinski 2013)

2.1.1 Marker-based motion tracking limitation

2.1.1.1 Markers occlusions

Markers are very susceptible to data occlusion. Each marker needs to be seen at least by two cameras at each recording frame in order to estimate the 3D position of the marker. If a marker is not seen by at least 2 cameras, occlusions occur and it is not possible to compute the global 3D position. Occlusions are a bigger problem in passive markers than in active markers. Active marker would be identified after collision as the same marker, but passive markers would be misidentified as a new marker. These paths can be reunited and gaps can be filled in by interpolation.

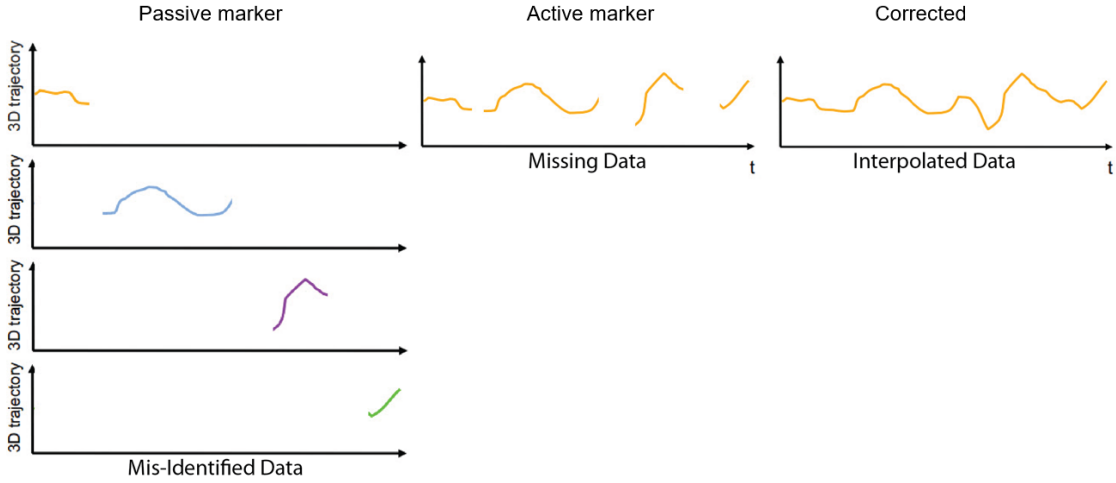

Figure 2-2 when occlusions occur some data are missing. Occlusion is more problematic in passive markers than active. Active marker would be identified after collision as the same marker, but passive markers would be misidentified as a new marker. Marker paths can be reunited and gaps can be filled in by interpolation, modified from (Cherveny 2015)

The gap filling simplifies the differentiation and integration steps. However, gap filling is a source of error and the produced data needs to be removed from the results before data analysis.

2.2 IMU-based motion tracking method

An IMU is a Micro-Electro-Mechanical module typically comprised of accelerometer, gyroscope and optionally magnetometer sensors.

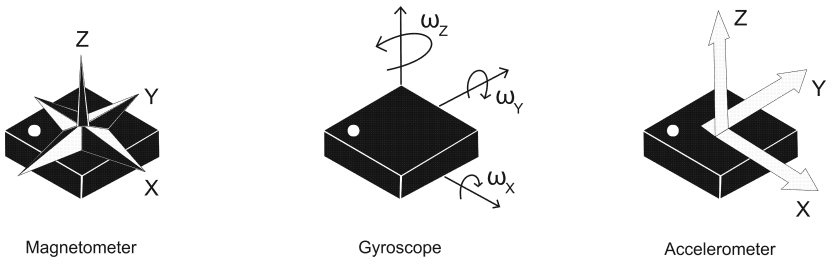

Figure 2-3 IMU comprised a combination of gyroscope, accelerometer and magnetometer, recording velocity, orientation, accelerations and gravitational forces.

Looking into literature on IMU-based motion tracking techniques, we can find application of this technique in aerospace, biomedical engineering, robotics, virtual reality, sport engineering (Seel 2016). However, the structure of all IMU-based motion tracking techniques is based on a common concept, which is called strap-down-integration algorithm. This concept comes originally from aerospace, where it is difficult to capture the motion of a spaceship, the problem can be simplified using strap-down integration of an IMU data placed on the spaceship (and in other applications on any moving object in 3D space and thus also on human body).

Since the IMU records the data regarded to its own coordinate system and as the IMU moves and rotates this coordinate system is also moves and rotates. Using strap-down-integration algorithm, it is possible to compute the position and orientation of the IMU with respect to its initial position and orientation. Having these kinematics data for the IMU positioned on the object, kinematics of the object with respect to its initial condition can be estimated.

2.2.1 Strap-down-integration algorithm

The gyroscope records the angular velocity (ω). The integration of the gyroscope angular velocity provides us the rotation with respect to the previous orientation (φ_0). By definition the rotation (φ) of an object is to be computed by numerical integration of its angular velocity:

$$\varphi(t) = \int \omega(t) \, .dt + \varphi_0 \tag{1}$$

This derivation is given slightly different in literatures by different expressions and assumptions like constant angular velocity or rotation around specific axis, but mathematically they are all corresponding to the above concept.

Each rotation transforms a vector from the local coordinate system of IMU sensor (MCS) at one moment in time to MCS at a previous moment in time (hint: this coordinate system is moving). These changes in rotation and positions can be expressed by rotation matrix. As in Figure 2-4 denoted for each time step by: R_1 , R_2 , R_3 and … .

The question is: "How to express this rotations in a fixed global coordinate system?"

The solution is the strap-down-integration, in which the initial orientation of IMU can be taken as the fixed reference coordinate system and we can transform the orientation at each moment in time to this reference coordinate system. As in Figure 2-4 expressed by: $\mathrm{R}_2.\mathrm{R}_1$ and $\mathrm{R}_3.\left(\mathrm{R}_2.\mathrm{R}_1\right)$.

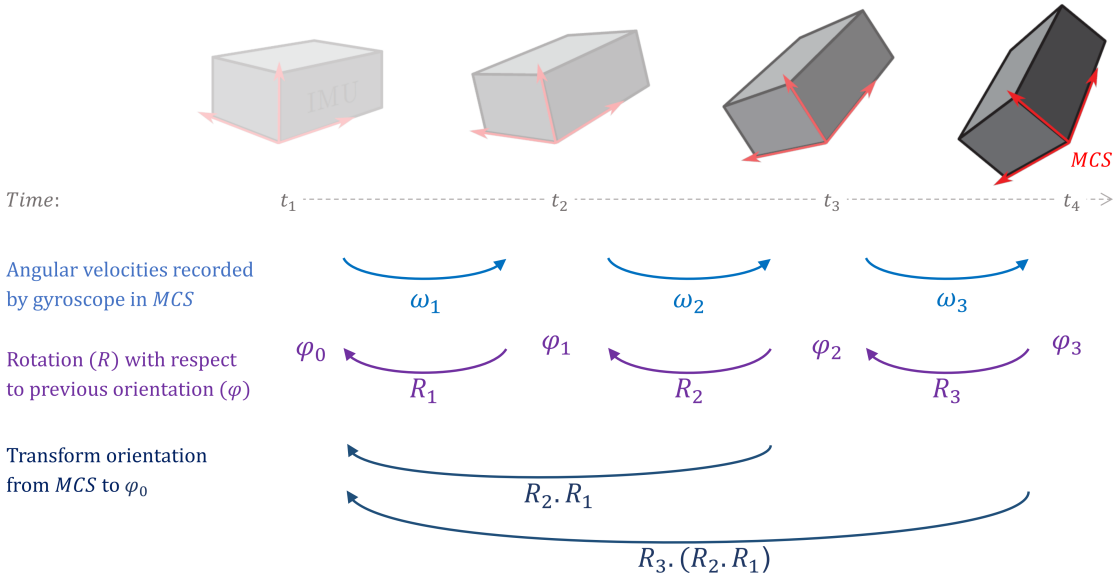

Figure 2-4 Strap-down-integration: angular velocity recorded by gyroscope can be integrated to obtain the rotation with respect to the previous orientation in time. The problem is that IMU is to attach to a moving object and therefore IMU records data in its moving coordinate system (MCS). The initial orientation of IMU can be assumed to be the fixed coordinate system and we can transform the orientation at each moment in time to this fixed coordinate system.

Having the rotation matrices to transform the coordinate system of IMU at each moment of time to the fixed coordinate system, the acceleration data recorded by IMU sensor can also be transformed to the fixed coordinate system. Subsequently we need to subtract gravity from acceleration data. Afterwards by integration of acceleration with respect to time, the changes of velocity and position can also be computed (Seel 2016).

$$x(t) = \iint \gamma(t)\,.dt^2 + x_o \tag{2}$$

Figure 2-5 shows a schematic view of the above procedure to compute orientation and position from the IMU data using strap-down-integration.

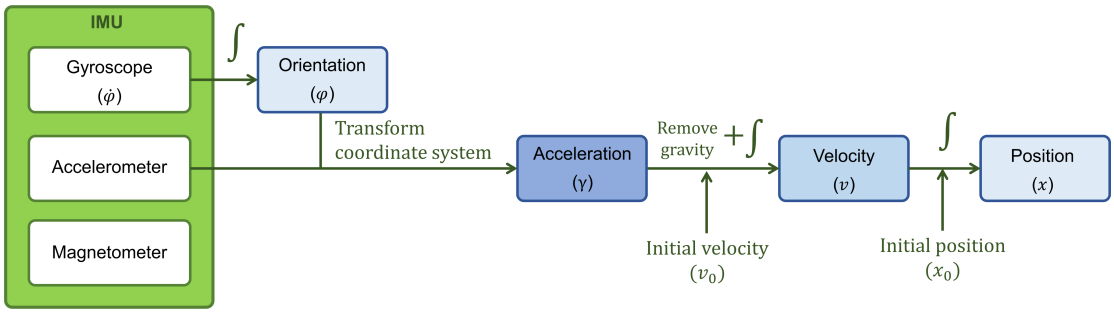

Figure 2-5 Schematic view of the Strap down integration routine for orientation, acceleration, velocity and position computation from IMU data. An inertial measurement unit contains gyroscope, accelerometer and magnetometer sensors, which measure respectively angular velocity and linear acceleration and magnetic field. The angular velocity is integrated in time to obtain the orientation. This orientation then is used to transform the acceleration vector from the local coordinate system of the IMU to a global coordinate System. This can then be integrated to get velocity and position.

2.2.2 IMU's data considerations

2.2.2.1 Data clipping

When using IMU for motion tracking, an important issue is choosing an appropriate IMU with sufficient range of measurement. Inadequate range of measurement of sensors may results in a form of distortion called "data clipping". Data clipping happens when the magnitude of the data to be measured exceeds the threshold. The result is that the sensor is unable to record those data and thereby the data would be underestimated.

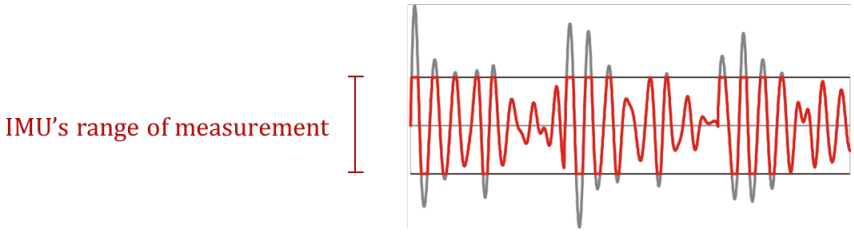

Figure 2-6 the real data in grey and the clipped data in red

A number of the previous studies did consider data clipping phenomena, as the reason that the IMU-based systems are not appropriate for the sport engineering fields measurements, where it is desired to record fast movements like fast ball pitching with high velocity and accelerations. For example, Ahmadi et al. 2010 states there does not exists a gyroscope which can records movements of faster than $\pm 300^{\circ}$/sec, which disqualifies the applications of IMU sensors for sports measurements (Ahmadi, Rowlands et al. 2010).

However, it is possible to build and program an IMU suitable for special range of motion measurement (to record only fast movements). Furthermore, the technology is improving fast and as the technology is growing, it seems this limitation is vanishing, and there are several pre-programmed, small and light-weighted IMU sensors available which claim to cover up the whole range of players motions. The recent Xsens (fabricated in the Netherlands) and Shimmer (fabricated in the United Kingdom) sensors claim to be able to record much faster movements in the range of $\pm 2000^{\circ}$/sec (Appendix 4 and 5). Even the Analog devices sensors (fabricated in the U.S.A.) are entitled to be capable to record much faster movements in the range of $\pm 20000^{\circ}$/sec (Appendix 6).

2.2.2.2 Error characteristics of gyroscope and accelerometer

As it is mentioned in 2.2.1, IMU-based kinematic computation uses numerical integration. Mathematical integration of a set of data with a constant bias, results in that the bias grows non-linearly in time. This phenomenon is called "drift". Overall, errors in the IMU recorded data results drift in orientation and position estimation after integration.

When an IMU is not moving, the measurements of gyroscope should be zero and the accelerometer output should show only the gravity (9.8 ms^{-2} in vertical direction). However, in practice usually the measured data by the IMU sensor contain an offset from these values. The average of these offsets is known as the constant bias of the IMU. Initial calibration steps are suggested to remove this offsets. However, the calibration steps are also subjected to scaling and axis alignments errors. Any error in calibration of gyroscope sensor after integration results in an orientation drift proportional to the angular velocity. And any error in calibration of accelerometer sensor after integration results in an orientation drift proportional to the squared rate of acceleration.

The bias of IMU is an accumulation of different sources of errors, not only calibration error. IMU sensors measurements are subjected to thermo-mechanical disturbances of environment and thereby not only the measurements are affected but also the calibration. Further, when IMU is turned on, its temperature is increasing. As the temperature is increasing the bias is also increasing non-linearly in time. This bias is to be simulated as a white noise. This bias after

integration results in a linear growth of residual bias in orientation estimation and a quadratic growth of residual bias in position estimation.

Furthermore, an IMU is an electronic module with its electrical flicker noise which exposure in random time. This error is to be simulated as random bias of instability (Woodman 2007, Seel 2016).

Altogether, both gyroscope and acceleration recordings are subjected to several sources of biases. Woodman 2007 did a systematic study on the above sources and characteristics of errors and simulated the significant errors as the sum of these errors (Woodman 2007).

The simulated logarithmic plot of this estimation in Figure 2-7 shows that the drift grows exponentially in time. The accelerometer bias is the significant cause of drift at the initial few milliseconds (until 0.3 seconds), after this time the gyroscope bias becomes the significant cause of drift. Practically, it is the gyroscope orientation estimation bias and not the accelerometer, which limit the overall accuracy of the most IMU-based motion tracking methods. An error in the orientation estimated by gyroscope may cause incorrect acceleration coordinate system transformation. Subsequent integration of the signals, results in a rapid accumulating of this error.

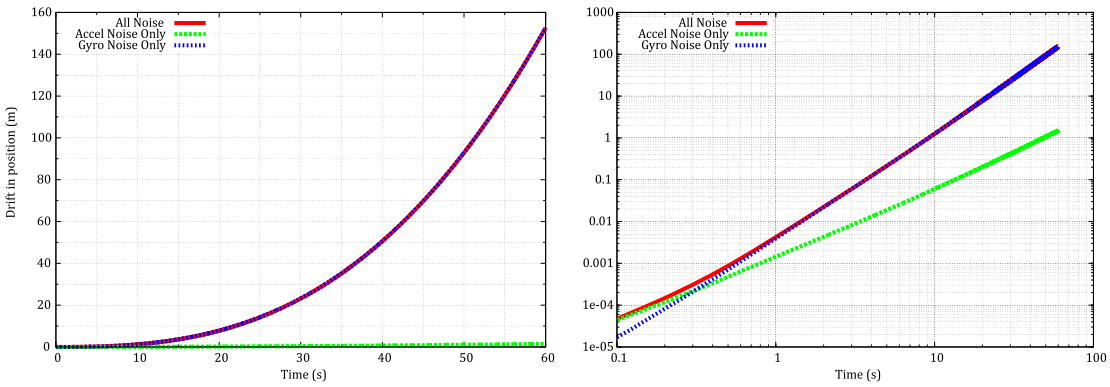

Figure 2-7 simulation of the metric and logarithmic propagation of the roll of gyroscope and accelerometer in drift arising (Woodman 2007).

Some of the commercially available IMU sensors, like Shimmer and Xsens, have an internal automatic compensation for these biases, which removes the drift from their output. For example, they have used the temperature bias, based on battery rate of reduction index (i.e. Voltage charge level).

2.2.2.3 Drift compensation

As it is shown in previous section, the drift is to be estimated quite well by an exponential function. Yet this estimation is subjected to initial calibration inaccuracy and varying environmental disturbances. These biases have different characters regarded to the varying recording duration and type of movement. This makes the bias reduction a necessary but not sufficient step, whereby any small bias in signals growth by integration. There is usually needed to apply additional drift compensation procedure on the specific part of the calculation which the bias comes from. Looking into the strap-down integration procedure, the major problem of position estimation inaccuracy is caused mainly by errors in orientation computation. The solutions to compensate for orientation drift in literatures are generally fall into two groups: the commonly used “data fusion” approaches and some studies used “specific assumptions”.

2.2.2.3.1 Data fusion approaches

The algorithms which use the data of two or more sensor types (gyroscope, accelerometer and magnetometer) measuring the same motion to "predict" and "update" the state of the system (orientation, acceleration, velocity and position), are known as data fusion algorithms. The prediction would be followed by an updating step, which specify how good it is the state predicted and continuously repeat this process for each time step or periodically over a span of data set to maintain a better estimation of current state of the system.

Data fusion does not need to be applied only on data of sensors from the same IMU. It is also possible to use data fusion of an IMU with the data of another system or another IMU. For example fusion of a set of marker-based with IMU-based position tracking data measured at the same time. The periodic position drift compensation approach is also commonly used for updating position estimation in navigation devices, whereas the position measured by GPS is to be combined with the high sampling frequency estimated position from gyroscope and accelerometer of an IMU (Woodman 2007).

Here a basic explanation is given to have an idea about what is happening is such filters. In a simple case consider from the angular velocity integration, the orientation is computed. This computation contains drift. The same motion is also measured by another sensor i.e. accelerometer. The orientation may also be computed from the accelerometer measurements. The fusion of these two set of data, coming from two different sensors and since they are measuring the same motion, this can be used to correct for the drift.

In this process, typically one of the data sets, which is more trustable and would be weighted more. The weighting between data sets usually denotes as the filter gain. The choice of weighting gain between IMU's sensors is based on the following remarks:

The orientation of an IMU can be defined by three angles: Pitch, Roll, and Yaw. These angles can be computed from the direction of gravity and the North Pole. The main concept behind this is that; the linear acceleration forces acting on an object are the sum of gravity, and the accelerations elicited by the movement. The accelerometer of a static IMU shows only the value of the gravity field. Because the only force applied to the static (not moving) IMU is the gravity, and since it is always pointing to the centre of earth, the pith and roll angles can be computed from accelerometer data (but not the Yaw, since the Yaw is not the matter of inclination). Similarly, The Yaw angle (heading towards Earth's magnetic North Pole) can computed using magnetometer data.

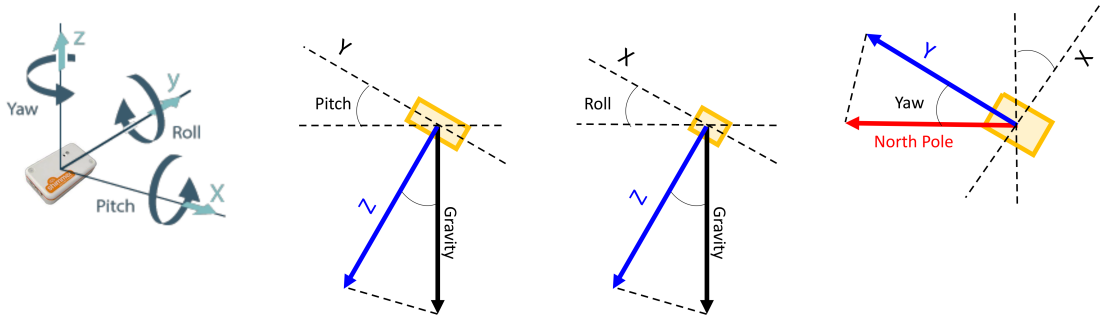

Figure 2-8 Orientation of IMU can be defined by Pitch, Roll and Yaw angles. These angles can be computed from the direction of gravity and the North Pole.

Accordingly, the drift in the inclination part of the IMU's orientation can be eliminated using the measured acceleration data (Fusion of gyroscope and accelerometer data). Besides, the drift in Yaw angle can be eliminated using magnetometer data (Figure 2-9).

Note that, the magnetometer data are sensitive to magnetic fields which is hard to prevent in presents of ferromagnetic materials in the indoor environments of experimental marker-based motion tracking lab (electronic devices, computers, cameras setup and the structure of the building).

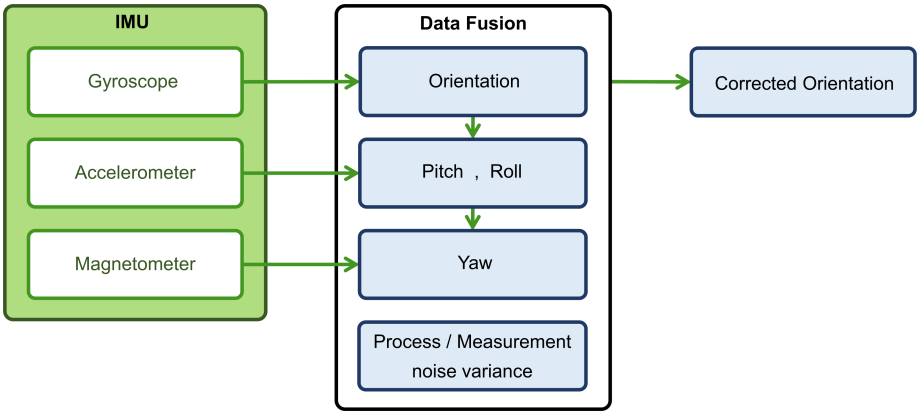

Figure 2-9- Orientation correction based on data fusion. Orientation (pitch, roll and yaw angles) can be computed from gyroscope. Accelerometer data can also be used to estimate pitch and roll. Magnetometer data can be used to estimate yaw angle. Different combination of errors estimated from gyroscope, accelerometer, magnetometer or other known sources of environmental errors (as explained in 0) can be used to compensate for drift.

There are many data fusion algorithms where as the most important of them are the complementary filter, the Kalman filter (with constant matrices), and the Mahony and Madgwick filter (Madgwick 2010). An experimental comparison (Cavallo, Cirillo et al. 2014) on these algorithms show that the dynamic Root-Mean-Square error (RMSE) of these algorithms are similar (smaller than 1◦) and the computational time of EKF algorithm is much longer than the Mahony and Madgwick (Table 2-1).

Table 2-1 – Experimental comparison of Fusion algorithms for attitude estimation. Hint, embedded system's computation time is longer than the academic experiments, i.e. with Matlab.

Algorithm	Euler angles RMSE [°]			Matlab/Simulink [ms]	Embedded system [ms]
	Roll	Pitch	Yaw		
EKF	5.05	3.24	5.93	0.1	2.7
Madgwick	5.54	3.93	6.27	0.017	0.15
Mahony	5.87	4.53	6.66	0.014	0.11

Extensive discussion and implementation of these algorithms is beyond the scope of this project. Here it is only sufficient to know that due to the above mentioned privileges of the Mahony and Madgwick filter, it is commonly used for human motion applications, and therefore we also used this filter (Madgwick 2010).

2.2.2.3.2 Specific assumptions

In order to accommodate the drift compensation procedure, some studies used specific assumptions. A simple example of this approach is that a walking foot velocity or distance to the ground is zero at the moment that foot contacts with the ground and an IMU placed on foot needs to measure zero velocity.

Therefore, the drift in the IMU velocity data measurements can be periodically corrected by the zero-velocity (or no distance to the ground) updates at the moments of the contact with ground. The weakness of the specific assumptions approach is that results would not be valid if the assumptions do not hold.

Figure 2-10 shows drift in position estimation (distance to the ground) during walking in IMU-based motion tracking comparing with the drift free marker-based approach.

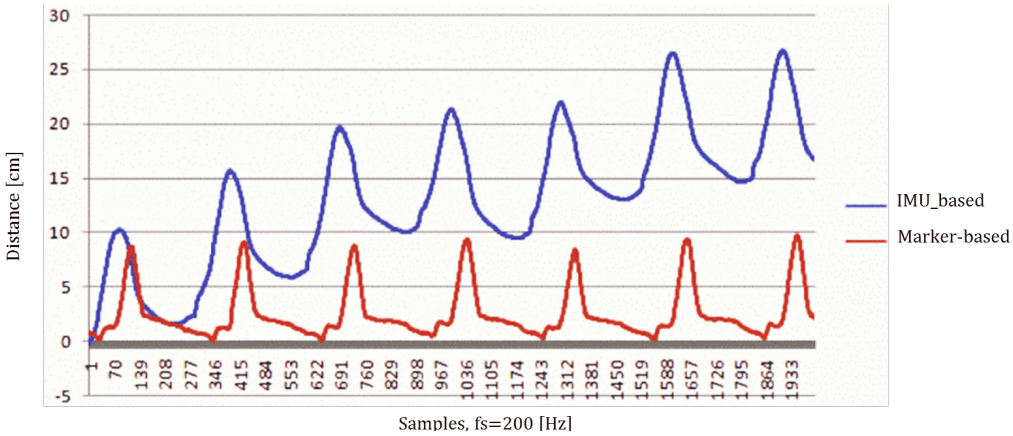

Figure 2-10 Drift in IMU-based motion tracking of foot during slow walking compared to measurement of the same motion using marker-based method (Lai, Charry et al. 2008)

2.2.3 Human body motion tracking with IMU

2.2.3.1 Choice of coordinate system

In IMU-based human motion tracking, the orientation and position of each segment would be determined by an IMU attached to it. As it is mentioned above, for kinematic analysis based on the IMU's recorded data, we need to choose a fixed coordinate system and it is convenient to choose the initial local coordinate system of the IMU.

When there are a number of IMU presented in the measurement, the question is how to define a unique global coordinate system (GCS)? If we choose the GCS to be the initial position of one of the IMU sensors, then the next question is what is the relative initial orientation of the other IMU sensors with respect to that IMU?

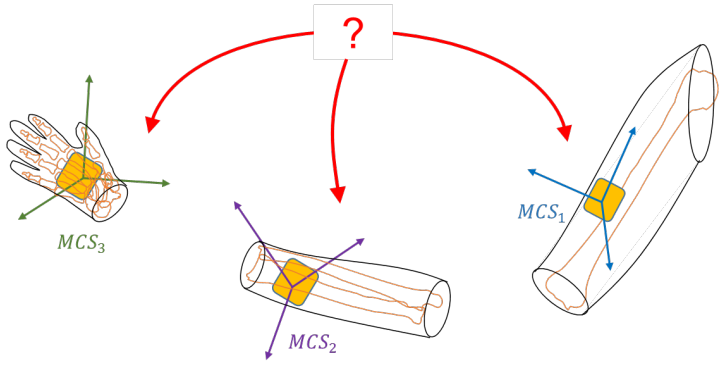

Figure 2-11 the data measured by IMU sensors are expressed in the IMU's coordinate systems. When tracking human motion using multiple IMU sensors, there is an issue that relative orientation of IMU sensors with respect to each other is not known.

It is good to mention here that the standard marker-based measurements did also face the problem of choosing a GCS. As it is explained in chapter 3, this problem for the maker-based systems is solved in an early stage before the measurements, when a GCS is defined via camera's calibration using a reference object.

Some commercial IMU sensors like Xsens suit, automatically converted the data to a global coordinate system through a pre-experimental calibration step (Roetenberg, Luinge et al. 2009).

Different methods can be used to find this relation. In chapter 4, it is explained that we take the initial relation between segments from the markers based method. Nevertheless, later in chapter 6 a convenient method is suggested to align the IMU sensors at the beginning of the measurement.

2.2.3.2 Functional calibration

A main problem in IMU-based motion tracking methods is that neither the direction nor the positions of the IMU sensors with respect to the body segments are known. As it was mentioned in previous section (2.2.3.3), some studies assumed IMU is precisely mounted on body segment the way that IMU's coordinate system is aligned with a meaningful physiological axis. There are also studies which did use the measurement data of predefined positions and/or motions, called functional calibration to find the orientation of IMU regarding to body segment mounted on it (Luinge, Veltink et al. 2007, O'Donovan, Kamnik et al. 2007, Cloete and Scheffer 2008, Favre, Jolles et al. 2008, Favre, Aissaoui et al. 2009, Roetenberg, Luinge et al. 2009, Takeda, Tadano et al. 2009, Lin and Kulic 2012, Li and Zhang 2014, Rogowski, Creveaux et al. 2014, Seel, Raisch et al. 2014, Schauer and Seel 2016).

An example for functional calibration with predefined static position is that in standing position with vertical and straight legs, the accelerations recordings have been used to determine the orientation of IMU with respect to the longitudinal axis of thigh and shank (Favre, Aissaoui et al. 2009, Takeda, Tadano et al. 2009).

Other studies determined the same relation using predefined functional calibration motion. They used the gyroscope recordings during lateral rotations of leg to determine the orientation of the IMU mounted on thigh with respect to the longitudinal axis of thigh (Takeda, Tadano et al. 2009). Figure 2-12 shows some examples of functional calibrations movements.

Figure 2-12 Calibration motions to determine orientation of IMU regarding to body segment (Seel, Raisch et al. 2014)

Among these studies, Rogowski et al. 2014 for upper limbs and the Seel et al. 2014 for lower limb gave comprehensive outlines of functional calibration movements (Rogowski, Creveaux et al. 2014, Seel, Raisch et al. 2014).

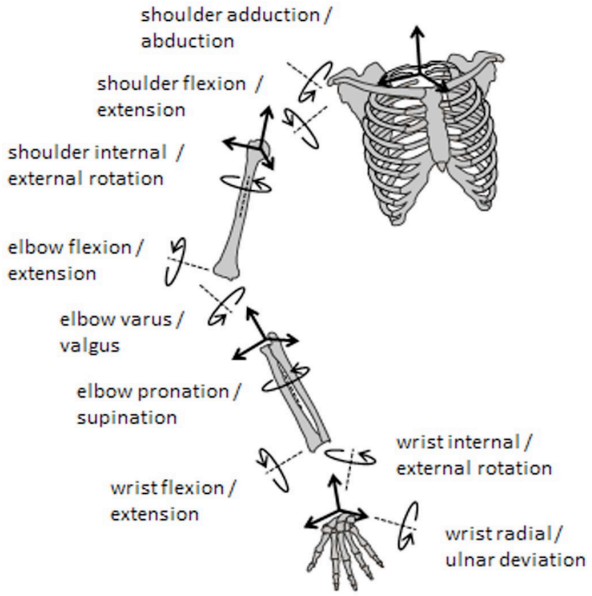

Figure 2-13 Functional calibration of upper limb (Rogowski, Creveaux et al. 2014)

Functional calibration allows defining the orientation of the IMU with respect to the segment, which defines the joints axes. Most likely the estimated axes would not be perpendicular to each other. This means that the computed coordinate system would not be Cartesian. The routine to convert these computed axes to a Cartesian coordinate system is as follow:

1- The first axis is to be defined by the calibration movement, which we trust the most.

2- Another calibration movement can define the second axis as the temporary axis, which would be corrected later.

3- The third axis would be defined to be perpendicular two the plane pass through these the first and second axis.

4- Subsequently the second axis would be corrected to be perpendicular two the plane passes through the first and third axis (Figure 2-14).

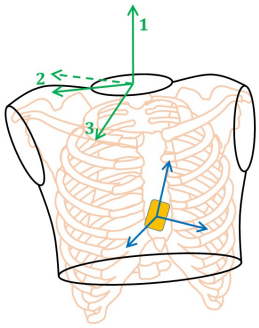

Figure 2-14 Functional calibration routine to define the orientation of the IMU mounted on the trunk with respect to trunk. A rotation of trunk is more truthful to be allows defining the orientation of IMU with respect to the first axis (1). Lateral flexion/extension allows defining the second axis (2), which needs to be corrected. The third axis (3) can be computed by cross product to be perpendicular to the plane pass through 1 and 2. Subsequently 2 would be corrected to be perpendicular to the plane passes through 1 and 3.

2.2.3.3 Simplifications assumptions

When we look into the previous literatures approaches, we realize many of the researches for simplifications of the problem took a number of assumptions, as:

1- The placement of IMU on body is assumed to be the way that one of the local coordinate axes of the IMU is aligned with a physiological meaningful axis (like the longitudinal axis of segment or the joint axis).

This results in inaccuracy of the results. An example of this is the study of Farve 2006 et al. where it is assumed the knee flexion/extension axis to be aligned with one of the axis of each IMU on tight and shank. This study noticed the integration of this misalignment introduces a drift in joint angle estimation and they suggested to remove the drift by a high-pass filter (Favre, Luthi et al. 2006).

Functional calibration routine is a method which is used in a number of recent studies to compute the IMU to segment coordinate system rotation, which practically reduce this misalignment error (Li and Zhang 2014). This routine is explained better in following section (2.2.3.2).

We would use Functional calibration routine to define the segments coordinate system. In chapter 3 and 4 you can find a comprehensive explanation of how did we used this method.

2- The body segments are usually assumed to be rigid and their attitude is measured usually only by one IMU attached to each segment.

3- The biological joint is often considered to be a perfect hinge, saddle or spherical joint.

An example of this is the studies of Seel et al. where he assumed the knee joint behaves like a hinge and shoulder joint as a spherical joint. Such mechanical joint defines kinematic constraints.

Like, in a hinge joint case, the angular velocities projections of two adjacent segments onto the joint plane (The plane which joint axis is the normal vector.) must be identical. Or for a spherical joint, the acceleration of joint centre in both local coordinate systems of the two segments must be identical (Seel, Schauer et al. 2012, Seel, Raisch et al. 2014, Schauer and Seel 2016, Seel 2016)

4- The skin movement is neglected and the IMU position and orientation with respect to the body segment is assumed to be constant.

The non-ridged, deformable human body joints and segments affect a human body measurement, which makes the measurements ambiguous. Subsequently it is needed to take some assumptions to define the parameters.

In this project we would also take these last three assumptions, to simplify the problem.

2.2.3.4 Choice of variables

In this project we aim to validate the results of IMU-based tracking method against a marker-based method. To do this, it is very important to choose the variables to be validated. We can analyse motion on different levels, from "orientation" to "angular velocity" or "angular acceleration". This is a relatively trivial mathematical computational issue that the amount of bias in the results depends on the choice of variables.

From orientation (φ) by one and two steps differentiations, the angular velocity (ω) and angular acceleration (α) can be computed respectively. However, the downside is that the numerical differentiation works as a high pass filter, which means any errors in the 3D positions will be amplified with each differentiation step.

Similarly, from angular acceleration (α) by one and two steps integration, the angular velocity (ω) and orientation (φ) can be computed respectively. However, the downside is that each integration step introduces a drift, which is proportionally increasing in time. Besides, integration is more challenging than differentiation, since we need to know a global reference points or initial condition for integration.

Table 2-2 differentiation and integration forms of variable levels

	Derivation form	Integration form
Orientation	φ	$\varphi = \int \omega \, dt + \varphi_0$
Angular velocity	$\omega = \frac{d\varphi}{dt}$	$\omega = \int \alpha \, dt + \omega_0$
Angular acceleration	$\alpha = \frac{d\omega}{dt} = \frac{d^2\varphi}{dt^2}$	α

The power generation during pitching starts mainly from stance foot and goes through body to the pitching hand and at the end the power transfers to the ball. In the fastball pitcher's application, we are more interested in angular velocity of body segments which eventually is needed to compute this energy generation flow and which results in magnitude of the velocity of ball. To do this, we need the angular velocities and inertial data of body segments.

The marker-based method provides us the positions of the markers and subsequently the body segments orientation. For computing angular velocity, one-step differentiation is to be done. The IMU-based measurements by gyroscope, accelerometer and magnetometer provide the angular velocity, linear acceleration and magnetic field. Integration of the angular velocity of IMU's gyroscope provides orientation. This orientation may be differentiated once to compute

angular velocity of body segment. But, it is desired to compute the angular velocity of segments directly from the IMU data.

Nevertheless, it is also interesting to compare the two methods at different kinematic level of variables to validate the method (segment orientation or joint angle, angular velocity and acceleration of joint and segments). This would be interesting, not only for baseball application, but for the overall validation of the method.

2.3 Project overview

In this project we aim to validate the results of IMU-based tracking method against a marker-based method. In order to validate the data, the deviation between IMU-based and marker-based measurements under different test conditions needs to be smaller - or in the range - of the natural variance observed in human motion. For fastball pitching studies the maximum velocities (not the average) need to be validated. Therefore, to validate the IMU-based method we set the allowable threshold at 10% for the maximum angular velocity.

Having this done, we can answer the main question of this research that whether we can get the same results from IMU and marker-based methods. If yes, how similar are the results. And if not, what are the differences and what is the source of these differences. It is also interesting to know, how does the IMU's functional calibration procedure affect the accuracy of measurements, by reproducing the same routine on the marker-based data.

As it was mentioned above the orientation and acceleration may also be computed and compare between the two methods. We need to keep in mind that differentiations introduce noise and integration introduces drift to data.

Further, the segment length can be calculated from the IMU data and having the segment length the kinematic data is complete to fill in a scalable rigid body model and compute the power generation flow. The inverse dynamic of the pitcher arm (from the pitching hand to the shoulder) is made to compute the joint forces and moments. For the whole body power flow calculation, the ground reaction force is needed and could not be measured in this experiment. The measurement of power flow can be used to estimate the best pitching configuration and real time feedback for each individual player. Figure 2-15 shows a schematic overview of the steps we would like to make. The yellow variables are to be compared as the index for validation of the IMU-based method.

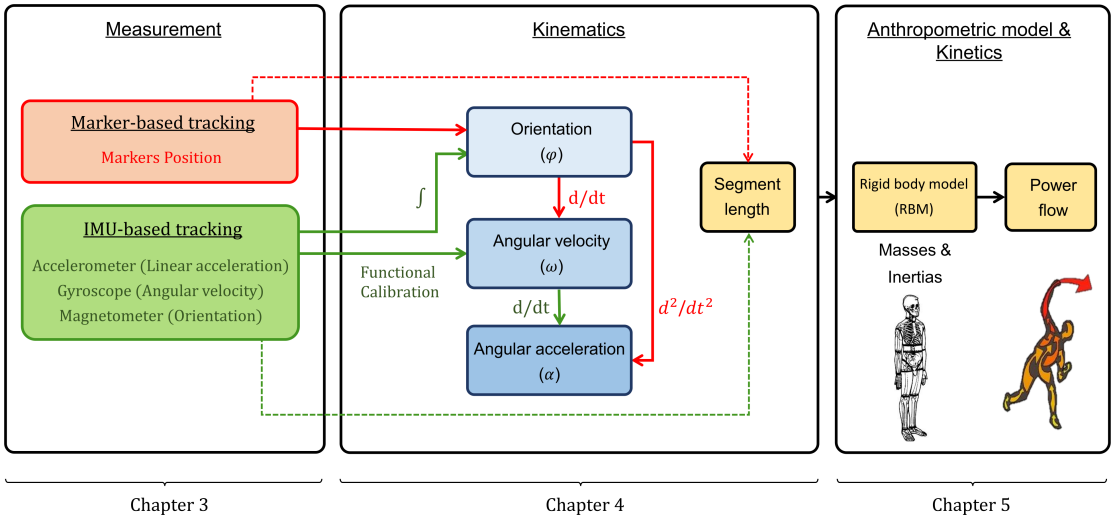

Figure 2-15 Overview of this project progress

The contents of this thesis is organized as follows:

Chapter 3 describes the experimental method for synchronized tracking of the same motion with IMU and markers to evaluate the IMU-based measurements against marker-based one.

Chapter 4 represents the kinematic analysis methods (estimation of joint angles, angular velocities and accelerations of body segments) for both IMU- and marker-based methods. This includes the functional calibration method to estimate IMU's orientation with respect to body segment (Transformation of IMU data to the joint centres). Then the method to compute segment lengths from IMU data is introduced. Afterwards the scalable anthropometric model is presented to estimate the masses and inertia properties of body segments using the body length as the scaling factor. Finally the method to compute body segments energy and power is explained to present the power flow in body segments.

Chapter 5 presents the kinematic and kinetics results and analysis. By identification of the sources of dissimilarities between IMU-based measurement against the marker-based reference, quantification of the error and evaluate the IMU-based measurement method.

Chapter 6 discuses the results and validate the IMU-based motion tracking against the marker-based measurements. Here the important achievements of this project are presented which can be used as a practical guideline for the IMU-based kinematic measurement in future.

Chapter 3

Experimental method

In this chapter, the experimental setup and measurement method is explained. The experimental setup consists of two separated but synchronized measurement systems measuring the same motion: 1) Marker-based motion capture and 2) IMU-based motion tracking system.

3.1 Experimental setup

3.1.1 Marker-based motion capture system

An OptiTrack motions capture system consisted of 16 cameras, 3 HUBs, a desktop PC and passive spherical markers are used in this project. Each HUB can be connected to maximum 6 cameras, thus 3 HUB are used to keep the cameras recordings synchronized and transfer data to the PC. The OptiTrack system is installed in a 6x6x3 meter area, where 16 cameras (OptiTrack flex 13) are mounted on 8 vertical pales. The "Motive" software is used to reconstruct marker trajectories from the skin markers tracking data. The markers can be tracked in when they are seen by at least two cameras. This results in that a part of the measurements area is lost and the real measurement area would be 4x4x3 meter (Schrauwen 2015). This volume is enough to test the pitching motion.

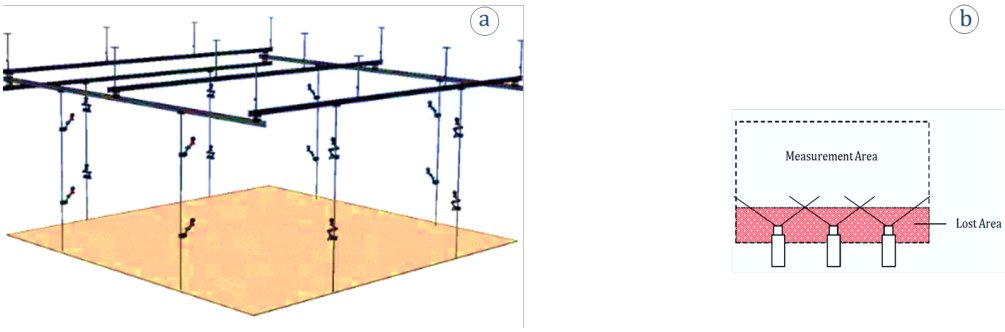

Figure 3-1 a) Measurement area is 6x6x3 meter with 16 cameras, b) The Lost area (Schrauwen 2015)

3.1.1.1 OptiTrack system calibration

In advance to experiments, in order to be able later to reconstruct the markers trajectories in 3D, it is needed to know the position of cameras with respect to each other and setup the accuracy of system to track a moving object (dynamic and static calibration). The dynamic calibration of cameras would be done by a wand with known rigid body defined by 3 markers, moving around in the whole measurement area and the captured frames of cameras would be corrected for the error in the known length measured of the rod. The static calibration is done by the L-form reference object (with three markers on it and a known geometry). By placing the L-form reference object in the experimental area the coordinate system axis on the ground would be defined. After the calibration of the cameras, the subject and experimenter do not have any contact with cameras. This guarantees a reliable measurement.

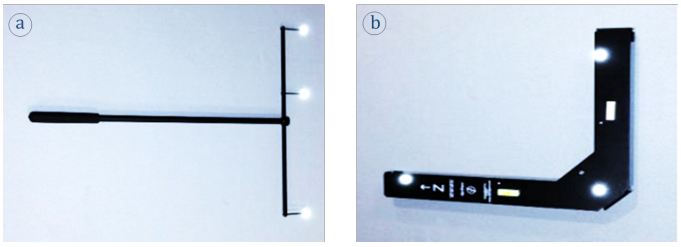

Figure 3-2- a) dynamic calibration wand, b) static calibration reference object (Schrauwen 2015)

3.1.2 IMU-based motion tracking system

IMU-based motion tracking system set-up consists of 8 IMU sensors (Shimmer3, see appendix 4) with its Base15 kit (Figure 3-4). The data is registered on SD cards of each IMU and after the measurements via the Base15 we bring the data to laptop. The "Consensys" software is used for between IMU sensors synchronization. It is also possible to send the data directly via Bluetooth to the laptop. However, since in this experiment we plan to do the analysis offline, in order to develop the method, there is no need to use the Bluetooth. We did a set of experiment with Bluetooth. It is difficult and takes time to connect the IMU sensors with computer to record data directly on computer. The most annoying problem was that when the an IMU disconnected (due to distance or being beside a part of body), eventually it remains disconnected till we bring the IMU near to computer and wait a few minutes till it connects again. Therefore, for the future experiments if it is aimed to use Bluetooth, it is suggested to support the system with a Bluetooth amplifier.

3.1.2.1 IMU system calibration

Preliminarily to measurement, we need to install a firmware on each IMU, setup the data acquisition format (frequency and limits) and calibrate each IMU separately to align the axis of the orthonormal coordinate system of each IMU with its outer sides (MCS).

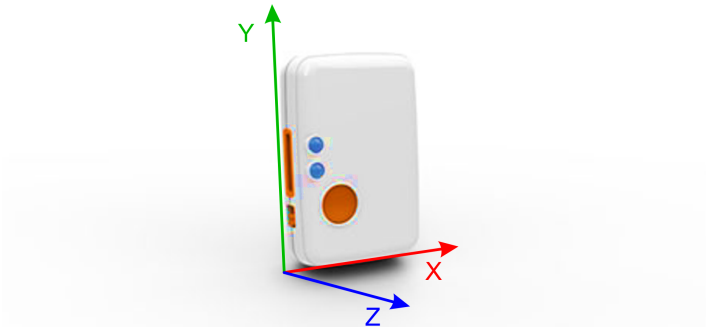

Figure 3-3- Coordinate system of IMU (MCS), Figure modified from (Shimmer 2014)

3.1.3 Connection between the two measurement devices

The Simmer IMU sensors have an external port (A6) in which a current signal up to 3 volts is allowed. Besides, the OptiTrack system exposure a trigger signal which goes through the HUBs and return to PC during each recording, to synchronize the cameras together. We reduce this trigger signal to 3 volts (important for not damaging the IMU) and record this on one IMU (we call it from now on the trigger IMU). The trigger IMU is only used for synchronization not for motion tracking. Each time we start recording by OptiTrack system, a trigger signal assert to the trigger IMU, and de-asserted when recording is stopped (Figure 3-4).

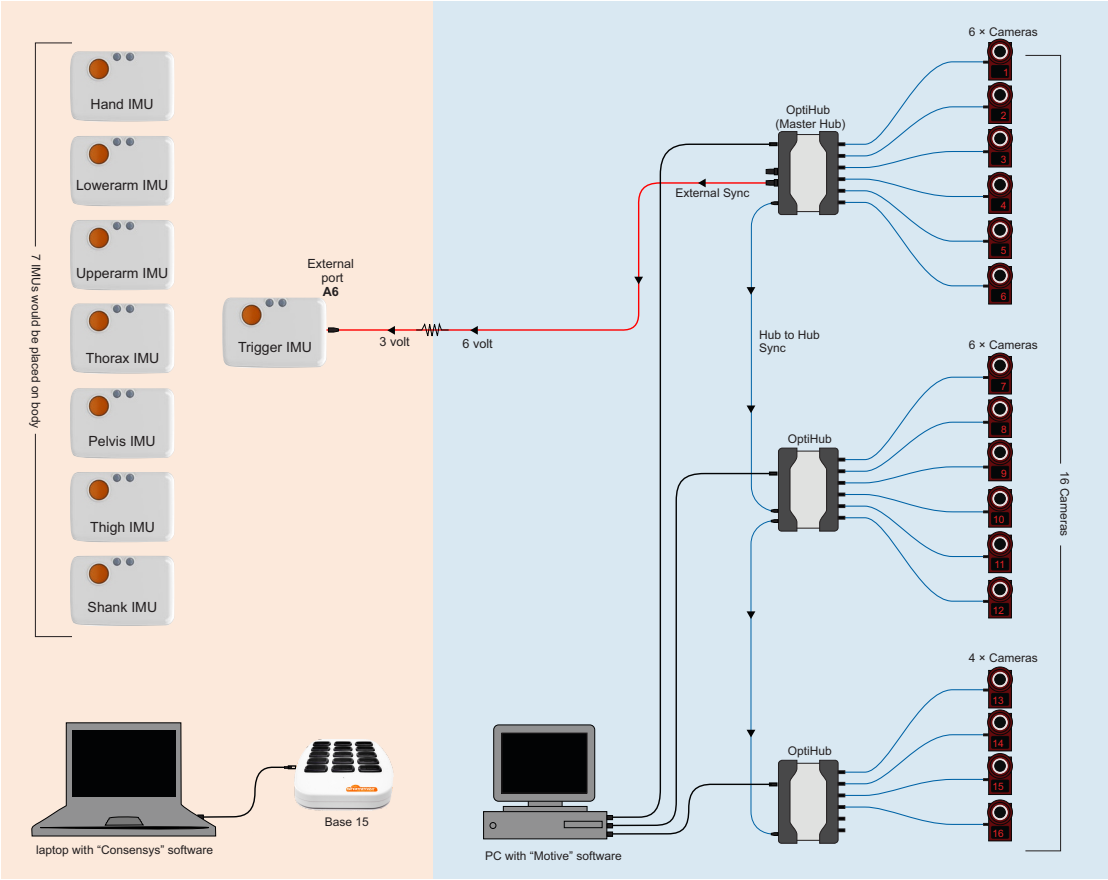

Figure 3-4- Schematic view of the synchronization of IMU system with OptiTrack system

3.2 Method of measurement

We did 4 pilot measurements to develop the experimental setup and solve hardware and synchronization problems. For example, placement of markers directly on the skin and on the special motion-tracking suite was done. Placement of markers with double-sided tape on skin was chosen to minimise inaccuracy. Data recording via Bluetooth and on SD cards was used and we chose to use SD card data recording. The results presented in this thesis are from the final working setup with one test subject; A 26 years old male with 71 kg weight and 183 cm height. The subject had no history of right upper limb complaints and gave their informed consent for this experiment.

3.2.1 Marker and IMU placements

It is common to place markers on bony parts of segments to reduce the inaccuracy due to the muscle contraction. However, some studies did mention that the skin is gliding on the bony parts and it is better to place the markers on the muscles which has smaller cross section and accordingly less volume changing due to the contraction (van der Helm and Pronk 1995, Lapinski 2013).

The placement of IMU's on the skin is not a standardized positioning. There is no reference protocol to place the IMU's. There are even studies that claim the IMU placement on different area on the same body segments does not result in a significant discrepancy in the results (Palermo, Rossi et al. 2014). Besides, position of IMU and markers should have some distance that they would not push each other due to skin motion. Also we put on each IMU a marker to have the position of IMU sensors in OptiTrack data. The markers are attached to the body on bony parts of body and IMU's on the muscles, which has smaller cross section and accordingly less volume changing due to muscle contractions.

Since we are interested in pitching motion, we choose to track only the pitching upper limb (Right hand, forearm and upper arm), the trunk (thorax and pelvis) and the stride leg (Left leg).

For the IMU-based system one IMU per each body segment is used to measure the orientation and velocity of each segment. Figure 3-5 shows the guideline of positioning the markers and IMU sensors that we used in this project. The name and position of the 20 Anatomical landmarks and the 7 IMU sensors, which are used to define the desired body segments, are shown.

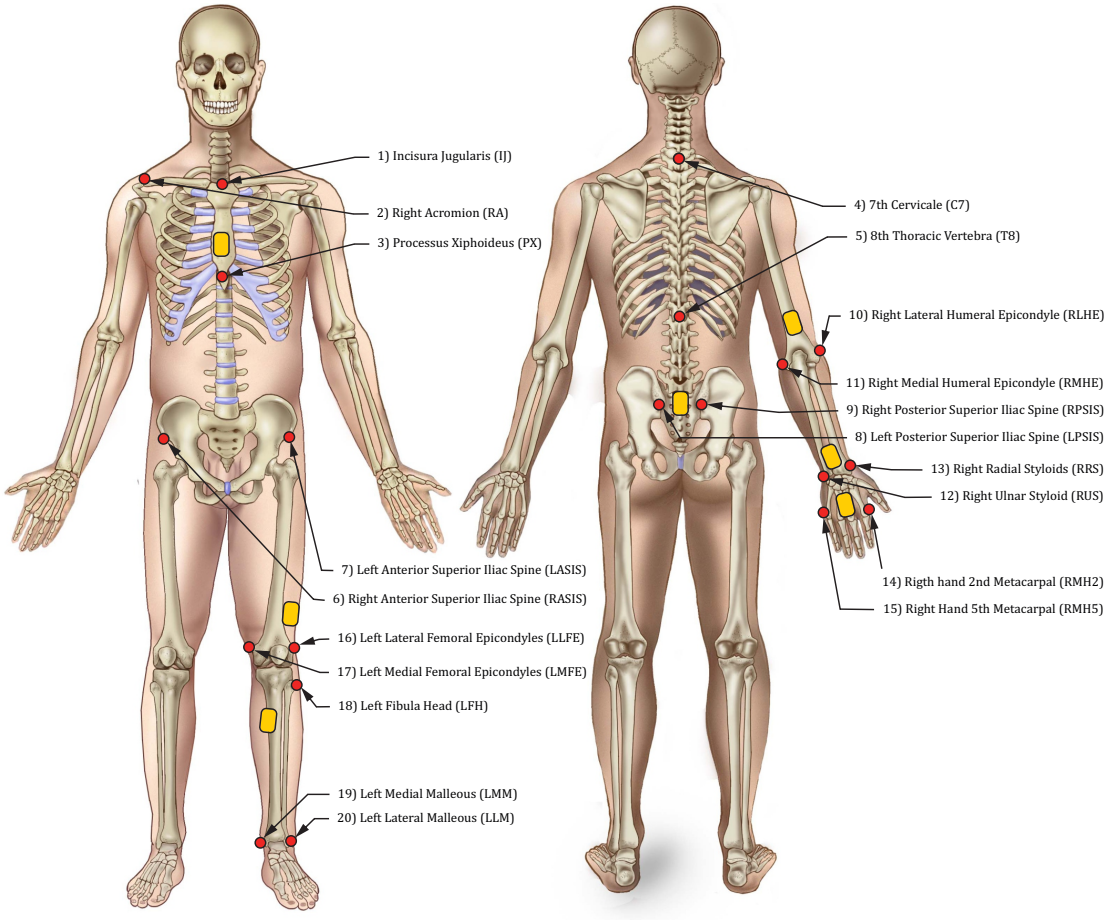

Figure 3-5 Placement of Anatomical landmarks (red circles) and IMU sensors (yellow rectangle) on body segments

In total, 20 anatomical markers and 7 extra markers on IMU sensors and 7 IMU sensors were placed on skin, to define the 7 body segments. The markers and IMU sensors are attached to the body by strong double-sided adhesive tape on bony parts of body (Figure 3-6).

Figure 3-6- Markers and IMU placement; subject is equipped with markers and IMU sensors, identifying 7 body segments.

3.2.2 Experimental protocol

Once all the IMU's are placed on body segments, before starting pitching measurements, the subject needs to perform at least two functional calibration movements per body segment to compute the orientation of each IMU regarding to the segment, which it is mounted on (as it was explained in section 2.2.3.2). Thus for each joint it is sufficient that the subject would perform two (not three) functional calibration movements. This routine needs to be done for the 7 body segments to reveal the orientation of the IMU sensors with respect to the segments, which is mounted on.

The subject is asked to perform more (than two) different possible functional calibration movements. The movements are also performed with different velocities. These are done to reveal the consequences of different calibration movements on results and establish a better measurement protocol for following measurements, which would be more discussed in results and conclusions (chapter 5-7).

In total, the subject did perform the following functional calibrations and experimental movements in 49 recording sessions:

- Static position section: Consisted of two static relaxed postures with body upright:
  - N-posture: neutral with arms beside the body and palm forward.
  - T-posture: with arms horizontal and thumbs forward
- Joints rotations section: Each preforms five times at three different speed (slow, normal and fast)
  - Right shoulder
    - Flexion/Extension: with the arm parallel to the sagittal plane until maximal humeral elevation is reached, then return to starting position. With palm in 3 positions; to the left, forwards and backwards
    - Abduction/Adduction: Abduct the arm parallel to the frontal plane until maximal humeral elevation is reached, then return to starting position.

        - Horizontal Abduction/Adduction: Abduct the horizontal arm parallel to the horizontal plane with palm downwards.
        - Internal/External Rotation: with elbow trunked 90°:
            - Upper arm horizontal and shoulder joint rotates so that the hand moves forwards and the palm faces the floor, then return to starting position.
            - Upper arm vertical and shoulder joint rotates so that the hand moves parallel to the horizontal plane with palm to the left, then return to starting position.
    - Right Elbow
        - Supination/Pronation: Elbow trunked 90° and lower arm rotates around its longitudinal axis, then return to starting position.
        - Flexion/Extension: with the lower arm parallel to the sagittal plane until maximal lower arm elevation is reached, then return to starting position. With palm in 3 positions; to the left, forwards and backwards.
    - Right Wrist
        - Flexion/Extension: Hand bends with palm down, towards the wrist, then return to starting position.
        - Radial/Ulnar deviation: hand bends towards the little finger, and then return to starting position.
    - Trunk
        - Rotation: subject sits on a chair and chain hands in front and rotates the trunk to left and right.
        - Flexion/Extension: subject stand and trunk bends forwards and backwards
    - Left Knee
        - Flexion/Extension: subject sit on a chair and flex and extend shank.
    - Left Hip
        - Flexion/Extension: stand on right foot, left leg is flexing and extending parallel to the sagittal plane. Left foot does not touch the ground.
        - Abduction/Adduction: stand on right foot, left leg is adducting and abducting parallel to the frontal plane. Left foot does not touch the ground.
        - Lateral rotation: stand on right foot, left leg is rotating from hip joint. Left foot does not touch the ground.
- Extra selected motions
    - Walking
    - Lunge: with (right and left) leg in front
    - Squat with trunk upwards and hands on the sides
- Pitching motions
    - Pitching while whole body moves
    - Pitching while only right arm moves

In order to prevent the subject to stare at cameras (there is a small hazard of IR exposure the subject eyes), the subject is instructed to look forward and no cameras is placed in front of the subject at eye level in the direction that the ball would be pitched.

The Madgwick's orientation computation algorithm that we are using has a single parameter beta, which controls the amount of trade-off between information from accelerometer, gyroscope and magnetometer. For better drift compensation and converge faster to the true state, it is advised that the subject remains still for at least few seconds upon start of recording set large beta (3 to 8) and for the rest of the recording set smaller beta ($\beta = 0.01\ to\ 0.1$). If not, then the orientation estimation fails.

Note that for our measurement, due to the environment condition inside lab (electronic devices, computers, cameras setup and the structure of the building), we needed to use a smaller beta ($\beta = 0.0001$), which means less trust the magnetometer and accelerometer and more trust gyroscope. Larger beta could not compensate for drift. Besides, both Shimmer's Matlab code (`updatequaternion`.m) and Madgwick's algorithm give the same results, since Shimmer's Matlab code use the same algorithm as the Madgwick's inside it. It means using $\beta = 0.0001$ in both Madgwick's algorithm and Shimmer's matlab code (`updatequaternion`.m), we could compensate for drift and produce a reliable orientation computation.

3.2.3 Data acquisition

After measurement, the following steps are taken to make the acquired data ready for analyses:

- For the OptiTrack data, the trajectories (markers positions) are reconstructed from the skin markers tracking data by the motive software. These markers positions are defined in a global reference frame (GCS) whereas the centre of this centre frame is somewhere on the ground. The position data in OptiTrack system are registered in separated trials whereas the starting time of each trial is at zero (sampling time is 0.0083s, 120Hz). The data for the first two time steps are exactly the same for all of the trials, this is due to the fact that trajectories at time zero is not known. The skin makers position (in ".c3d" format) are labelled in MOKKA software. And saved again in ".c3d" format (note that one of the trials when opened in MOKA had one time step less than the data at the end). The ".c3d" format files are imported in MATLAB. Some of the markers were tracked in a few separated data file, which were needed to identify (by "find(isnan)"), and reunited. Due to the occlusion of some markers in time, there were some gaps in data. The gaps have been filled in MATLAB by "fillgaps" function. A low pass filter with cut off frequency 3 Hz has been used to smooth the data and get rid of noise. The Nan data time vector is used to remove the unreal data.

- For IMU's data, Filtering of the IMU sensor output is carried out inside of the IMU. Filter output is modelled at a frequency of 500 Hz or lower, as desired. After the measurements all of the IMU's are set into the base15 ports and the registered data on the SD cards of IMU sensors are synchronized and exported via CONSENSYS software into "*.mat* " files. In this MATLAB structure format file, the following data are recorded: wide range accelerometer [m/s^2], low range [m/s^2], gyroscope [°/s], magnetometer, trigger signal [mV] and time.

3.2.3.1 Limits and concerns

Each marker is trackable by OptiTrack system, as long as it could be seen by at least two of the cameras. However, there exist some concerns that lead to occlusions in the markers position. Some times for example when the arm comes up, one of the marker points on the head or hand might be hidden between head and arm, and the cameras might not be able to track the marker point for less than a second but a lot of frames. Those occlusions gaps can be filled by interpolation. However, this would not be real data captured by OptiTrack system. Therefore, we don't use this option of OptiTrack system. However, we did interpolate the data for simplifying the differentiation but at the end of calculations we removed the frame data, which were produced by interpolation.

The high speed of a player delivering a pitch holds for high velocity of segments accelerating and vanishing in a very short span in time and therefore tracking the segment with camera tracking requires high frame rate of video recording and with IMU requires fast and sensitive IMU sensors. The maximum resolution of the Optitrack system cameras is 120Hz, which provides a high level of motion capture resolution (There exist motion tracking systems with higher sampling frequency up to 300 Hz).

Pitches of professional baseball players are recorded to reach a ball velocity of around 170 [km/h], which is 1 meter per 44ms. Besides, we know that the ball velocity is roughly matching the maximum velocity of hand. This means OptiTrack system registers only 5 frames when the pitcher hand moves 1 meter and whatever happens in between those 5 fames is not recorded. The sampling frequency of 120 Hz is adequate for method development but too slow for capturing the pitches of professional baseball players, where we are specifically interested to explore the kinematic of the player at a few milliseconds when the power build in body reach to its maximum and to present the fastball.

Therefore, the used Optitrack device for tracking baseball pitchers may not be appropriated. The IMU sensors with sampling frequency of 500 Hz would register 22 frames per meter, which is a frame for each 4.5 cm. Therefore, the used IMU sensors setup for tracking baseball pitchers might be appropriated.

3.2.4 Synchronization

The data of the IMU sensors has been acquired for each IMU for around 1 hour. The trigger IMU data has been used to separate the trials related to the acquired data by the OptiTrack system. The trigger signal is registered in external port A6 of the extra IMU connected to the OptiTrack HUB. Figure 3-7 shows the trigger signal.

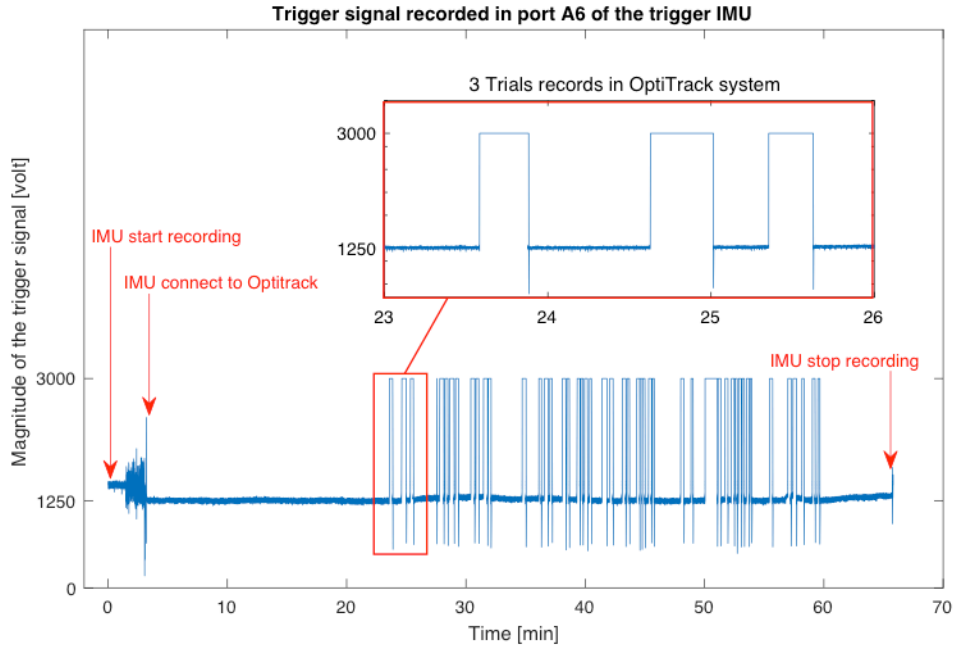

Figure 3-7 Trigger signal recorded on the trigger IMU is used to synchronize OptiTrack system with IMU sensors

The trigger is identifying as each recording by OptiTrack is registered by constant value of 3000 mV (3 volt). Each time that the magnitude of the trigger signal is above 2750 mV (a magnitude under 3000) the data has been set as the new trial. The new trial ends when the magnitude of the trigger signal drops and became smaller than 2750 mV. The data between the trials are not needed, since we do not have their correspondent measurement by OptiTrack system.

3.2.4.1 Limits and concerns

IMU's acquisition data is at 500Hz (sampling time of 2ms), while the OptiTrack record the motion at 120Hz (sampling time of 8.3ms). This may result in an error of synchronization that can exceed up to the 8.3ms. Further, the 16 cameras are also synchronised with each other, which can results in tracking error. The IMU's also needs to synchronize with each other that means the synchronization between IMU's also may introduce a shift in their recordings of up to 2ms (since sampling time is 2ms).

The acquisition frequency was set to 500 Hz. However, each IMU has its own internal clock and use computer clock for between IMU sensors synchronization. Consequently, acquisition frequencies between IMU sensors slightly differ from the 500 Hz. In order to solve this problem all the IMU's data have been interpolated into the time vector of the trigger IMU.

Chapter 4

Analysis method

In this chapter, the method used to compute the kinematics, kinetics and power flow of the subject from the measurement data is explained.

4.1 Kinematics analysis

The kinematics computation includes estimation of joint angles, angular velocities and angular accelerations for both IMU- and marker-based methods. To perform the computation, first we need to choose a kinematic representation:

Kinematics of segments is represented by the translation and rotation of LCS with respect to GCS. The translations of each segment are defined by the position of the origin of its LCS, this origin being the proximal joint centre. The most common method to represent rotation is Euler angles defined as angles of the three axes of LCS with respect to the three axes of the GCS (Wu, Van Der Helm et al. 2005). To choose the order of rotations, we refer to Wu's recommendations for standardization in the reporting of kinematic data. According to this standard order of rotation for reporting the joints rotation of this project we have the followings: shoulder rotation order is Y-X-Y and the other joints (elbow, wrist, hip, knee, ankle and lumbar joint) rotation order is Z-X-Y. (Wu and Cavanagh 1995).

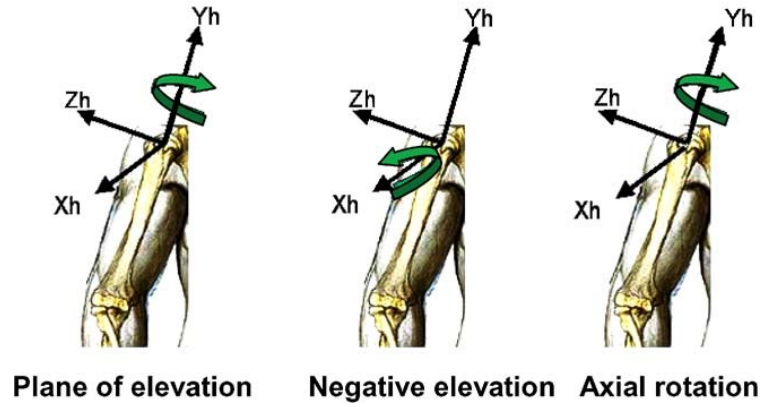

Figure 4-1 A rotation angles definition for upper arm ("h" stands for humours). The figure is modified from: (Wu, Van Der Helm et al. 2005), h: humours

Euler angle representation is a three-parameter kinematic representation, which is the minimal representation of the kinematic expressing only the rotation. The disadvantage of using Euler angles is that singularity may occur when transforming from one coordinate system to another (Gimbal-lock). When the movement is known, we can change the rotation order definition to prevent the singularity. The disadvantage of this approach is that we need to use different sequence for different motions and that the joint angle depends on the sequence (Wu, Van Der Helm et al. 2005).

Hence, no three-parameters set can be both global and non-singular. A different way to avoid singularity is to use an alternative representation called quaternion. A quaternion is a set of four parameters expressing rotation. Any rotation in 3D can be represented as a combination of an axis vector and a rotation angle, as Figure 4-2 shows. Quaternion gives a simple way to represent this axis-angle representation with four parameters and apply the corresponding rotation to a position vector representing a point relative to the origin in 3D.

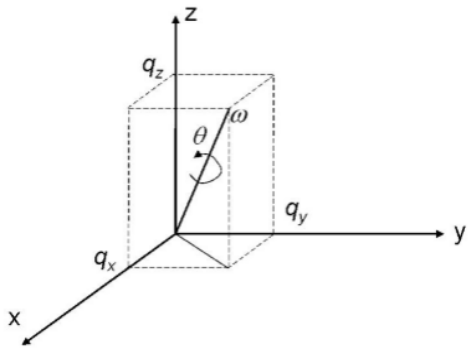

Figure 4-2 Quaternion rotations representation

Quaternion (q) is a vector quantity of the form:

$$q = \begin{bmatrix} q_\omega & q_x & q_y & q_z \end{bmatrix}^T \tag{3}$$

IMU records the orientation of a segment with respect to its initial orientation. Hence, a single segment in space has three degree of freedom in rotations. However since four parameters are used to define a state with three degree of freedom, they are not independent (Dirkx 2011). This dependency (which is defined by $\|q\| = 1$), results in preforming very smooth resampling and gap fillings, when interpolating between two rotations in 3D space (Thalmann and Thalmann 1993). This property is very useful to deal with the occlusion that occurs very often in in motion capture in 3D space (see appendix 1 for more equations of quaternion).

Nevertheless, the disadvantage of quaternion is that the parameters do not have a clear physical interpretation, like Euler angles do. Therefore, in order to represent every possible configuration and also prevent singularities we choose to use quaternions representation for computation and Euler angles for data presentation and analysis of results.

4.1.1 Kinematic estimation for marker-based method

As it was mentioned in chapter 3, the marker positions are defined in a global coordinate system (GCS). Based on the marker positions, the segments and their local coordinate system of in the global coordinate systems (LCS in GCS) can be defined. The local coordinate system of each segment in the global coordinate system defines the orientation of the segments with respect to the global coordinate system ($R_{GCS \rightarrow LCS}$). These steps are explained in 4.1.1.1. Having these for every two adjacent segment, joint angles can be computed. This step is explained in 4.1.1.2. Having these all the angular velocity and accelerations for joints and segments can be computed. This step is explained in 4.1.1.2.

4.1.1.1 Segments local coordinate system

4.1.1.1.1 Joint centre

The origin of each segments local coordinate system (LCS) is at the proximal joint centre apart from the thorax. The joint centres (JC) are estimated with regression equations that model the relation between markers positions on the skin and the joint centres. The accuracy of joint centres is dependent on the accuracy of positioning the markers on anatomical landmarks and the morphology of the subject (Wu and Cavanagh 1995, Wu, Siegler et al. 2002, Wu, Van Der Helm et al. 2005).

In this study, the locations of joints are estimated based on position of markers and measurements of previous studies collected by Reed and McConville and modified approach of Dumas et al. 2007 on Reed et al 1999 data (McConville, Clauser et al. 1980, Reed, Manary et al. 1999, Dumas, Aissaoui et al. 2005, Dumas, Chèze et al. 2007, Dumas, Cheze et al. 2007).

Distal positions are computed using the position of the proximal joint centre and the segment orientation in an iterative way.

4.1.1.1.1.1 Cervical joint centre (CJC) and right Shoulder joint centre (RSJC)

The location of cervical joint centre (CJC) and right shoulder joint centre (RSJC) are estimated based on positions of following markers: 7th Cervicale (C7), the Incisura Jugularis (IJ), 8th Thoracic Vertebra (T8), Processus Xiphoideus (PX), right Acromion (RA).

The computation of CJC and RSJC are similar. The distance between marker positions and these two joint centres are scaled by the thorax width ($l_c = IJ - C7$).

For an average size male, CJC and RSJC are estimated by regression as follows:

- CJC is to be defined by a vector in the sagittal plane from C7 with an angle of 8° (above the line through C7 and IJ) and the vector length is 55% of l_c.
- RSJC is to be defined by a vector in a plane parallel to the sagittal plane from RA with an angle of -11° (under the RA) and 43% of l_c. Whereas, the sagittal plane goes through C7, IJ, T8 and PX.

4.1.1.1.1.2 Lumbar joint centre (LJC) and left hip joint centres (LHJC)

The location of the lumbar joint centre (LJC) and left hip joint centres (LHJC) are estimated based on the location of Anterior Superior Iliac Spines (RASIS and LASIS), posterior Superior Iliac Spines (RPSIS and LPSIS) and their middle points (MASIS and MPSIS).

The computation of LJC and LHJC are similar. The distance between marker positions and these two joint centres are scaled by the pelvis width ($l_p = RASIS - LASIS$).

- According to Dumas et al 2007 based on McConville et al data, for an average size male, LJC is estimated by regression using a vector from MASIS with the length of vector being -26.8%, 0% and 12.8% of l_p, respectively on the X, Y, and Z-axes of the pelvis LCS (The Z-axis runs from LASIS to RASIS. The Y-axis is normal to the plane containing LASIS, RASIS and MPSIS. The X-axis is the cross product of Y and Z-axes).

However, we used a slightly different routine, to minimise the soft tissue artefacts. l_p has been normalized by previous data ($r_p = mean(\|RASIS - LASIS\|) / \|RASIS_{mc} - LASIS_{mc}\|$). Where $RASIS_{mc}$ and $LASIS_{mc}$ are the Anterior Superior Iliac Spines data from McConville et al. 1999 used as reference geometry. The data from McConville contain the four iliac spines and hip joint centre. Thus, the position of the hip joint centre from RASIS, LASIS and MASIS by using r_p as a scaling factor can be determined in a local coordinate system linked to the pelvis. The position of

LJC is computed as the mean of the positions estimated from the three anatomical landmarks (RASIS, LASIS and MPSIS) by:

$$LJC = \frac{\left[\left(RASIS - r_p.RASIS_{mc}\right) + \left(LASIS - r_p.LASIS_{mc}\right) + \left(MPSIS - r_p.MPSIS_{mc}\right)\right]}{3} \quad (4)$$

- According to Dumas et al 2007 based on McConville et al data, for an average size male, LHJC is estimated by regression using a vector from MASIS with the length of vector being -20.8%, -36.1% and -28.3% of l_p, respectively on the X, Y, and Z-axes of the pelvis LCS (The Z-axis runs from LASIS to RASIS. The Y-axis is normal to the plane containing LASIS, RASIS and MPSIS. The X-axis is the cross product of Y and Z-axes).

Similar to the LJC in order to minimise the soft tissue artefacts, the position of LHJC is computed as the mean of the distance estimated from three anatomical landmarks (RASIS, LASIS and LJC) and the McConville ones, using r_p as the scaling factor by:

$$LHJC = \frac{\left[\left(RASIS + r_p.\left(LHJC_{mc} - RASIS_{mc}\right)\right) + \left(LASIS + r_p.\left(LHJC_{mc} - LASIS_{mc}\right)\right) + \left(LJC + r_p.LHJC_{mc}\right)\right]}{3} \quad (5)$$

4.1.1.1.1.3 Elbow, Wrist, Knee and Ankle Joint Centres (REJC, RWJC, LKJC, LAJC)

The computation of the right elbow, right wrist, left knee and left ankle joint centres (REJC, RWJC, LKJC and LAJC) are similar:

- Right wrist joint centre (RWJC) is estimated as the midpoint between the right Radial and Ulnar Styloid Process (RRS and RUS).
- Right elbow joint centre (REJC) is estimated as the midpoint between right Lateral and Medial Humeral Epicondyle (RLHE and RMHE).
- Left knee joint centre (LKJC) is estimated as the midpoint between left Lateral and Medial Femoral Epicondyles (LLFE and LMFE).
- Left ankle joint centre (LAJC) are estimated as midpoint between left medial (LMM) and Lateral Malleous (LLM)

4.1.1.1.2 Segments LCS

4.1.1.1.2.1 Thorax

The thorax coordinate system is defined based on the position of the following markers: 7th cervicale (C7), incisura jugularis (IJ), 8th Thoracic vertebra (T8), processus xiphoideus (PX).

The origin of the thorax coordinate system is CJC and its axes are defined as follow: The Y-axis runs from middle point of PX and T8 to the middle point of C7 and IJ. The Z_{temp}-axis is computed as the cross product of two vectors from middle point of PX and T8 to IJ and to C7. The X-axis is defined as the cross product of Y and Z_{temp}-axis. Subsequently, the Z-axis is defined as cross product of the X and Y-axis.

$$LCS_{thorax}: \begin{cases} \mathbf{y}_{thorax} = \left(\left(IJ+C7\right)/2 - \left(PX+T8\right)/2\right) / \left\| \left(IJ+C7\right)/2 - \left(PX+T8\right)/2 \right\| \\ \mathbf{z}_{temp} = \left(IJ - \left(PX+T8\right)/2\right) \times \left(C7 - \left(PX+T8\right)/2\right) \\ \mathbf{x}_{thorax} = \left(\mathbf{y}_{thorax} \times \mathbf{z}_{temp}\right) / \left\| \mathbf{y}_{thorax} \times \mathbf{z}_{temp} \right\| \\ \mathbf{z}_{thorax} = \mathbf{x}_{thorax} \times \mathbf{y}_{thorax} \end{cases} \quad (6)$$

4.1.1.1.2.2 Right upper arm

The right upper arm coordinate system is defined based on the position of the following markers: right shoulder joint centre (RSJC), right medial humeral epicondyle (RMHE), right lateral humeral epicondyle (RLHE) and their middle point which is the right elbow joint centre (REJC).

The origin of right upper arm coordinate system is RSJC and its axes are defined as follows: The Y-axis runs from REJC to RSJC. The Z_{temp}-axis runs from RMHE to RLHE. The X-axis is to find as the cross product of the Y- and Z_{temp}-axis. The Z-axis is to find as the cross product of the X- and Y-axis.

$$LCS_{upperarm}: \begin{cases} \mathbf{y}_{upperarm} = (RSJC - REJC) / \left\| RSJC - REJC \right\| \\ \mathbf{z}_{temp} = RLHE - RMHE \\ \mathbf{x}_{upperarm} = \mathbf{y}_{upperarm} \times \mathbf{z}_{temp} / \left\| \mathbf{y}_{upperarm} \times \mathbf{z}_{temp} \right\| \\ \mathbf{z}_{upperarm} = \mathbf{x}_{upperarm} \times \mathbf{y}_{upperarm} \end{cases} \quad (7)$$

4.1.1.1.2.3 Right lower arm

The right lower arm LCS is defined based on the position of the following markers: Right Ulnar Styloid (RUS), Right Radial Styloid (RRS) their middle point which is the Right Wrist and Elbow Joint Centre (RWJC and REJC).

The origin of right lower arm LCS is REJC and its axes are defined as follows: The Y-axis runs from RWJC to REJC. The Z_{temp}-axis runs from RUS to RRS. The X-axis is to find as the cross product of the Y- and Z_{temp}-axis. The Z-axis is to find as the cross product of the X- and Y-axis.

$$LCS_{lowerarm}: \begin{cases} \mathbf{y}_{lowerarm} = (REJC - RWJC) / \left\| REJC - RWJC \right\| \\ \mathbf{z}_{temp} = RRS - RUS \\ \mathbf{x}_{lowerarm} = \mathbf{y}_{lowerarm} \times \mathbf{z}_{temp} / \left\| \mathbf{y}_{lowerarm} \times \mathbf{z}_{temp} \right\| \\ \mathbf{z}_{lowerarm} = \mathbf{x}_{lowerarm} \times \mathbf{y}_{lowerarm} \end{cases} \quad (8)$$

4.1.1.1.2.4 Right hand

The right hand coordinate system is defined based on the position of the following markers: right hand 2nd and 5th metacarpal (RMH2 and RMH5), right ulnar styloid (RUS), right radial styloid (RRS) and the middle point of RUS and RRS which is the wrist joint centre (RWJC).

The origin of right hand coordinate system is RWJC and its axes are defined as follows: The Y-axis runs from the middle point of RMH2 and RMH5 to REJC. Similar to the lower arm, Z_{temp}-axis runs from RUS to RRS. The X-axis is to find as the cross product of the Y- and Z_{temp}-axis. The Z-axis is to find as the cross product of the X- and Y-axis.

$$LCS_{hand}: \begin{cases} \mathbf{y}_{hand} = (RWJC - (RMH2 + RMH5)/2) / \left\| RWJC - (RMH2 + RMH5)/2 \right\| \\ \mathbf{z}_{temp} = RRS - RUS \\ \mathbf{x}_{hand} = \mathbf{y}_{hand} \times \mathbf{z}_{temp} / \left\| \mathbf{y}_{hand} \times \mathbf{z}_{temp} \right\| \\ \mathbf{z}_{hand} = \mathbf{x}_{hand} \times \mathbf{y}_{hand} \end{cases} \quad (9)$$

4.1.1.1.2.5 Pelvis

The pelvis coordinate system is defined based on the position of the following markers: right and left anterior superior iliac spines (RASIS and LASIS), right and left posterior superior iliac spines (RPSIS and LPSIS) and their middle points (MASIS and MPSIS).

The origin of pelvis coordinate system is LJC and its axes are defined as follows: The Z-axis runs from RASIS and LASIS. The Y_{temp}-axis is defined as the cross product of two vectors that run from RASIS and LASIS to the middle point of RPSIS and LPSIS (MPSIS). The X-axis is the cross product of the Y- and Z-axis. The Y-axis is the cross product of the Z- and X-axis.

$$LCS_{pelvis}: \begin{cases} \mathbf{z}_{pelvis} = (RASIS - LASIS) / \left\| RASIS - LASIS \right\| \\ \mathbf{y}_{temp} = ((RASIS - MPSIS) \times (LASIS - MPSIS)) \\ \mathbf{x}_{pelvis} = \mathbf{y}_{temp} \times \mathbf{z}_{pelvis} / \left\| \mathbf{y}_{temp} \times \mathbf{z}_{pelvis} \right\| \\ \mathbf{y}_{pelvis} = \mathbf{z}_{pelvis} \times \mathbf{x}_{pelvis} \end{cases} \quad (10)$$

4.1.1.1.2.6 Left thigh

The left thigh coordinate system is defined based on the position of the following markers: left hip and knee joint centres (LHJC and LKJC), left medial femoral epicondyle (LMFE), left lateral femoral epicondyle (LLFE).

The origin of left thigh coordinate system is LHJC and its axes are defined as follows: The Y-axis runs from RKJC to RHJC. The Z_{temp}-axis runs from LLFE to LMFE. The X-axis is to find as the cross product of the Y- and Z_{temp}-axis. The Z-axis is to find as the cross product of the X- and Y-axis.

$$LCS_{thigh} : \begin{cases} \mathbf{y}_{thigh} = (LHJC\text{-}LKJC) / \left\| LHJC\text{-}LKJC \right\| \\ \mathbf{z}_{temp} = LLFE\text{-}LMFE \\ \mathbf{x}_{thigh} = \mathbf{y}_{thigh} \times \mathbf{z}_{temp} / \left\| \mathbf{y}_{thigh} \times \mathbf{z}_{temp} \right\| \\ \mathbf{z}_{thigh} = \mathbf{x}_{thigh} \times \mathbf{y}_{thigh} \end{cases} \quad (11)$$

4.1.1.1.2.7 Left shank

The left shank coordinate system is based on the position of the following markers: left knee and ankle joint centre (LKJC and LAJC), left fibula head (LFH), left medial malleolus (LMM), left lateral malleolus (LLM).

The origin of left shank coordinate system is LKJC and its axes are defined as follows: The Y-axis runs from LAJC to LKJC. The X_{temp}-axis is normal to plane containing the LKJC, LAJC and LFH pointing anteriorly. The Z-axis is the cross product of the X_{temp} and Y-axis. The X-axis is to find as the cross product of the Y- and Z-axis.

$$LCS_{shank} : \begin{cases} \mathbf{y}_{shank} = (LKJC - LAJC) / \left\| LKJC - LAJC \right\| \\ \mathbf{x}_{temp} = (LFH - LAJC) \times (LKJC - LAJC) \\ \mathbf{z}_{shank} = \mathbf{x}_{temp} \times \mathbf{y}_{shank} / \left\| \mathbf{x}_{temp} \times \mathbf{y}_{shank} \right\| \\ \mathbf{x}_{shank} = \mathbf{y}_{shank} \times \mathbf{z}_{shank} \end{cases} \quad (12)$$

Figure 4-3 shows an overview of the approach of this project as explained in section 4.1.1 to estimate joints positions and coordinate system of body segments.

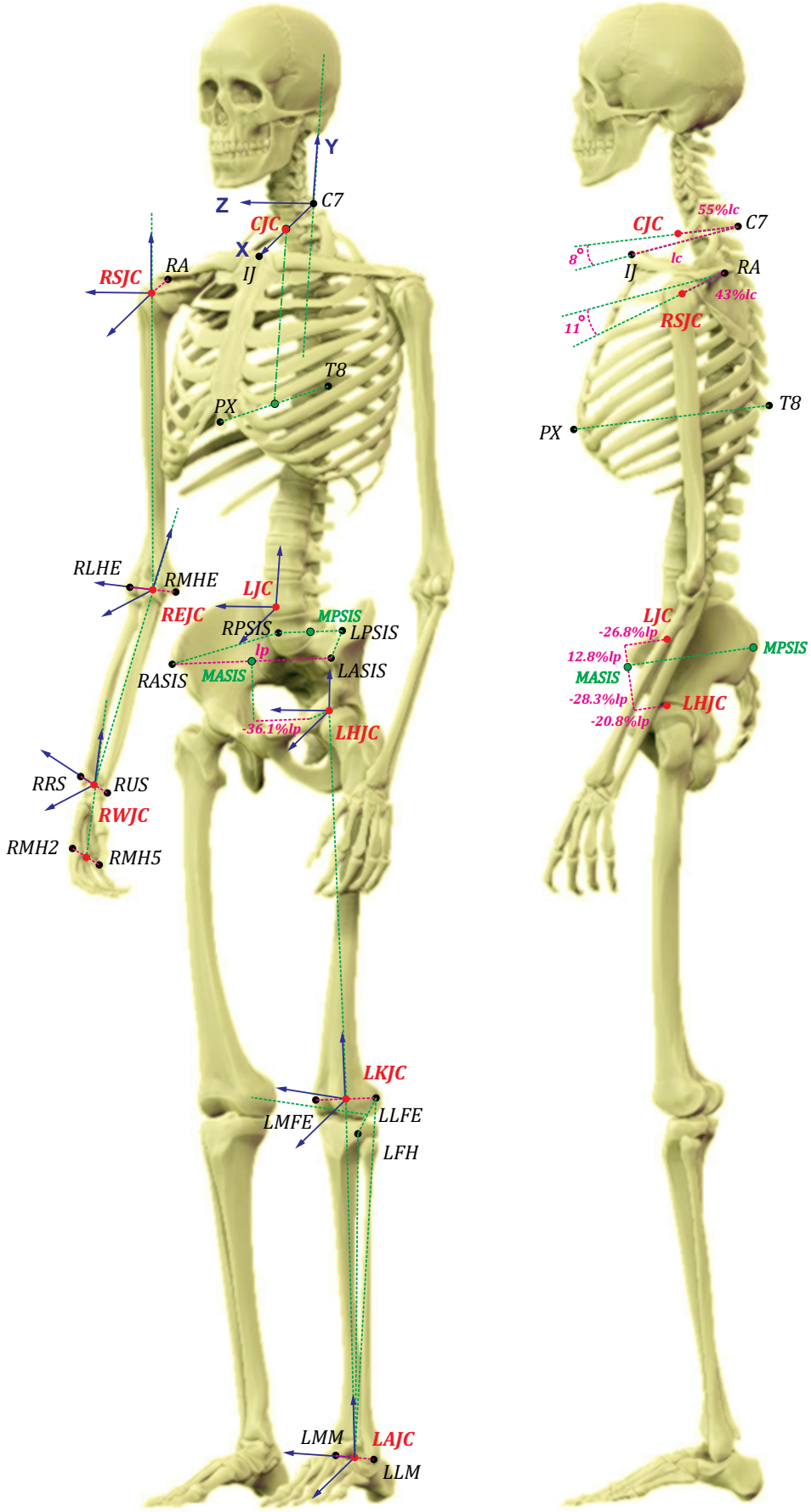

Figure 4-3 Estimating coordinate system of segments and joint centres based on regression (Dumas, Cheze et al. 2007)

4.1.1.2 Joints rotation

Wu defines the joint rotation as: "The rotation of a distal body segment with respect to the proximal segment" (Wu and Cavanagh 1995). This definition is usually used in human motion analysis. Based on this definition and having the LCS of segments (section 4.1.1.1), joint angles can be denoted as the rotation from the LCS of each proximal segment to its distal segment ($R_{LCS_{pro} \rightarrow LCS_{dis}}$).

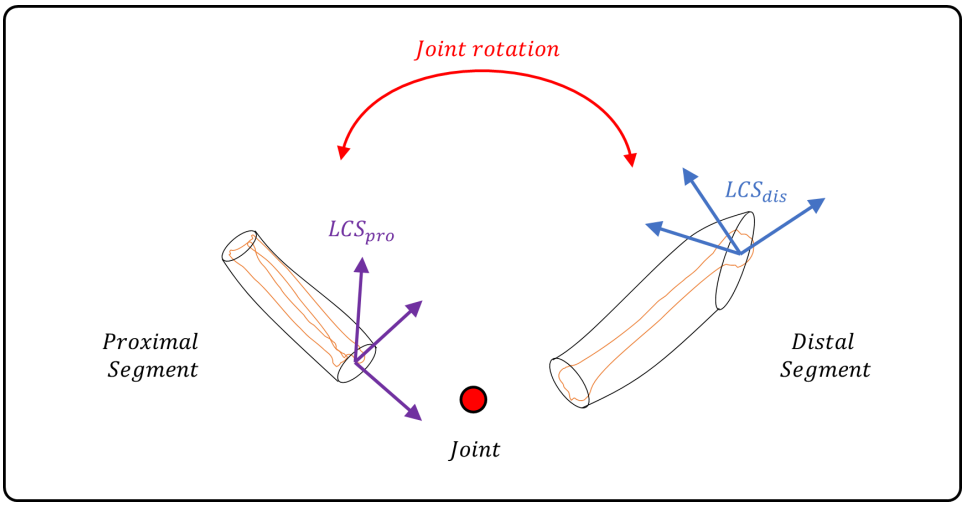

Figure 4-4 Representation of joint rotations by local coordinate system of proximal to distal segment

Mathematically the joint rotations can be computed as follow:

$$R_{LCS_{pro} \rightarrow LCS_{dis}} = R^{-1}_{GCS \rightarrow LCS_{pro}} * R_{GCS \rightarrow LCS_{dis}} \quad (13)$$

Whereas $R_{GCS \rightarrow LCS_{dis}}$ is the rotation matrix from the global coordinate system to the local coordinate system of the distal segment (LCS_{dis}). $R^{-1}_{GCS \rightarrow LCS_{pro}}$ is the inverse of the rotation matrix from the global coordinate system to the local coordinate system of the proximal segment which is equivalent to $R_{LCS_{pro} \rightarrow GCS}$. This estimated rotation between the proximal to distal segments, can be converted to Euler angles and quaternions ($q_{LCS_{pro} \rightarrow LCS_{dis}}$).

4.1.1.3 Joints angular velocity and acceleration

The rate of change of each joint angle (angular velocity ω of each joint), can be computed by differentiating the quaternions of the joint ($q_{LCS_{pro} \rightarrow LCS_{dis}}$), according to:

$$\omega_q = \begin{bmatrix} 0 \\ \omega \end{bmatrix} = 2\dot{q} \otimes \overline{q} \quad (14)$$

Where: $\otimes$ is the quaternion product (appendix1), $\omega = \begin{bmatrix} \omega_x & \omega_y & \omega_z \end{bmatrix}^T$ and $\overline{q}$ is the conjugate of the quaternion and $\dot{q}$ is the first derivative of q with respect to time. The complex conjugate of quaternion (represent rotation from A to B) defines the inverse of the rotation (represent rotation from B to A): $\overline{q}_{A \rightarrow B} = q_{B \rightarrow A}$

Subsequently, the rate of change of the angular velocity (angular acceleration $\dot{\omega}$ of each joint), can be computed by double differentiation of the joint quaternions, as follow:

$$\dot{\omega}_q = \begin{bmatrix} 0 \\ \dot{\omega} \end{bmatrix} = 2\left(\ddot{q} \otimes \overline{q} + \dot{q} \otimes \dot{\overline{q}}\right) \tag{15}$$

4.1.1.4 Segments angular velocity and acceleration

The same routine (using equation 14 and 15) can also be used to compute the segment's angular velocity and acceleration in GCS by differentiating the quaternions of the segments. The angular velocity and accelerations of the segments in global coordinate system, were transformed into the local coordinate system of the segments via:

$$\begin{aligned} \omega_{LCS} &= R_{LCS \to GCS} * \omega_{GCS} = R^{-1}_{GCS \to LCS} * \omega_{GCS} \\ \dot{\omega}_{LCS} &= R_{LCS \to GCS} * \dot{\omega}_{GCS} = R^{-1}_{GCS \to LCS} * \dot{\omega}_{GCS} \end{aligned} \tag{16}$$

4.1.1.5 Overview

Figure 4-5 shows the routine to compute the segment and joint kinematics from markers positions.

The marker positions are measured by Optitrack system in the global coordinate system (GCS). Based on the marker positions, the segment's local coordinate system of in the global coordinate systems (LCS in GCS) can be defined. The local coordinate system of each segment in the global coordinate system defines the rotation ($R_{GCS\rightarrow LCS}$) and orientation ($q_{GCS\rightarrow LCS}$) of the segments with respect to the global coordinate system. Having $R_{GCS\rightarrow LCS}$ for every two adjacent segment (proximal and distal), their relative orientation and the joint angle can be computed. Having orientation changes q and its derivatives, the angular velocity and accelerations of segments and joints ($\omega_s, \omega_j, \alpha_s$ and α_j) have been estimated.

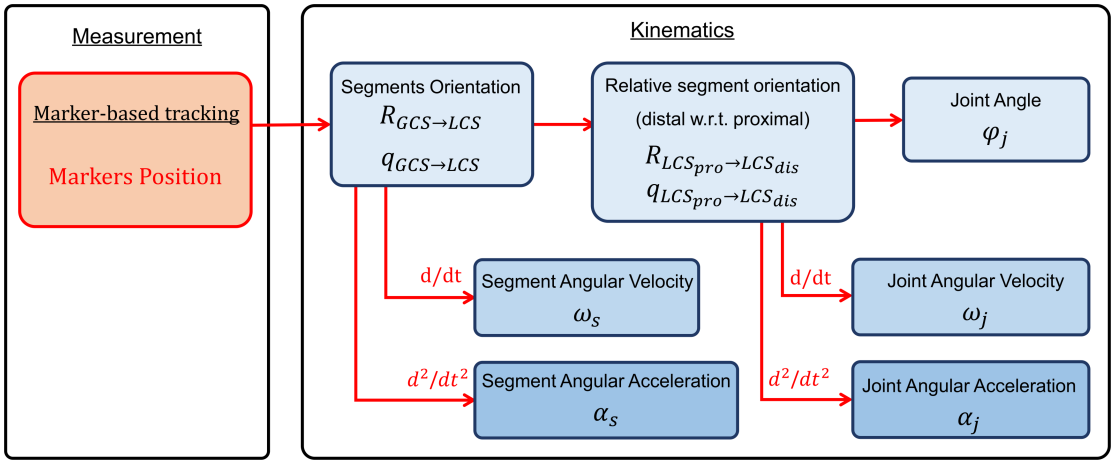

Figure 4-5 Schematic view of kinematic computation routine from the markers positions data.

In order to make the marker-based kinematic comparable with the IMU-based method, the kinematic computed with respect to the LCS of the segments are transformed to the FCS of the segments.

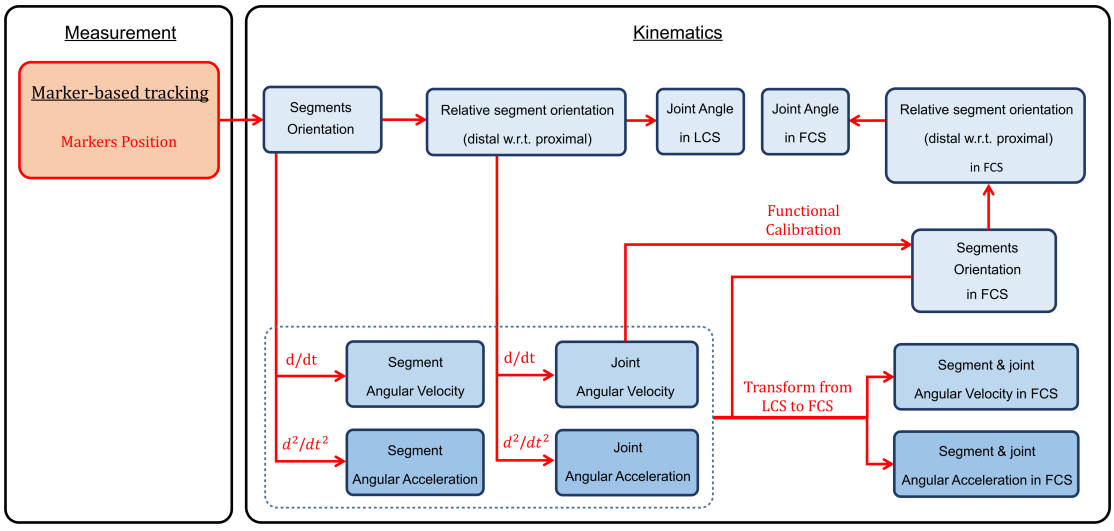

Figure 4-6 Joint rotation calculation routine Marker-based data with functional calibration

4.1.2 Kinematic estimation for IMU-based method

As it was mentioned in chapter 2 (section 2.2.3.2), the orientation of each segment is computed by combining measured the angular velocity, linear accelerations and magnetic field by an IMU. These data are measured in the local coordinate systems of each IMU itself (MCS).

Movements soliciting only one degree of freedom of a joint at a time are used to reveal the joint functional axis and to define a functional coordinate system (FCS). Note that ideally the LCS computed with the markers is aligned with the FCS computed by functional calibration. However, since most likely it is not the case, they are entitled with different names.

The transformation of IMU data (measured in MCS) to the FCS is represented by $R_{MCS \rightarrow FCS}$. This relative orientation of the FCS with respect to the MCS is assumed to be constant due to the hypothesis of rigid segment. This step is explained in 4.1.2.1.

Having this transformation matrix, the angular velocity recorded by the IMU in the MCS can be transformed to the FCS, which would be the angular velocity of the segment. This step is explained in 4.1.2.2.

Further, the orientation of the IMU with respect to its initial orientation can be computed using a strap-down integration algorithm. Having these and the initial orientation, we can compute the joint angle. This step is explained in 4.1.2.3.

4.1.2.1 Segments local coordinate system

4.1.2.1.1 Joint centres and segment length

The segment length in the marker data is the mean of the distance between the joint centres during the measurement. However, computing the segments length from the IMU data is not such a trivial problem as from the marker based data as the IMU only measure orientation and not position.

The studies of Seel et al. introduced a method to estimate the distance from IMU to the joint centres (Seel, Schauer et al. 2012, Seel, Raisch et al. 2014, Schauer and Seel 2016, Seel 2016). In this method the IMU sensors are attached to body segments and the skin movement are neglected. Accordingly, it is assumed that the distance of the IMU to the adjacent joints remains constant during motion.

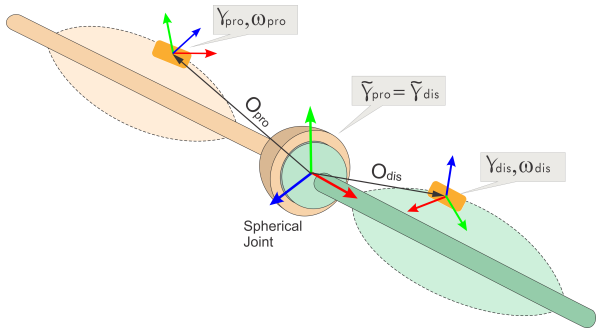

Figure 4-7 Distance between joint centre and IMU sensors on two adjacent segments (O_{pro} and O_{dis})

Considering a spherical joint, the acceleration of each IMU sensor can be defined as the sum of the joint centre acceleration and radial and tangential accelerations due to the rotation of each IMU around the joint centre:

$$\begin{aligned} \gamma_{pro}(t) &= \tilde{\gamma}_{pro}(t) + \omega_{pro}(t) \times \left[\omega_{pro}(t) \times O_{pro}\right] + \dot{\omega}_{pro}(t) \times O_{pro} \quad \forall t \\ \gamma_{dis}(t) &= \tilde{\gamma}_{dis}(t) + \omega_{dis}(t) \times \left[\omega_{dis}(t) \times O_{dis}\right] + \dot{\omega}_{dis}(t) \times O_{dis} \quad \forall t \end{aligned} \tag{17}$$

$\gamma(t)$: Recorded segments acceleration by IMU; $\tilde{\gamma}(t)$: Joint center acceleration; $\omega(t) \times [\omega(t) \times O]$: Centrifugal acceleration; $\dot{\omega}(t) \times O$: Tangential acceleration

Accordingly, the joint's acceleration may be defined by shifting the measured accelerations into the joint centre:

$$\begin{aligned} \tilde{\gamma}_{pro}(t) &= \gamma_{pro}(t) - \left(\omega_{pro}(t)\times\left[\omega_{pro}(t)\times O_{pro}\right] + \dot{\omega}_{pro}(t)\times O_{pro}\right) \quad \forall t \\ \tilde{\gamma}_{dis}(t) &= \gamma_{dis}(t) - \left(\omega_{dis}(t)\times\left[\omega_{dis}(t)\times O_{dis}\right] + \dot{\omega}_{dis}(t)\times O_{dis}\right) \quad \forall t \end{aligned} \tag{18}$$

Note that in these equations the IMU data are expressed in the IMU's coordinate systems of the proximal and distal (MCS_{pro} and MCS_{dis}). Since $\tilde{\gamma}_{pro}$ and $\tilde{\gamma}_{dis}$ represent the same quantity (acceleration of the joint) estimated based on data measured by two IMU's, these two equations should be equal. So, it can be written as the following constraint:

$$\tilde{\gamma}_{pro}(t) - \tilde{\gamma}_{dis}(t) = 0 \quad \forall t \tag{19}$$

Having accelerations (γ_{pro} and γ_{dis}) measured by accelerometers and angular velocities (ω_{pro} and ω_{dis}) measured by gyroscopes of the IMU sensors attached to the proximal and distal segments, we can implement an optimization algorithm for the in time varying recordings and solve for the two O_{pro} and O_{dis} vectors.

Some other literatures like Salehi et al. 2015 suggested to use an automatic optimization containing a model built up all the segments and all of the segments lengths would be computed at once with a constraint that the IMU needs to remains in a plane going through the two adjacent joints. It is suggested that this would help to compute a more accurate segment length (Salehi, Bleser et al. 2015).

It is also possible to use a trick to compute this vector indirectly. Like, Chen et al. 2013, which suggested a method to compute the upper and lower arm by two functional calibration movements of shoulder and elbow flexion and extension. As you can see in Figure 4-8, using shoulder flexion/ extension the distance between the IMU on the lower arm and shoulder can be defined and by subtracting this distance from the distance between the IMU and the elbow (found from the elbow flexion/extension) the upper arm length could be estimated (Chen 2013).

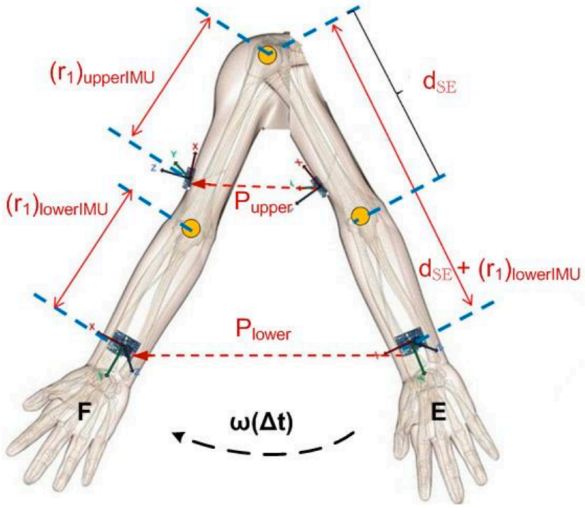

Figure 4-8 length estimation of upper and lower arm by **two functional calibration movements of shoulder and elbow flexion and extension (Chen 2013)**

Attempts to use this method have not been successful. The distance between shoulder joint and the IMU on the lower arm, which is around 55 cm according to the Optitrack reference, was estimated to be 45 cm in this case. The thorax was not moving in this trial and this can be the reason that the optimization did not work properly. Another possibility is that these dissimilarities might be due to the complex nature of shoulder joint.

Since the gyroscope and angular velocity data are measured in the two separated coordinate systems of the proximal and distal IMU sensors, (Salehi, Bleser et al. 2015) modified the previous equation by incorporating the relative orientations of these IMU sensors:

$$\tilde{\gamma}_{pro}(t) - q_{pro \to dis} \otimes \tilde{\gamma}_{dis}(t) = 0 \qquad \forall t \tag{20}$$

We also attempted to use this method and the results are consistent with and without this adaptation. It only results in longer optimization duration. Thus, we did not use this adaptation.

This optimization problem was implemented in MATLAB using *single global solution* solver, equipped with *fmincon* algorithm to find local solutions. Any other optimization method might also be employed as well. Gauss-Newton algorithm was used by (Seel, Raisch et al. 2014), *lsqnonlin* algorithm with Levenberg-Marquardt used by (Salehi, Bleser et al. 2015) and the results are similar. The global optimization with generic algorithm and multi-start search has a better performance in avoiding local minimum. When employing other algorithm, however the results were similar with the global algorithm, yet the output note the "*possible local minimum"*, which means the global optimization make authentic results.

Using two series of such optimizations, each segment length can be computed. For example, Figure 4-9 shows the computation of lower arm length using elbow and wrist flexion/extension.

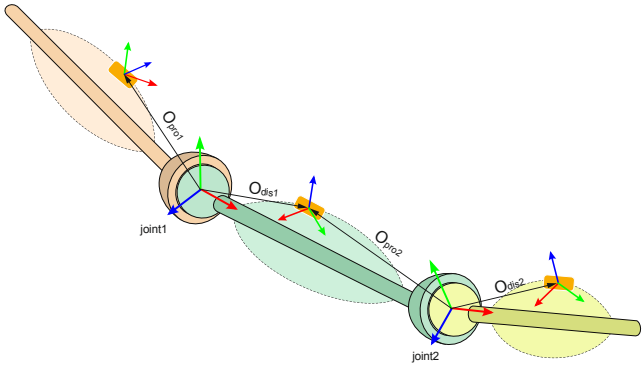

Figure 4-9 Segment length estimation having two vectors from the IMU on the lower arm w.r.t. to elbow and wrist.

4.1.2.1.2 Functional calibration

Movements with one degree of freedom of the joints are used to define the joint axes in the MCS and find the orientation of each IMU with respect to the segment's coordinate system (MCS w.r.t. FCS). This means that actually functional calibration defines the transformation of IMU data to the joint. Functional calibration will be used to compare the measurements of the Optitrack system with the IMU's one. Besides it gives also a better insight into the motion of the segments by reducing the cross talk of the axes.

Here as an example, the method of this study to find the coordinate system of forearm will be explained in detail in 4.1.1.1.1. This method is also verified with another method from literature (Seel, Schauer et al. 2012) which is shortly explained in 4.1.1.1.1.1. Using this this axes the rotation matrix from IMU to segment can be set up as explained in 4.1.1.1.1.2. This is followed by a suggested routine for all of the other segments.

4.1.2.1.2.1 Method1: Optimization

Another method to identify the joint axis is based on a physical fact that: "The projections of angular velocities measured by the IMU sensors on the two adjacent segments into the joint plane have the same length for each instant in time." In this study, the results have been also compared with this method. For a more detail description of this method refer to (Seel, Schauer et al. 2012).

4.1.2.1.2.2 Method2: 50% ω_{max}

The IMU mounted on the forearm records data with respect to MCS. Neither position nor orientation of MCS with respect to the forearm is known. The elbow joint is able to provides two movements: "pronation/supination" and "flexion/extension". The direction of the longitudinal axis of the forearm (Y-axis) can be found using the direction of the angular velocity during pronation and the opposite direction of angular velocity during supination.

$$\mathbf{y}_{forearm} \approx \left(\omega / \|\omega\|\right)_{pronation} \approx -\left(\omega / \|\omega\|\right)_{supination} \tag{21}$$

This method need prior knowledge of the orientation of the MCS on the segment, since when we are only looking into the IMU recordings offline, we do not know when is supination and when is pronation. In order to distinguish between these motions, you can look into the accelerations recordings to recognize the initial orientation of IMU regarding the gravity (which axis shows around 9.8 m/s²). From that initial orientation you can find out if the following movement is supination or pronation (Figure 4-10).

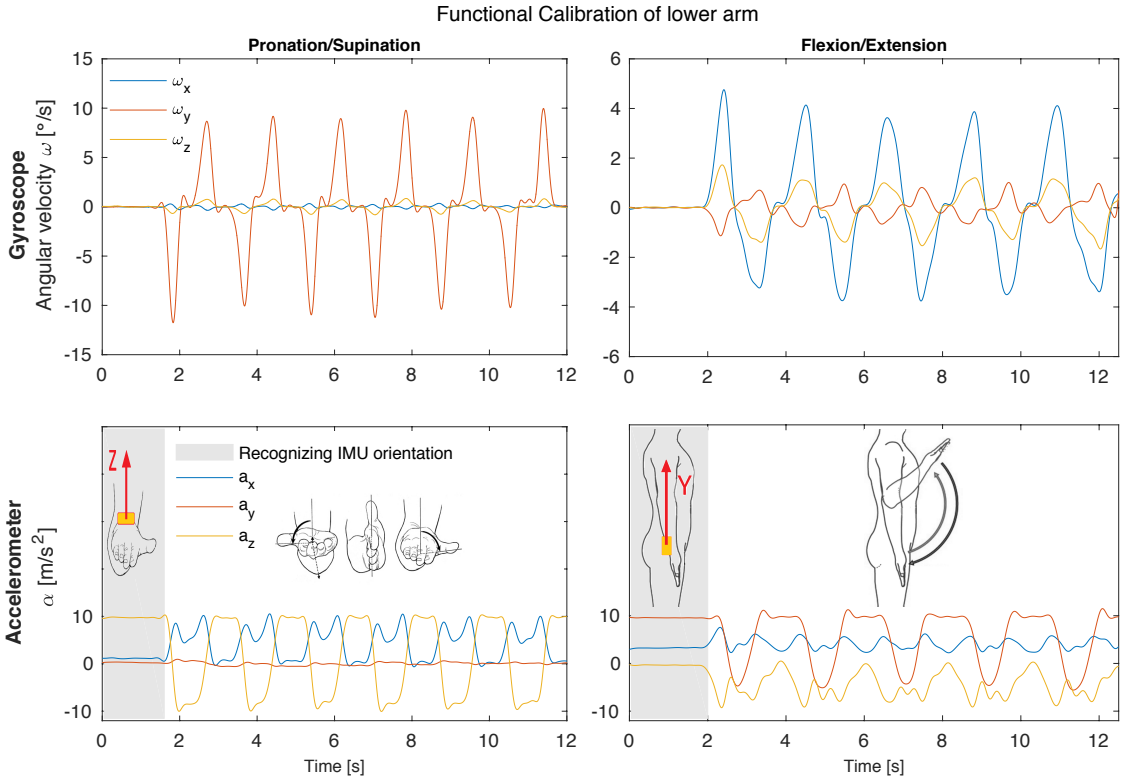

Figure 4-10 Distinguishing movements by identifying the initial orientation of IMU.

Since the subject preforms movements repeated after each other, when switching between rotation in two different directions (in this case pronation/supination), the angular velocity vector switch from one direction to another in a continuous way so at some point it is pointing in a direction that is not the functional axis. Therefore, it is needed to remove the switching parts in data. For this purpose, the pronation axis is computed as the mean of the angular velocities (ω) that are greater than 50% of the maximum angular velocity ($\omega > (\omega_{max}/2)$) during pronation and the supination axis is defined in the opposite direction based on all the angular velocities, which are smaller than 50% of the minimum angular velocity ($\omega < (\omega_{min}/2)$).

$$\text{axis}_{pronation-supination} = \left(\left(\omega / \|\omega\|\right)_{pronation|\omega>(\omega_{max}/2)} - \left(\omega / \|\omega\|\right)_{supination|\omega<(\omega_{min}/2)} \right) \Big/ 2 \tag{22}$$

The Y-axis direction is the normalised mean of these two directions.

$$\mathbf{y}_{forearm} = \text{axis}_{pronation-supination} \,/\, \left\| \text{axis}_{pronation-supination} \right\| \quad (23)$$

In Figure 4-11, five repeated pronation and supination is used to define the Y-axis as follow:

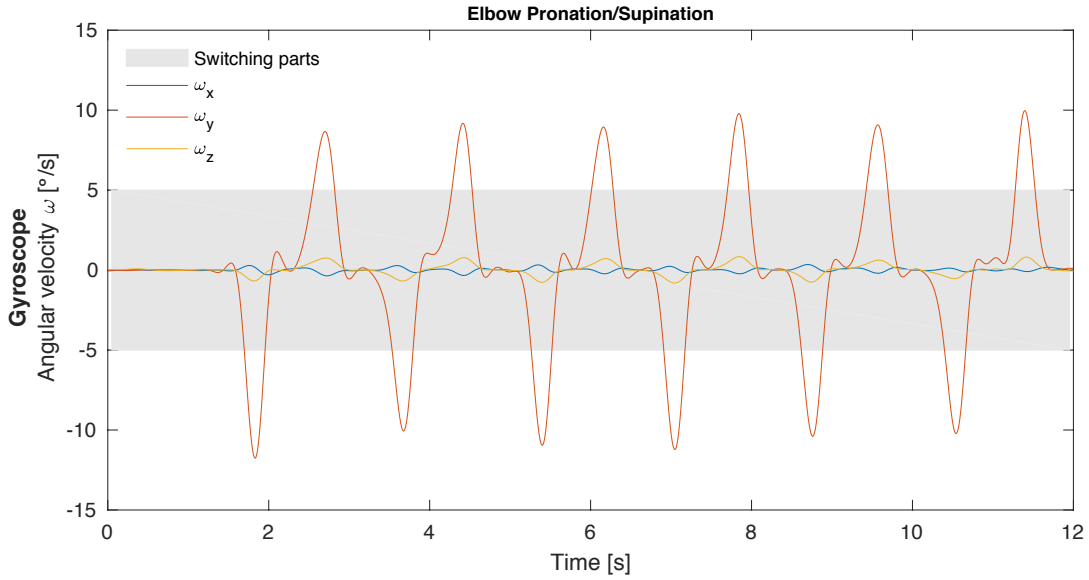

Figure 4-11 Removing switching parts from the angular velocity data for defining functional axis.

Accordingly, the direction of the Z-axis can be found using the direction of the angular velocity during elbow flexion and the opposite direction of angular velocity during elbow extension. Figure 4-12 represents this computation.

$$\text{axis}_{flexion-extension} = \left(\left(\omega / \left\| \omega \right\| \right)_{flexion | \omega > (\omega_{max}/2)} - \left(\omega / \left\| \omega \right\| \right)_{extension | \omega < (\omega_{min}/2)} \right) \Big/ 2 \quad (24)$$

$$\mathbf{z}_{forearm} = \text{axis}_{flexion-extension} \,/\, \left\| \text{axis}_{flexion-extension} \right\|$$

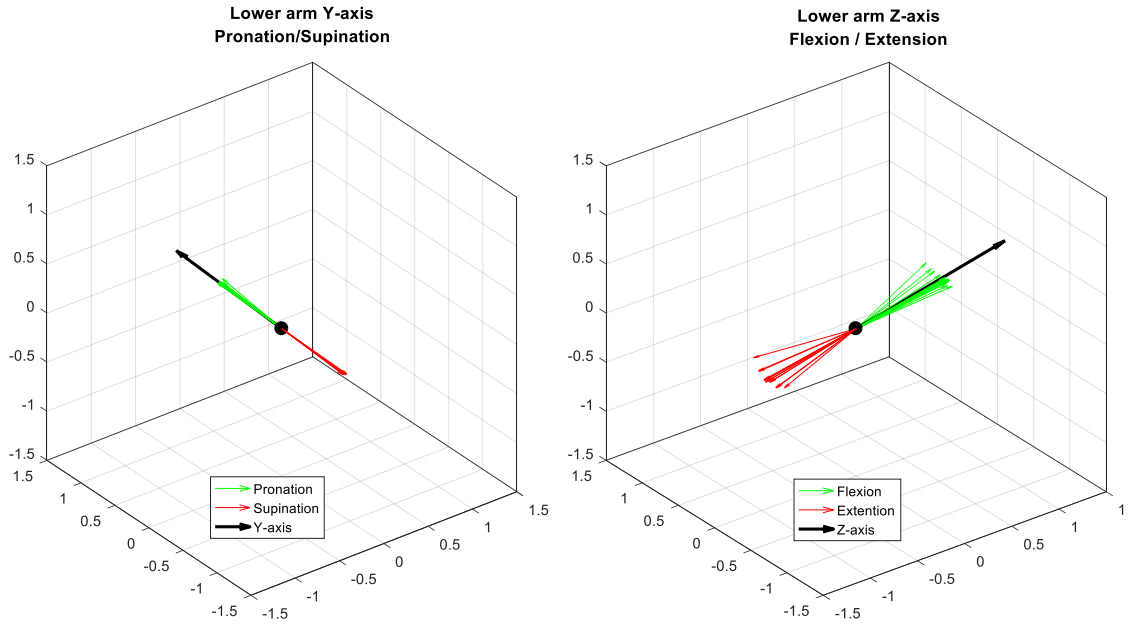

Figure 4-12 in functional calibration a joint is rotating in two directions (one direction is defined with green and the opposite direction with red). The mean of theses directions is used to define the axis.

4.1.2.1.3 Orientation of IMU with respect to the segment

As it was explained in 4.1.2.1.2.1, the $\mathbf{y}_{forearm}$ and $\mathbf{z}_{temp}$ axes are defined. The direction of X-axis can be determined as the direction of the vector perpendicular to the plane of Y and Z-axis. This could be found as the cross product of Y and Z-axis.

$$\mathbf{x}_{forearm} = \mathbf{y}_{forearm} \times \mathbf{z}_{temp} \text{ , where x, y and z are unit vectors.} \quad (25)$$

However, since the Y and Z-axis are found via measurements and anatomy, they would not be exactly orthogonal. The direction of Z-axis is the flexion axis, which defines the elbow joint as a hinge. Particularly, it is difficult to keep the forearm horizontal. Therefore, in order to obtain an orthogonal coordinate system a new Z-axis would be found as the vector perpendicular to the Y and X-axis.

$$\mathbf{z}_{forearm} = \mathbf{x}_{forearm} \times \mathbf{y}_{forearm} \quad (26)$$

A rotation matrix is constructed for each segment to transform the IMU coordinate system (MCS) to the forearm coordinate system defined by functional calibration ($R_{MCS \to FCS}$). This rotation matrix is assumed constant and constructed based on the above functional axes as:

$$R_{MCS \to FCS} = \begin{bmatrix} \mathbf{x}_{forearm} & \mathbf{y}_{forearm} & \mathbf{z}_{forearm} \end{bmatrix} \quad (27)$$

For a better estimation of some joint angles, for example the elbow angle, during elbow flexion/ extension, the Z-axis of lower arm is transformed to the upper arm. That is done since when using ZXY order, the Z is the Z of the proximal axis and since the upper arm is not that much moving and we are interested in the rotation of the lower arm.

It is assumed in this project that IMU sensors are mounted to segments and the skin movements are neglected. According to this assumption, each IMU position and orientation with respect to its regarded segment during measurements remains constant ($R_{MCS \to FCS}$ is assumed to be constant).

The same routine as explained in 4.1.2.1.3 can be used to compute the FCS for all the 7 segments used in this project (hand, forearm, upper arm, thorax, pelvis, thigh and shank). This section gives details of this computation and the selected functional movements. According to the following procedures the coordinate system of segments can be defined using angular velocities recorded by the IMU sensors mounted on the segments regardless the orientation or position of the IMU sensors on the segments.

4.1.2.1.3.1 Thorax

The IMU mounted on thorax between IJ and PX is used to define the coordinate system of thorax is defined based on angular velocities recorded by this IMU during trunk axial rotations and squat.

The Y-axis is pointing upward and is defined using the IMU angular velocities, which points the positive Y-direction when trunk is rotating to the left and negative Y-direction when trunk is rotating to the right.

The Y-axis of thorax may also be defined using the direction of gravity recorded in the linear acceleration data of the IMU. However, such definition would not be probably aligned with the functional axis of the Thorax. But this kind of definition would results in a connection between the segments, which have used gravity as the Y-axis. Besides, it is easier definition of thorax coordinate system.

The Z_{temp}-axis is pointing to the right side and is computed using the IMU angular velocities which represents the positive Z-direction as trunk is flexing forward during the squat motion when the subject goes down and negative Z-direction as trunk is extending backward when the subject is standing up during squat.

The X-axis, pointing forward, is defined as the cross product of Y and Z_{temp}-axis. Subsequently, Z-axis is defined as cross product of X and Y-axis.

$$FCS_{thorax}: \begin{cases} \mathbf{y}_{thorax} = \text{axis}_{trunk\ rotation\ to\ left-trunk\ rotation\ to\ rigth} \quad or \quad \mathbf{y}_{thorax} = \left(\gamma / \left\|\gamma\right\|\right)_{stand} \\ \mathbf{z}_{temp} = \text{axis}_{trunk\ flexion\ to\ down-trunk\ flexion\ to\ up} \\ \mathbf{x}_{thorax} = \left(\mathbf{y}_{thorax} \times \mathbf{z}_{temp}\right) / \left\|\mathbf{y}_{thorax} \times \mathbf{z}_{temp}\right\| \\ \mathbf{z}_{thorax} = \mathbf{x}_{thorax} \times \mathbf{y}_{thorax} \end{cases} \tag{28}$$

4.1.2.1.3.2 Right upper arm

The IMU mounted on the right upper arm distally to the deltoid insertion, where there are less muscle contractions is used. The upper arm coordinate system is defined based on the angular velocities recorded by this IMU during external/internal rotation at 90° elevation and shoulder flexion/extension with the elbow extended.

The Y-axis is defined using the IMU angular velocities, which points the positive Y-direction during shoulder internal rotation and negative Y-direction during shoulder external rotation. The Z_{temp}-axis is pointing to the lateral side and is computed using the IMU angular velocities, which represents the positive Z-direction as the shoulder is flexing (when the arm moves upward) and negative Z-direction as the shoulder is extending (when the arm moves downward).

The X-axis is pointing forward and is defined as the cross product of Y and Z_{temp}-axis. Subsequently, the Z-axis is defined as the cross product of X and Y-axis.

$$FCS_{upperarm}: \begin{cases} \mathbf{y}_{upperarm} = \text{axis}_{shoulder\ internal\ rotation-shoulder\ external\ rotation} \\ \mathbf{z}_{temp} = \text{axis}_{shoulder\ extension-shoulder\ extension} \\ \mathbf{x}_{upperarm} = \mathbf{y}_{upperarm} \times \mathbf{z}_{temp} \,/\, \left\|\mathbf{y}_{upperarm} \times \mathbf{z}_{temp}\right\| \\ \mathbf{z}_{upperarm} = \mathbf{x}_{upperarm} \times \mathbf{y}_{upperarm} \end{cases} \tag{29}$$

4.1.2.1.3.3 Right lower arm

The IMU mounted on the right lower arm proximally to the wrist on the distal part of the radius, where there are less muscle contractions. As it was explained in details in 4.1.2.1.2, the lower arm coordinate system is defined based on angular velocities recorded by this IMU during pronation/supination and flexion/extension of the lower arm.

The Y-axis is pointing from distal to proximal and is defined to the IMU angular velocities, which points to the positive Y-direction during pronation and negative Y-direction during supination of the lower arm. The Z_{temp}-axis is pointing from the medial side to the lateral side and is computed using the IMU angular velocities, which represents the positive Z-direction as the elbow is flexing (when arm moves upside) and the negative Z-direction as elbow is extending (when arm moves downside). The X-axis is defined as the cross product of Y and Z_{temp}-axis. Subsequently, the Z-axis is defined as the cross product of X and Y-axis.

$$FCS_{lowerarm}: \begin{cases} \mathbf{y}_{lowerarm} = \text{axis}_{pronation-supination} \\ \mathbf{z}_{temp} = \text{axis}_{elbow\ flexion-elbow\ extension} \\ \mathbf{x}_{lowerarm} = \mathbf{y}_{lowerarm} \times \mathbf{z}_{temp} \,/\, \left\|\mathbf{y}_{lowerarm} \times \mathbf{z}_{temp}\right\| \\ \mathbf{z}_{lowerarm} = \mathbf{x}_{lowerarm} \times \mathbf{y}_{lowerarm} \end{cases} \tag{30}$$

4.1.2.1.3.4 Right hand

The IMU mounted on the dorsal part of the right hand is used to define the coordinate system of the right hand based on the angular velocities recorded by this IMU during radial/ulnar deviation and flexion/extension of the right hand.

Since the wrist has no axial rotation, for the hand we used a different order in the axis computation than the other segments. The Z-axis, pointing from medial to lateral, is defined using

the IMU angular velocities, which points the positive Z-direction during flexion and negative Z-direction during extension of the right hand. The X_{temp}-axis, pointing forward, is computed using the IMU angular velocities, which represents the positive X-direction during ulnar deviation and the negative X-direction during radial deviation. The Y-axis is defined as the cross product of the Z and X_{temp}-axis. Subsequently, the X-axis is defined as the cross product of the Y and Z-axis.

$$FCS_{hand}: \begin{cases} \mathbf{z}_{hand} = \text{axis}_{\textit{hand flexion}-\textit{hand extension}} \\ \mathbf{x}_{temp} = \text{axis}_{\textit{ulnar deviation}-\textit{radial deviation}} \\ \mathbf{y}_{hand} = \mathbf{z}_{hand} \times \mathbf{x}_{temp} \,/\, \left\| \mathbf{z}_{hand} \times \mathbf{x}_{temp} \right\| \\ \mathbf{x}_{hand} = \mathbf{y}_{hand} \times \mathbf{z}_{hand} \end{cases} \tag{31}$$

4.1.2.1.3.5 Pelvis

The IMU mounted on the thorax between RPSIS and LPSIS (which would be almost on MPSIS) is used to define the coordinate system of the pelvis based on angular velocities and linear accelerations recorded by this IMU during trunk lateral rotations and squat.

The Y-axis is defined using the IMU acceleration, which points the positive Y-direction when standing (i.e. gravity).

The Z_{temp}-axis is computed using the IMU angular velocities, which represents the positive Z-direction during squat motion when the subject goes down and negative Z-direction when the subject is standing up during squat. The X-axis is defined as the cross product of Y and Z_{temp}-axis. Subsequently, the Z-axis is defined as cross product of X and Y-axis.

$$FCS_{pelvis}: \begin{cases} \mathbf{y}_{pelvis} = \left(\gamma / \left\| \gamma \right\| \right)_{stand} \\ \mathbf{z}_{temp} = \text{axis}_{\textit{trunk flexion to down (sitting down)-trunk flexion to up (standing up)}} \\ \mathbf{x}_{pelvis} = \mathbf{y}_{temp} \times \mathbf{z}_{pelvis} \,/\, \left\| \mathbf{y}_{temp} \times \mathbf{z}_{pelvis} \right\| \\ \mathbf{y}_{pelvis} = \mathbf{z}_{pelvis} \times \mathbf{x}_{pelvis} \end{cases} \tag{32}$$

4.1.2.1.3.6 Left thigh

An IMU is mounted on the distal and lateral part of the thigh on the tendon part of the iliotibial band. The thigh coordinate system is defined based on angular velocities recorded by this IMU during hip internal external rotation and hip flexion/extension with extended knee (heel does not touch the ground).

The Y-axis is pointing from distal to proximal and is defined using the IMU angular velocities, which points to the positive Y-direction during external rotation of the hip and negative Y-direction during the hip internal rotation. The Z_{temp}-axis is pointing from lateral to medial and is computed using the IMU angular velocities, which represents the positive Z-direction when the hip is flexing and negative Z-direction when the hip is extending. The X-axis is pointing forward and is defined as the cross product of Y and Z_{temp}-axis. Subsequently, Z-axis is defined as cross product of X and Y-axis.

$$FCS_{thigh}: \begin{cases} \mathbf{y}_{thigh} = \text{axis}_{\textit{external rotation-internal rotation}} \\ \mathbf{z}_{temp} = \text{axis}_{\textit{hip flexion}-\textit{hip extension}} \\ \mathbf{x}_{thigh} = \mathbf{y}_{thigh} \times \mathbf{z}_{temp} \,/\, \left\| \mathbf{y}_{thigh} \times \mathbf{z}_{temp} \right\| \\ \mathbf{z}_{thigh} = \mathbf{x}_{thigh} \times \mathbf{y}_{thigh} \end{cases} \tag{33}$$

4.1.2.1.3.7 Left shank

An IMU is mounted on the medial and proximal part of the tibia. The shank coordinate system is defined based on angular velocities recorded by this IMU during hip internal/external rotation when the subject is standing with extended knee (the same motion as was used for thigh) and during knee flexion/extension when the subject is sitting.

The Y-axis is defined using the IMU angular velocities, which points to the positive Y-direction during hip external rotation and negative Y-direction during the hip internal rotation. The Z_{temp}-axis is computed using the IMU angular velocities, which represents the positive Z-direction as the knee is flexing and negative Z-direction when the knee is extending. The X-axis is defined as the cross product of Y and Z_{temp}-axis. Subsequently, the Z-axis is defined as the cross product of the X and Y-axis.

$$FCS_{shank}: \begin{cases} \mathbf{y}_{shank} = \text{axis}_{lateral\ rotation\ to\ left-lateral\ rotation\ to\ rigth} \\ \mathbf{z}_{temp} = \text{axis}_{flexion-extension} \\ \mathbf{x}_{shank} = \mathbf{y}_{shank} \times \mathbf{z}_{temp} \\ \mathbf{z}_{shank} = \mathbf{x}_{shank} \times \mathbf{y}_{shank} \end{cases} \quad (34)$$

4.1.2.2 Segment angular velocity and acceleration

One of the important goals of this project was to compute accurately (against marker-based as reference) the angular velocity of segments with an IMU-based method.

In the previous section, the constant transformation between the IMU and the segment mounted on it was estimated. Having this transformation ($R_{MCS\rightarrow FCS}$), the angular velocities recorded by each IMU (ω_{MCS}) can be transformed into its segment's coordinate system (ω_{FCS}). The angular acceleration can be computed then by one step differentiation of the angular velocity.

$$\begin{aligned} \omega_{FCS} &= R_{FCS\rightarrow MCS} * \omega_{MCS} = R^{-1}_{MCS\rightarrow FCS} * \omega_{MCS} \\ \alpha_{FCS} &= \dot{\omega}_{FCS} \end{aligned} \quad (35)$$

4.1.2.3 Joints rotation

The orientation of IMU with respect to its initial orientation ($q_{MCS^0\rightarrow MCS^t}$) can be estimated using strap-down integration as it was explained in chapter 2. The Consensys Software is the embodied software of the Shimmer IMU sensors which computes quaternion based on Madgwick and Mahony algorithm (Madgwick, Harrison et al. 2011). This quaternion can be transformed to their equivalent rotation matrix ($R_{MCS^0\rightarrow MCS^t}$).

From the functional calibrations, we computed in 4.1.2.1 the transformations from the coordinate system of each IMU to the segment mounted on it ($R_{MCS\rightarrow FCS}$). As it was mentioned in **Error! Reference source not found.** in order to relate two IMU's data, the initial orientation of the IMU sensors with respect to each other needs to be known. Since there is no global reference frame definition in IMU data, we have to define a connection between each proximal and distal segment coordinates to compute the joint angle. For this purpose, it is sufficient to know this relation one frame, like the initial condition. That is to be determining by a known configuration in which orientations of the segments with respect to each other is known. A static known anatomical position (like standing) with assumed joint angles can be used to define this relation. In order to make the IMU and marker joint angles comparable we can also take the initial angle from one system and put it to the other system. We did set the initial orientation of the IMU with the orientation computed at the same time from the markers (Figure 4-13).

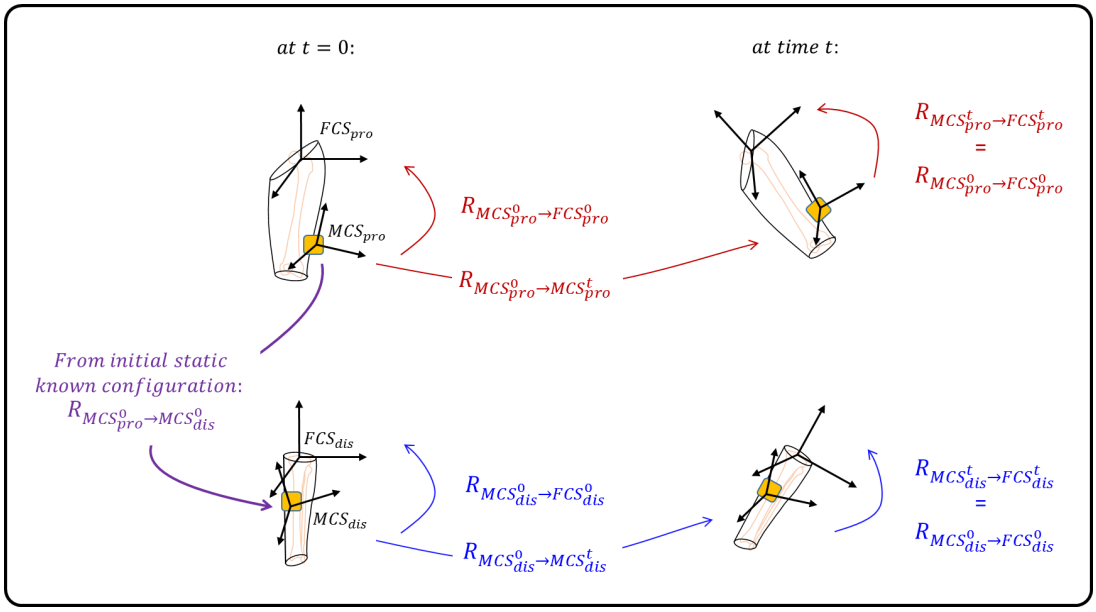

Figure 4-13 Schematic view of the known data of two adjacent segments

In order to do this, first of all, the quaternions of each IMU has been initialized to start from the zero position by multiplication of it by its initial conjugate taken at the starts of the motion.

$$R_{starting\ from\ zero} = R_{1:end} \otimes R_1^{-1} \tag{36}$$

Subsequent problem is that the marker-based the angle representations were done in the LCS of the segment, while the IMU-based data are in FCS of the segment. Therefore, it is needed to get the initial angle in a similar coordinate system from marker-based data. We computed the functional axis using the same routine as it was explained for the IMU-based data in section 4.1.2.1. We used the segments angular velocities computed by marker-based data instead of the angular velocity measured by gyroscope.

Having these all, we can define the joint rotation from the proximal to the distal segment by:

$$R_{FCS^t_{pro}\rightarrow FCS^t_{dis}} = R^{-1}_{MCS^t_{pro}\rightarrow FCS^t_{pro}} . R^{-1}_{MCS^0_{pro}\rightarrow MCS^t_{pro}} . R_{MCS^0_{pro}\rightarrow MCS^0_{dis}} . R_{MCS^0_{dis}\rightarrow MCS^t_{dis}} . R_{MCS^t_{dis}\rightarrow FCS^t_{dis}} \tag{37}$$

The initial orientations of the IMU sensors with respect to each other can be rewrite to be defined as a function of orientations of segments with respect to each other:

$$R_{MCS^0_{pro}\rightarrow MCS^0_{dis}} = R_{MCS^0_{pro}\rightarrow FCS^0_{dis}} . R_{FCS^0_{pro}\rightarrow FCS^0_{dis}} . R^{-1}_{MCS^0_{pro}\rightarrow FCS^0_{pro}} \tag{38}$$

And the orientation of IMU sensors with respect to the segments are assumed to remain constant in time, thus:

$$\begin{aligned} R_{MCS^0_{pro}\rightarrow FCS^0_{pro}} &= R_{MCS^t_{pro}\rightarrow FCS^t_{pro}} \\ R_{MCS^0_{dis}\rightarrow FCS^0_{dis}} &= R_{MCS^t_{dis}\rightarrow FCS^t_{dis}} \end{aligned} \tag{39}$$

4.1.2.4 Joints angular velocity and acceleration

The angular velocity and accelerations of joints are computed with the same routine as it was explained in 4.1.1.2 for the marker-based kinematic computations.

A non-orthogonal projection (Desroches, Dumas et al. 2010) of the joint angular velocity is used to compute the angular velocity on the Joint Coordinate Systems (JCS, as defined in (Wu, Van Der Helm et al. 2005).

Table 4-1- JCS of the shoulder, elbow and wrist

Shoulder	Elbow	Wrist
$\begin{cases} \mathbf{e}_1 = \mathbf{y}_{ics}^{th} \\ \mathbf{e}_3 = \mathbf{y}_{ics}^{ua} \\ \mathbf{e}_2 = \mathbf{e}_3 \times \mathbf{e}_1 \end{cases}$	$\begin{cases} \mathbf{e}_1 = \mathbf{z}_{ics}^{ua} \\ \mathbf{e}_3 = \mathbf{y}_{ics}^{la} \\ \mathbf{e}_2 = \mathbf{e}_3 \times \mathbf{e}_1 \end{cases}$	$\begin{cases} \mathbf{e}_1 = \mathbf{z}_{ics}^{la} \\ \mathbf{e}_3 = \mathbf{y}_{ics}^{h} \\ \mathbf{e}_2 = \mathbf{e}_3 \times \mathbf{e}_1 \end{cases}$

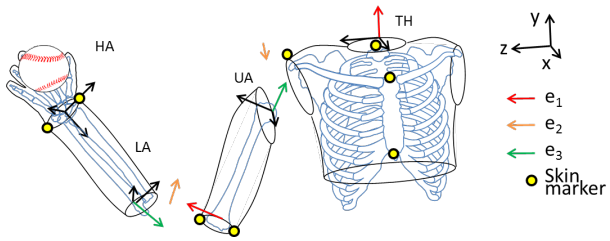

Figure 4-14 Representation of the local coordinate systems and joint coordinates systems of the linked chain model. The joint coordinate systems are used to get an anatomical interpretation of the mechanical parameters computed by the models.

This step is not needed for power computation, and it is only used for analysis of joint's angular velocities and accelerations.

4.1.2.5 Overview

Using functional calibration, the transformation between the IMU data (measured in MCS) to the coordinate system of segment is estimated by $R_{MCS \rightarrow FCS}$. This relative orientation of the FCS with respect to the MCS is assumed to be constant in time due to the hypothesis of rigid segment. Having this transformation matrix, the angular velocity recorded by the IMU in the MCS can be transformed to the FCS, which would be the angular velocity of the segment (ω_s) and by one step differentiation the angular accelerations (α_s). Further, the orientation of the IMU in time can be computed using a strap-down integration algorithm ($R_{MCS^0 \rightarrow MCS^t}$). Using these filled in the equation 37, the joint angle can be estimated. Figure 4-15 shows these routine steps as explained in detail in section 4.1.2 to compute the joint angles from the IMU's recorded data.

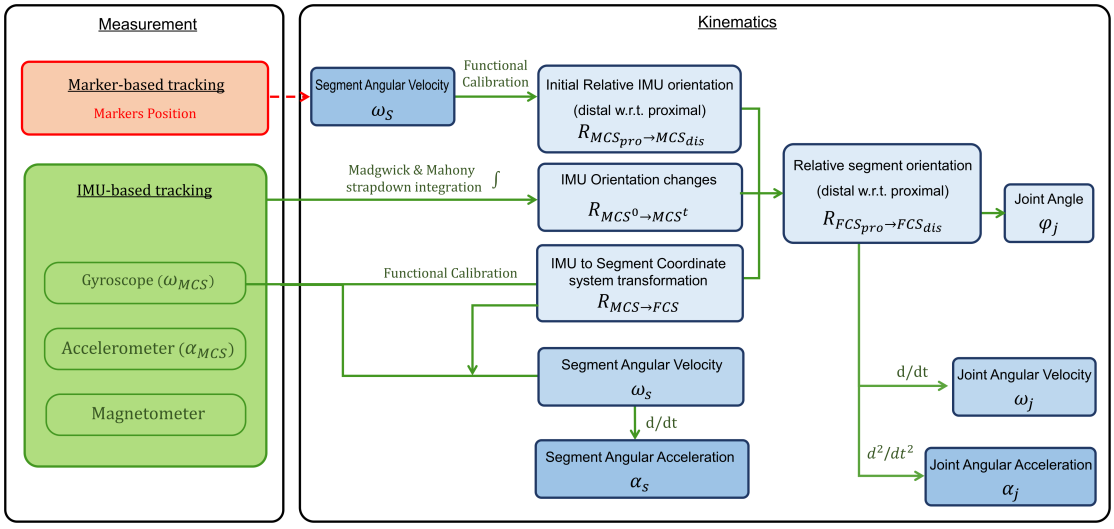

Figure 4-15 Joint rotation calculation routine IMU-based data

Note that for this study, the relative IMU sensors orientation is taken from an initial frame in marker-based measurement (---> in Figure 4-15, comes from angular velocity (ω_s) containing one step differentiation). In discussion another method for future studies is suggested.

4.2 Anthropometric model & Power flow

In this section, the Anthropometric model and a method to compute kinetic energy generation in body segments and power flow is explained. The necessary velocities of joints and segments for this computation were calculated as it was explained in section 4.1. Furthermore a scalable anthropometric model from literature is used to set up the mass and inertias properties. For the scaling process, the segments length is needed which is easy to calculate from the joint positions of the Optitrack data. The segments length computation from the IMU data is not trivial. A method to compute the segments length from the IMU data is described.

4.2.1 Full body anthropometric model

We used the scalable anthropometric model established by (Wu and Cavanagh 1995, Wu, Siegler et al. 2002, Wu, Van Der Helm et al. 2005), based on the positions and inertia data from (Dumas, Cheze et al. 2007) which is in its turn an adjustment of the measurements of McConville et al. (McConville, Clauser et al. 1980). Appendix 2 describes in detail the antropometric model and the scaling of the mass and inertia parameters of the segments.

The kinematic constraints keep the motion of the independent defined positions in the local coordinates of the segments together by bonding the joints together. Having 14 joints in the model requires 14 kinematic constrains to keep the 15 segments together. The kinematic constraints could be defined by equality of two definitions of the same joint positions in two adjacent segments. For example, the shoulder joint in global coordinate system may be defined according to the equation 9, both from the thorax and from the upper arm segments in the GCS:

$$\begin{bmatrix} 0 \\ SJC_{GCS} \end{bmatrix} = \begin{bmatrix} 0 \\ O_{thorax} \end{bmatrix} + q_{thorax} \otimes \begin{bmatrix} 0 \\ SJC_{thorax} \end{bmatrix} \otimes \overline{q}_{thorax}$$
$$\begin{bmatrix} 0 \\ SJC_{GCS} \end{bmatrix} = \begin{bmatrix} 0 \\ O_{upperarm} \end{bmatrix} + q_{upperarm} \otimes \begin{bmatrix} 0 \\ SJC_{upperarm} \end{bmatrix} \otimes \overline{q}_{upperarm} \quad (40)$$

Whereas, SJC_{GCS} is the global position of the shoulder joint centre, CJC_{GCS} is the global position of origin of the thorax coordinate system, SJC_{thorax} is the position of shoulder joint centre with respect to the thorax coordinate system. We assume that the SJC_{GCS} is fixed. q_{thorax} and $q_{upperarm}$ are respectively the quaternions of the thorax and the upper arm and $\overline{q}_{thorax}$ and $\overline{q}_{upperarm}$ are respectively the conjugate of the quaternions of the thorax and the upper arm. The left hand side of the equations 37 are identical. Accordingly, the kinematic constraint, which keeps the upper arm attached to the thorax in the shoulder joint, is defined by:

$$\left(\begin{bmatrix} 0 \\ O_{thorax} \end{bmatrix} + q_{thorax} \otimes \begin{bmatrix} 0 \\ SJC_{thorax} \end{bmatrix} \otimes \overline{q}_{thorax} \right) - \left(\begin{bmatrix} 0 \\ O_{upperarm} \end{bmatrix} + q_{upperarm} \otimes \begin{bmatrix} 0 \\ SJC_{upperarm} \end{bmatrix} \otimes \overline{q}_{upperarm} \right) = 0 \quad (41)$$

One extra constraint is defined to introduce the initial position of the human body. This has been defined by the equality of the measured position of the Incisura Jugularis ($IJ_{measured}$), and the global position of Incisura Jugularis (IJ_{GCS}). IJ is leading the motion.

$$IJ_{GCS} - IJ_{measured} = 0 \quad (42)$$

Note that, this was possible due to the use of skin markers measurements and should be modified for a method using only IMU sensors. As it was explaind extensively in chapter 3, the IMU sensors do not measure translations and position of segments. Thus some adjustments needs to be done in the IMU based methods to measure the position. This is probably a limitation to track with IMU in future project. In this project since we used an initial frame from marker-based method, we did not faced this problem.

The transformation is defined as the sum of translation and rotation (Bajd, Mihelj et al. 2010). Where the translation (O_{GCS}) shifts the origin of coordinate system from the global frame to the local frame. It is the position of the origin of segment coordinate system (the joint centre) in the global coordinate system.

$$\underbrace{P_{GCS}}_{Transformation} = \underbrace{O_{GCS}}_{Translation} + \underbrace{R_{xyz}.P_{LCS}}_{Rotation} \tag{43}$$

Subsequently from the equality of the equation 9 and 19, we have:

$$\begin{bmatrix} 0 \\ R_{xyz}.P_{LCS} \end{bmatrix} = q_{LCS} \otimes \begin{bmatrix} 0 \\ P_{LCS} \end{bmatrix} \otimes \overline{q}_{LCS} \tag{44}$$

The model is tested with pitching data measured with skin markers method. The quaternion's of segments has been calculated from the skin markers tracking measurements. The model was able to represent pitching.

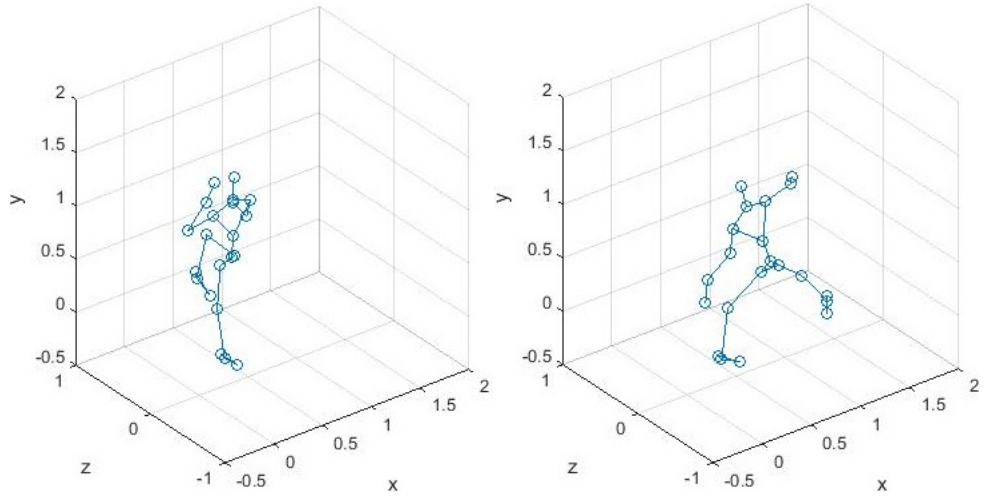

Figure 4-16 Matlab implemented model with quaternions during pitching. Quaternion data from real player pitching is used.

This model is capable to work for both measurement data from IMU's and Optitrack markers. The model input can be either the IMU's acceleration, velocity and orientation data or the positions data of the OptiTrack system. Using this model the computed data can be verified by comparing the 3D illustration of the two methods.

4.2.1.1 Mass and Inertial Parameters

The mass properties and joint centres are defined using regression equations based on the mass of the pitcher and the dimension of his segments (Dumas et al. 2007). As an example, the mass of the thorax will represent 26.8% of the pitcher's mass and the position of the centre of mass in the thorax will be defined as percentage of the length between the cervical joint and the thoracic joint.

Mass and Inertial Parameters are computed based on regression from Dumas et al 2007:

The inertia matrix of Segment centre of mass (CoM) and in its LCS are computed following Dumas et al. (2007):

$$I_{ij} = (r_{ij}.l_s)^2.m_s \quad \text{with:} \begin{cases} r_{ij} \text{ scaling vector for the body segment inertial parameters from Dumas et al. 2007} \\ l_s \text{ the lenght of the segment} \\ \text{m}_s \text{ the mass of the segment} \end{cases} \tag{45}$$

Inertia matrix at CoM in the global coordinate system is computed as follow:

$$I^{s}_{G_{GCS}} = R_{GCS\rightarrow LCS}.I^{s}_{G_{LCS}}.R_{LCS\rightarrow GCS} \tag{46}$$

In Dumas et al. the element of the matrix of inertia for each body segment is computed as:

$$I_{ij} = (r_{ij}.l_s)^2.m_s \quad \text{thus:} \quad r_{ij} = \left(\frac{I_{ij}}{m_s}\right)^{1/2}.\frac{1}{l_s} \tag{47}$$

The Position of centre of masses (CoM) in the global coordinate system is computed as:

$$\begin{bmatrix} 0 \\ G_{GCS} \end{bmatrix} = \begin{bmatrix} 0 \\ O_s \end{bmatrix} + q \otimes \begin{bmatrix} 0 \\ G_{LCS} \end{bmatrix} \otimes \overline{q} \tag{48}$$

The velocity of CoMs in the global coordinate system is computed as:

$$\begin{bmatrix} 0 \\ v_{G_{GCS}} \end{bmatrix} = \begin{bmatrix} 0 \\ \dot{O}_s \end{bmatrix} + \dot{q} \otimes \begin{bmatrix} 0 \\ G_{LCS} \end{bmatrix} \otimes \overline{q} + q \otimes \begin{bmatrix} 0 \\ G_{LCS} \end{bmatrix} \otimes \dot{\overline{q}} \tag{49}$$

The accelerations of CoMs in the global coordinate system is computed as:

$$\begin{bmatrix} 0 \\ \gamma_{G_{GCS}} \end{bmatrix} = \begin{bmatrix} 0 \\ \ddot{O}_s \end{bmatrix} + \ddot{q} \otimes \begin{bmatrix} 0 \\ G_{LCS} \end{bmatrix} \otimes \overline{q} + q \otimes \begin{bmatrix} 0 \\ G_{LCS} \end{bmatrix} \otimes \ddot{\overline{q}} + 2\dot{q} \otimes \begin{bmatrix} 0 \\ G_{LCS} \end{bmatrix} \otimes \dot{\overline{q}} \tag{50}$$

4.2.2 Inverse dynamics

The kinematics is estimated for the IMU-based method as well as for the Optitrack-based method; segment's coordinate system from functional calibration and joint centres, segment lengths, joint angles and velocities. The SCS, joint centres, segment length are used in the anthropometric human body model for estimating the segment masses, inertias and centre of mass position in SCS.

Once the kinematic and inertial properties are defined and the external forces are known, and the inverse dynamics method is used on limbs to determine the joint actions. In this study, due to the lack of measurement of ground reaction force (external force), only the upper arm power flow is estimated. The power flow in the other joint cannot be estimated since we did not measure the reaction force of the ground (Figure 4-17).

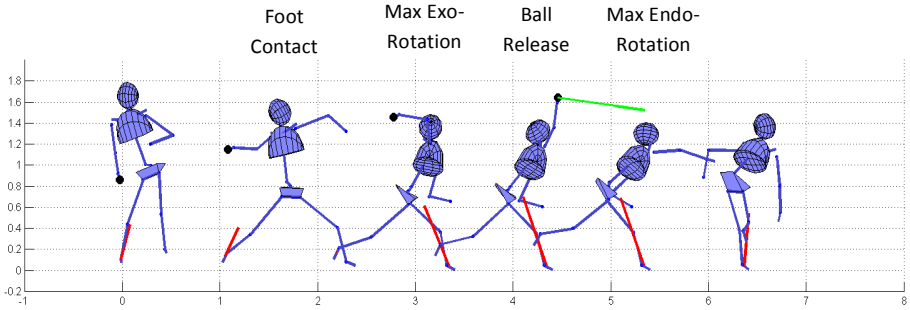

Figure 4-17 the main phases of pitching represented with the linked chain model. The red arrows represent the ground reaction forces, the green arrow represent the ball velocity at the time of ball release.

Then an inverse dynamic model is used only for the arm's segments. The inverse dynamics goes from distal to proximal segment in a recursive way from hand through lower and upper arm to the shoulder. Note that we did not have the ball and glove in our study thereby for the hand segment the external forces are equal to zero. So for the dynamic of hand segment can be estimated from which the forces and moments at wrist can be estimated. Afterward the dynamic of lower arm and from that the forces and moments at elbow and then the dynamics of upper arm and moments and forces at shoulder can be estimated. For two segment i and i-1, where i is the proximal segment and i-1 the distal segment (in Figure 4-18 is indicated each the number for each segment).

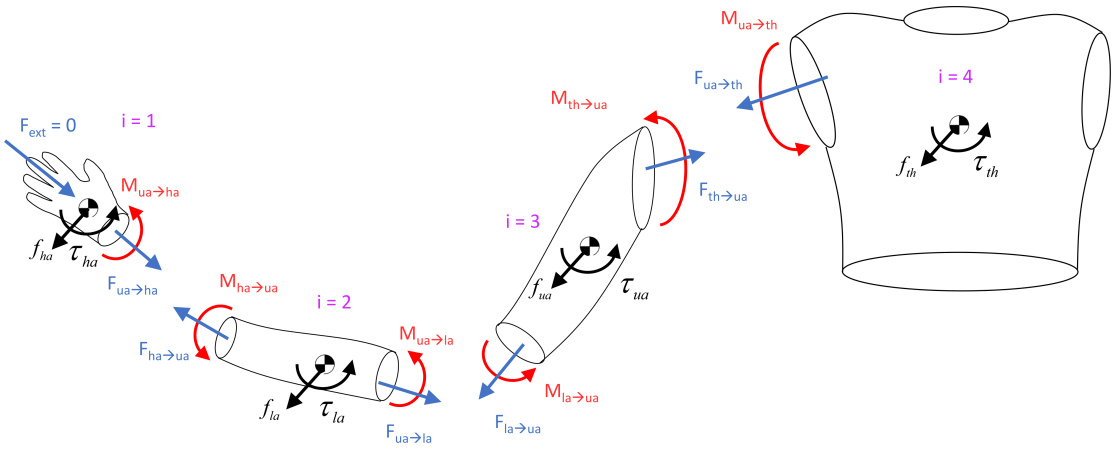

Figure 4-18 Inverse dynamic model of Arm. In this figure, *M* is the moment, *F* is the force, Γ is the derivative of linear momentum, δ is the derivative of angular momentum, *th* is the thorax, *ua* is the upper arm, *la* is the lower arm, ha is the hand. Where the $F_{ua\to th}$ is the force that upper arm apply on the thorax and F_{ext} is the external force.

Since the mass of a segment being assumed to be rigid is constant, the translational motion of the centre of mass can be defined by:

$$\Gamma_{GCS} = m.\gamma_{G_{GCS}}, \text{ where the } \gamma_{G_{GCS}} \text{ is the linear acceleration of the centre of mass} \quad (51)$$

For the IMU method the linear velocity of segment (at CoM) can be computed by integration of the linear acceleration (at CoM). Here it is also important to pay attention to that in computation of IMU's orientation we used a very small beta ($\beta = 0.0001$), as it was mentioned in 3.2.2. This means less trust the magnetometer and accelerometer and more trust gyroscope. The reason to this was that the existence of gravity in the recorded data of IMU. So actually we ignored the acceleration data and estimate the orientation of IMU. Now using this orientation ($R_{MCS^0\to MCS^t}$), the gravity can be removed from the acceleration data ($\gamma_{corrected\ for\ gravity}$).

$$\gamma_{corrected\ for\ gravity} = \gamma_{MCS} - \left(R_{MCS^0\to MCS^t}.g_{MCS}\right) \quad (52)$$

The g_{MCS} is the gravity direction in coordinate system of the IMU, which is simply to be defined at t_0 (when the subject is standing upright and not moving), using the recorded acceleration. Knowing the fact that the IMU is not moving so the only acceleration presented in the data recorded by the IMU is the gravity and the direction of gravity with respect to the coordinate system of IMU is simply to be defining by the recorded acceleration.

$$g_{MCS} = 9.81\left(\gamma/|\gamma|\right) \quad (53)$$

Note, the γ_{MCS} has been taken as the mean of a short run measurement (Figure 4-19).

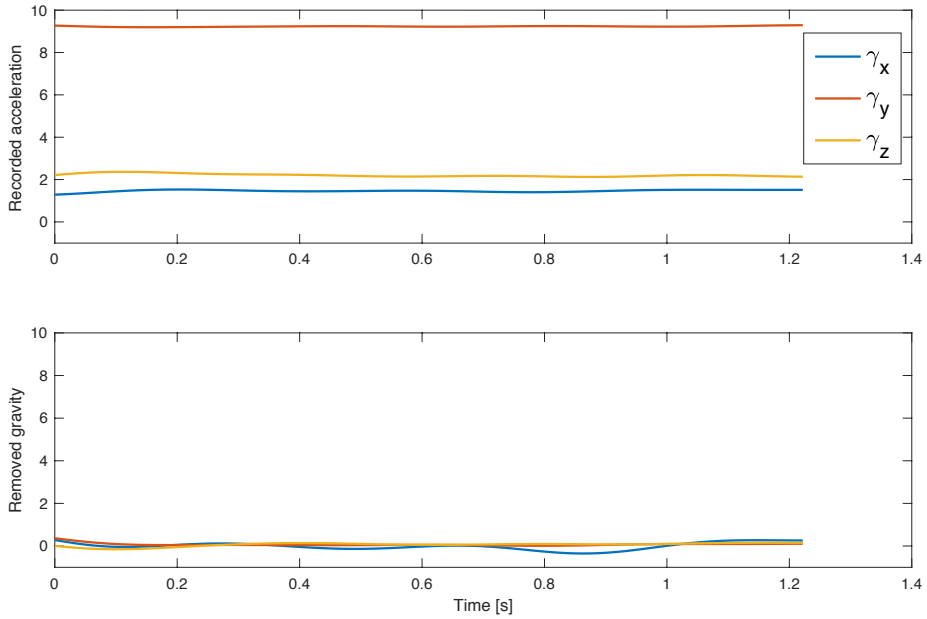

Figure 4-19 Gravity removing from accelerations recorded data in IMU. This figure if filtered acceleration of thorax in standing condition.

The linear acceleration recorded by the IMU needs to be transformed to the centre of mass of the segments. This is done by:

$$\gamma_{GCS} = \left(R_{MCS\to FCS}\cdot\gamma_{IMU}\right) + \left(\left(\underbrace{r_{proximal\,joint\,to\,IMU} - r_{proximal\,joint\,to\,CoM}}_{r_{CoM\,to\,IMU}}\right)\times\dot{\omega}_{FCS}\right) \tag{54}$$

Subsequently the linear velocities (v_i) of each segment i, is to be computed by one step integration. However this step is known to be inaccurate according to many previous studies, since the computation of velocity via the numerical integration would results in a drift in it (Deblonde 2011). If the drift is linear, we can compensate it.

Similarly, the equations describing angular motion can be derived considering the rotational motion of each segment about a joint centre:

$$\delta_{GCS} = I_{g_{GCS}}.\gamma_{GCS} + \omega_{GCS}\times\left(I_{g_{GCS}}.\omega_{GCS}\right) + \left(R_{GCS\to LCS}.r^{G}_{LCS}\right)\times\Gamma_{GCS} \tag{55}$$

Where the r^{G}_{LCS} is the lever arm

The segments dynamic are defined by Newton-Euler equations:

1- The Newton equation for each segment i (as defined in Figure 4-18) is computed as:

$$\delta^{i}_{GCS} = F_{i+1\to i} + F_{i-1\to i} + m_i g \Rightarrow F_{i+1\to i} = \delta^{i}_{GCS} - F_{i-1\to i} - m_i g = \delta^{i}_{GCS} + F_{i\to i-1} - m_i g \tag{56}$$

If i is the first segment (most distal which is hand) then $F_{i-1\to i}$ is the force applied by the environment on the distal segment, thus $F_{i\to i-1}$ is the force applied by the segment on the environment.

2- The Euler equation for each segment i (as defined in Figure 4-18) is computed as:

$$\delta^i_{GCS} = M^{o^i}_{i+1\to i} + M^{o^i}_{i-1\to i} + M_{Wi} \;\Rightarrow\; M^{o^i}_{i+1\to i} = \delta^i_{GCS} + M^{o^i}_{i-1\to i} - M_{Wi} \tag{57}$$

$$\text{whereas:}\begin{cases} M^{o^i}_{i-1\to i} = M^{o^{i-1}}_{i\to i-1} + \left(r^{o^{i-1}}_{GCS} - r^{o^i}_{GCS}\right)\times F_{i\to i-1} \\ M_{Wi} = \left(R_{GCS\to LCS}\,.\,r^{G^i}_{LCS^i}\right)\times m_i g \end{cases}$$

4.2.3 Segment power

For estimating the segment power, the linear and angular velocity of the centre of mass of each segment i are used align with the derivatives of the linear and angular momentum as follows:

$$\begin{cases} \text{Translational power:} & P^l_i = F_i\,.\,v_i \\ \text{Angular power:} & P^\omega_i = M_i\,.\,\omega_i \end{cases} \text{, the total power is: } P = P^l_i + P^\omega_i \tag{58}$$

4.2.4 Joint power

For estimating the joint power, the joint angular velocity is computed as:

$$\omega_{joint} = \omega_{dis\to pro} = \omega_{dis} - \omega_{pro} \tag{59}$$

Using this definition, the joints power is computed as follow:

$$P^\omega_{joint} = M_{joint}\,.\,\omega_{joint} \tag{60}$$

Chapter 5

Results & Discussion

In this chapter, in order to validate the IMU-based functional calibration method introduced in this study (the 50% of the maximum angular velocity ($50\%\ \omega_{max}$) explained in 4.1.2.1.2.2), we did compare the results with the optimization method of Seel et al. explained in 4.1.2.1.2.1. The similarity of the results of these two functional calibration methods may confirm the correctness of the method.

The kinematic and kinetic results of Marker-based and IMU-based methods are presented. The error of the IMU-based measurement against the marker-based reference is quantified. The sources of these dissimilarities are identified at different levels of segments and joints rotation angle, angular velocities and accelerations.

5.1 Rotation angle

5.1.1 Segment angle

The segment rotation is computed based on the two functional calibration methods (50% ω_{max} and the Optimization) applied on both Optitrack and IMU data. Figure 5-1 shows, as an example, the computed lower and upper arm rotations represented by Euler angles (ZXY order) during elbow flexion/extension. As you can see the upper arm is almost not moving and the lower arm is flexing and extending.

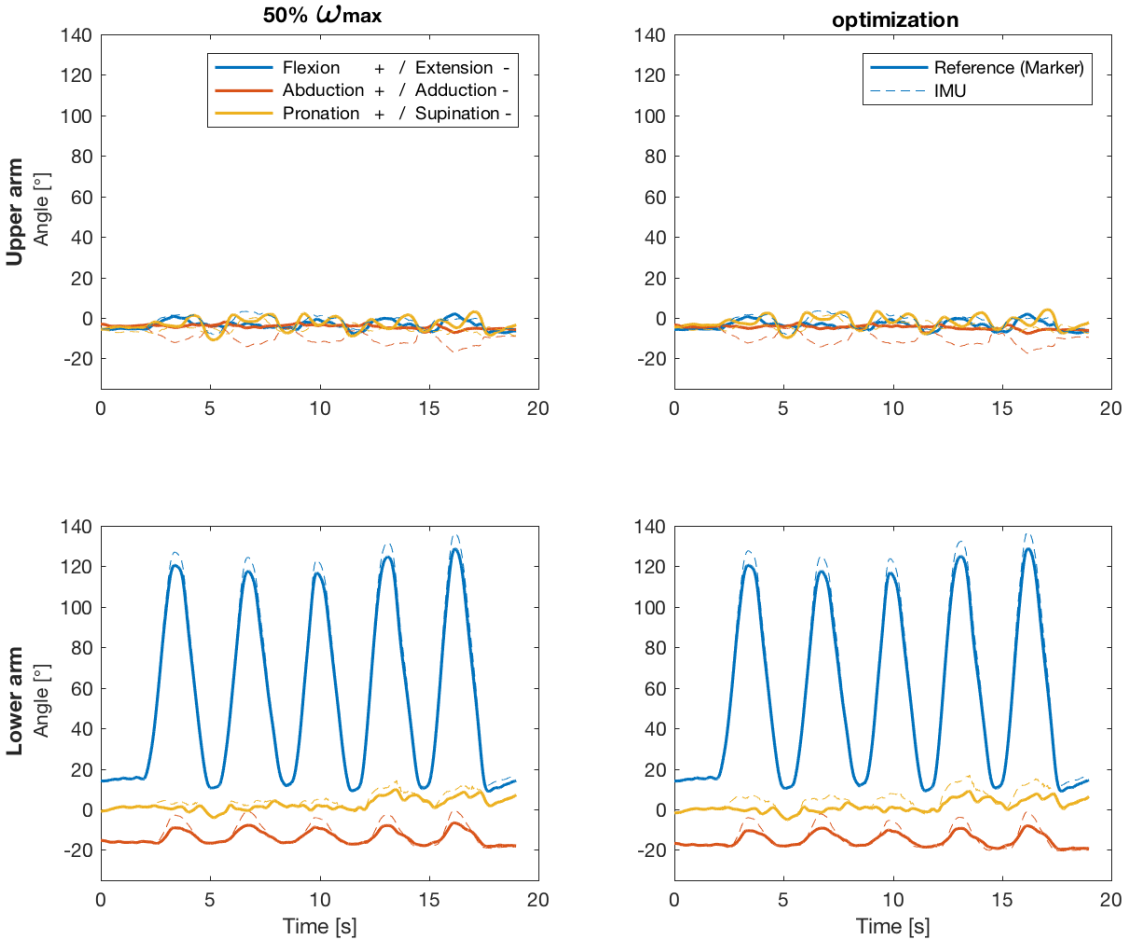

Figure 5-1 Lower and upper arm rotation is represented by Euler angles (with ZXY order) during elbow flexion and extension. The computation is done with both 50%ω_{max} and Optimization methods.

In Figure 5-1, the patterns of the angles are similar between both methods with a similar range difference (a peak difference of around 10°). Only the abduction/adduction angle of lower arm is not similar in both methods.

5.1.2 Joint angle

Similarly the joint rotation is computed based on the two (50% ω_{max} and the Optimization) methods applied on both Optitrack and IMU data. As it was explained in section 4.1, we use a ZXY Euler angle rotation sequence which means Z of the proximal segment, Y of the distal segment and X is the cross Product of these two. For the shoulder a YXY Euler angle rotation sequence is used which means Y of the proximal segment, Y of the distal segment and X is the cross Product of these two (Wu, Van Der Helm et al. 2005).

Figure 5-2 shows, the elbow joint rotation represented by Euler angles (with ZXY order). As you can see Figure 5-1 and Figure 5-2 show similar pattern for flexion/extension angle. This

similarity was expected since the proximal segment is not moving much and the joint angle would only present the motion of the distal segment (lower arm). As it was mentioned in 4.1.2.1.3, to make the angle estimation is this motion more accurate, the Z-axis of distal segment is transformed to the proximal segment.

The $50\%\ \omega_{max}$ method joint flexion/extension angle estimation patterns are similar between all angles with a peak difference of less than 10°. But, the abduction/adduction and pronation/supination are significantly different. Still the axis angles are very similar. The computation is done based on both $50\%\ \omega_{max}$ and Optimization methods. The $50\%\ \omega_{max}$ method during elbow flexion showed smaller amplitude of the adduction/abduction and pronation angles and similar estimation of flexion angle. The minimization of the adduction/abduction shows that the estimation of the flexion axis was more accurate with the $50\%\ \omega_{max}$ method. This method reduced the cross talk when compared to the Optimization method (Figure 5-2).

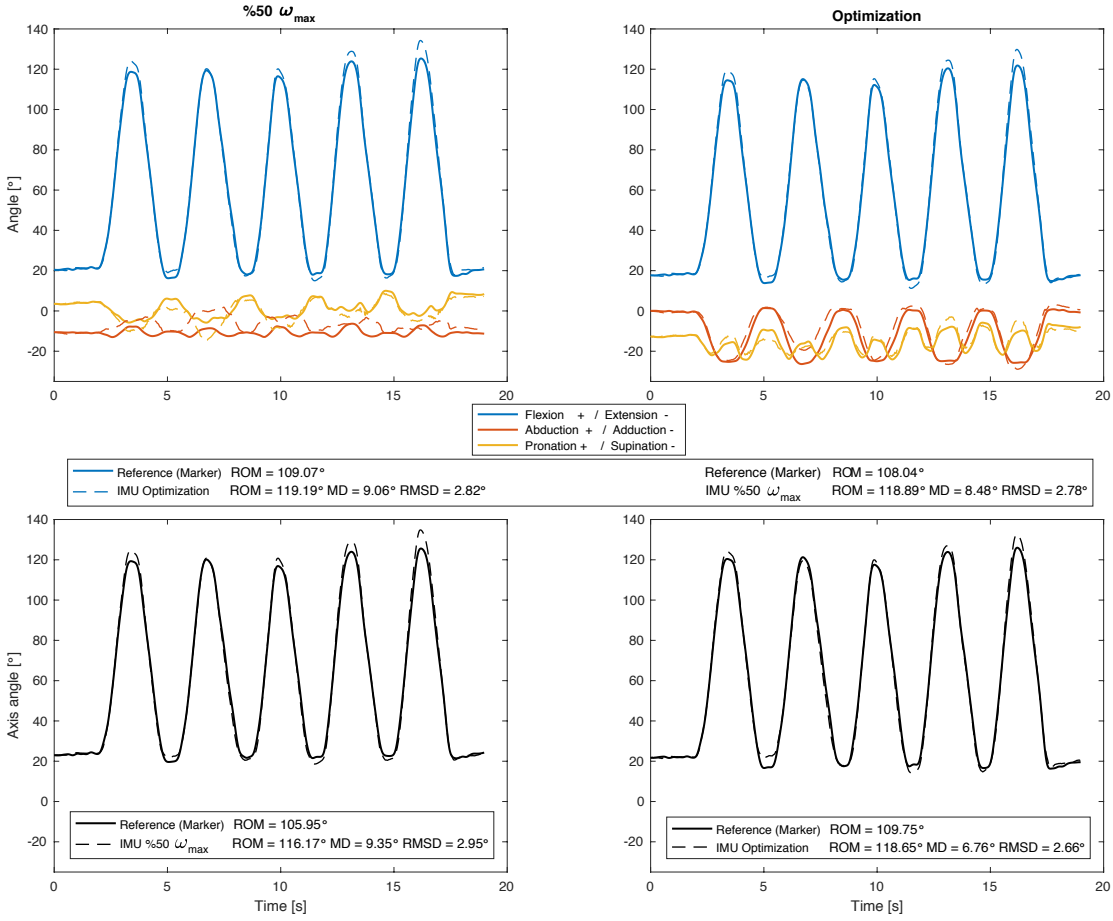

Figure 5-2 Elbow joint angle is represented by Euler angles (with ZXY order). The computation is done based on both $50\%\omega_{max}$ and Optimization methods. The ROM, MD and RMSD of the $50\%\omega_{max}$ method are smaller than the optimization method.

Further to quantify the differences, in Figure 5-2, ROM is the range of the movement (note: in this study ROM is not the joint range of motion), the maximum deviations (MD) and the average deviation (RMSD) between joint rotations by Optitrack and IMU measurements are computed and presented. The ROM, MD and RMSD are to be computed as follows:

$$ROM = \left|\varphi_{\max} - \varphi_{\min}\right|$$

$$MD = \left(\sqrt{\max\left(\varphi_{Optirack} - \varphi_{IMU}\right)^2}\right) \quad \text{, Where } \varphi \text{ is the rotation} \tag{61}$$

$$RMSD = \sqrt{mean\left(\varphi_{Optirack} - \varphi_{IMU}\right)^2}$$

As it can be seen in Figure 5-2, the RMSD and MD of the flexion/extension angle is very similar to the axis angle RMSD and MD. This indicates that the flexion/extension axis is defined well. Besides ROM, RMSD and MD of the two methods are also similar, which is also again evidence of the correct estimation of axis and angles. The MD and RMSD of the $50\%\ \omega_{max}$ method are a bit smaller than the optimization method, which indicate that the $50\%\ \omega_{max}$ method did estimate the axis and angles more accurately.

The rotation of joints during different movements have been computed and compared with the Optitrack reference ones.

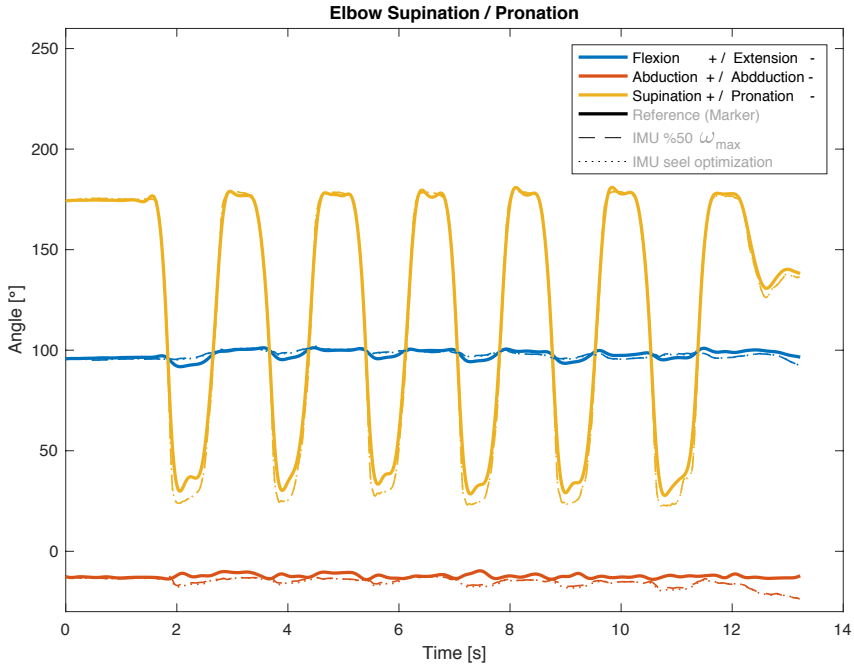

Figure 5-3 The IMU tracking method is able to track the motion and the computed angles are similar to the Optitrack reference method. The two functional calibration methods are roughly identical.

The worse segment to track (the largest RMSD) was the hand due to the error in its orientation. Although the tracking is not fitted with the reference, both IMU motion tracking methods estimated almost the same results presenting about twice bigger angle than the Optitrack reference one (Figure 5-4).

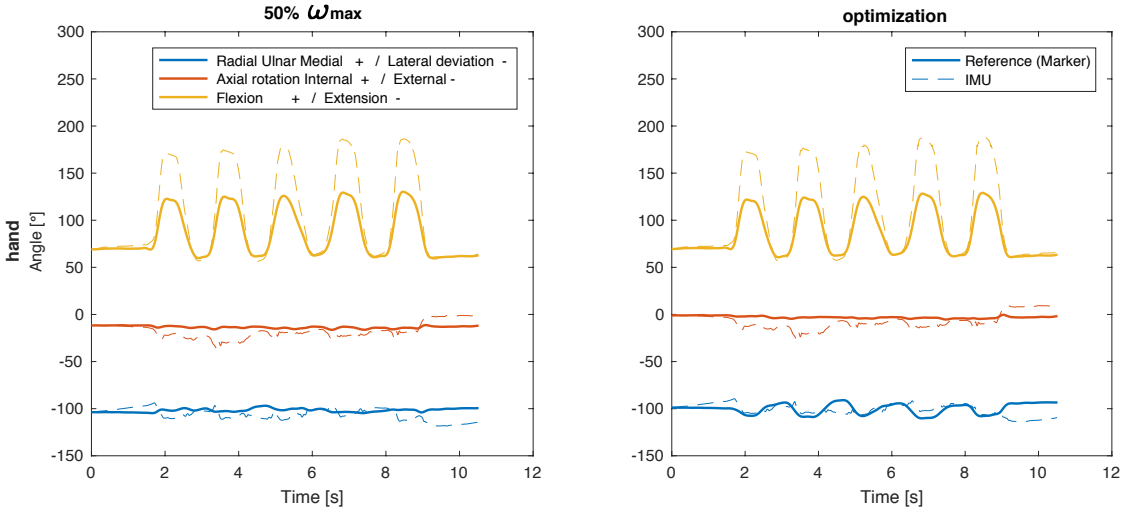

Figure 5-4 Lower arm and hand rotation during elbow flexion/extension. The computation is done with both the $50\%\omega_{max}$ and Optimization methods. IMU estimated bigger rotations with both methods.

This indicates a technical weakness of the IMU sensor on hand that was not able to fit the optitrack reference. It is possible that this is due to technical limitation of the IMU, like some mistake in the IMU calibration. It can also be due to the positioning of the IMU on the hand, which was too close to the wrist joint or the skin motion. Another possibility is that the hand is a small segment and the proportion of the hand mass and length with respect to its IMU is much larger than the proportion of the other body segments with respect to their IMU.

Table 5-1 Joint's rotation comparison of the two IMU-based methods (50% ωmax and Optimization) with the Optitrack reference measurements

Joint	Motion	Motion Type	ROM				MD		RMSD	
			50% ωmax		Optimization		50% ωmax	Optimization	50% ωmax	Optimization
			Optitrack	IMU	Optitrack	IMU				
Shoulder	*Flexion / Extension*	slow	118.0	114.0	119.0	100.9	23.6	24.6	13.2	12.9
		fast	118.0	104.3	118.8	90.7	25.6	26.7	15.0	14.1
Elbow	*Flexion / Extension*	slow	109.1	120.5	109.2	120.8	9.6	9.5	3.0	3.1
		fast	107.8	126.6	107.9	126.9	13.9	14.3	5.3	5.5
	Supination / Pronation	slow	148.4	164.8	149.7	164.7	14.3	13.0	7.0	6.4
		fast	151.1	158.8	152.2	159.5	22.2	22.1	8.3	8.2
Wrist	*Flexion / Extension*	slow	61.8	123.2	63.3	118.1	54.9	50.6	24.3	21.6
		fast	66.2	127.1	67.8	126.4	59.5	56.8	28.6	27.1
	Radial / Ulnar Deviation	slow	42.6	67.5	42.6	65.7	39.1	48.4	11.6	19.0
		fast	74.6	94.0	72.4	93.5	72.3	64.2	20.5	17.5
Hip	*Abdaction/ Adduction*	slow	41.5	40.0	41.5	41.2	7.3	7.4	2.7	3.4
		fast	44.5	47.2	44.5	50.0	8.0	7.4	4.0	2.6
	Internal / External Rotation	slow	72.7	60.6	72.7	60.0	14.0	14.2	9.3	9.5
		fast	61.7	55.1	61.7	54.4	10.3	10.3	3.6	3.7
Knee	*Flexion / Extension*	slow	81.3	100.9	80.1	104.3	18.9	21.0	7.9	8.6
		fast	82.3	127.3	81.4	142.3	55.2	67.5	9.2	12.0
Lumbar joint	*Internal / External Rotation*	slow	39.5	41.2	39.0	41.1	4.7	8.7	2.4	4.1
		fast	49.2	50.3	48.6	51.0	6.9	7.0	2.6	4.4
	Flexion / Extension	slow	24.7	14.3	24.6	12.5	22.5	17.2	9.9	7.0

Table 5-1 shows an overview of computed range of movements (ROM), Maximum deviations (MD) and average deviation (RMSD) between joint rotations by Optitrack and IMU measurements.

As it can be seen in Table 5-1 the rotations tracked by IMU sensors are consistent with the Optitrack reference motion tracking. Both $50\%\ \omega_{max}$ and the Optimization results fit the reference measurements (RMSD<20°) for most trials. The largest dissimilarities are shown by RMSD = 27,1° of the wrist joint, which is due to the error in hand's orientation. The shoulder joint also shows RMSD=14,1°, which was also expected since in this study the complex movements of the scapula was neglected (Hint: in this study we had only one IMU for tracking the motion of thorax and one IMU for tracking the motion of the upper arm). However this simplification is done on

both IMU and marker-based method, still the multiple degree of freedom of the scapula cannot be neglected and might have resulted in this differences.

Another finding from this table is that the faster movements have the larger RMSD and thus they are less similar to the optitrack reference. This can indicate the effect of inertia, which might be prevented by using lighter IMU's. However, the hip joint motions presents a smaller RMSD for the faster movements, which means the joint angle is estimated better in the faster movements. The reason to this can be the method for definition of coordinate system of pelvis and thigh or the calibrations of the pelvis and thigh's IMU. This can also be due to the positioning of IMU on the muscles of thigh. Furthermore, since the Y-axis of pelvis was estimated as the mean of the direction of gravity recorded by accelerometer and the other axis was estimated using the gyroscope data, the error might be due to misalignment of gyroscope and accelerometer sensors. However, in static situation the IMU noise did affect the measurement. As a not moving IMU records noise rather than useful data.

Further more the results show that the $50\%\ \omega_{max}$ method has a RMSD of equal or smaller than the optimization method, and reduces the effect of cross talk between the axes. Moreover, the computation with the $50\%\ \omega_{max}$ method takes around 10s, while the optimization method takes around 500s (for 10s of data recordings with a sampling frequency of 500 Hz). Therefore, the $50\%\ \omega_{max}$ method is superior to the optimization method.

5.2 Angular velocity and acceleration

5.2.1 Segment's angular velocity and acceleration

Segments angular velocities and accelerations are also compared. For a motion like shoulder flexion/extension, with elbow extended and wrist at 0° flexion, it is expected that the lower and upper arm and the hand would have almost the same angular velocities. As it was mentioned in section 5.1, the hand's IMU results do not seem reliable. This issue is also appearing on the velocities and accelerations level. Figure 5-5 shows how the upper and lower arm angular velocity is fitted with the Optitrack reference, and the hands velocity is overestimated.

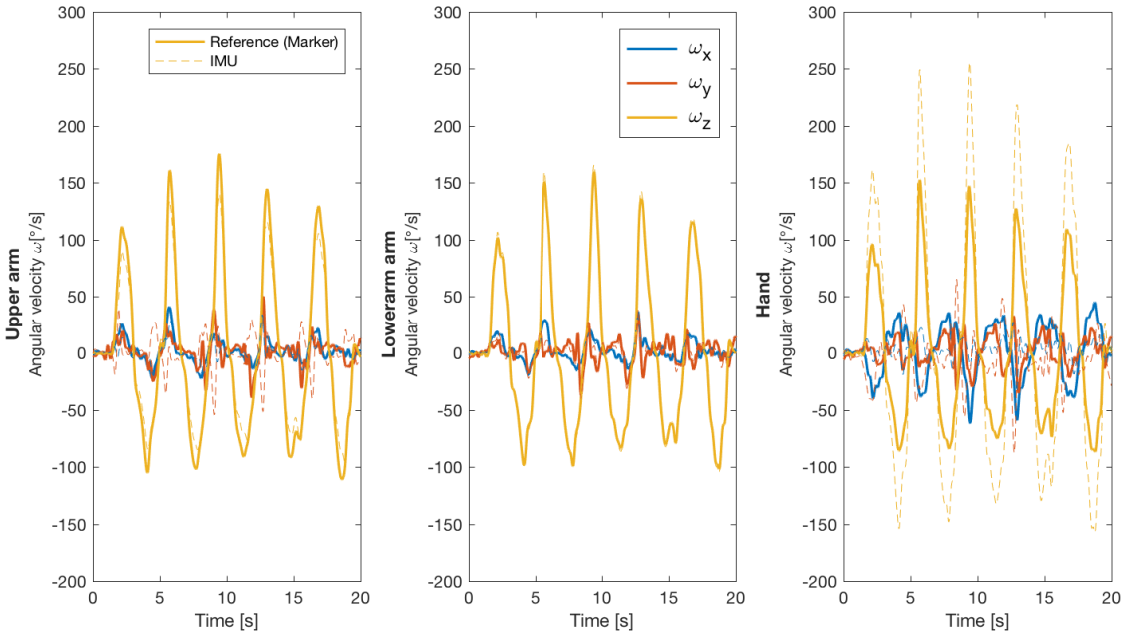

Figure 5-5 Arm segments have almost the same angular velocities during shoulder flexion/extension.

Figure 5-6 shows as an example the angular velocity and accelerations of the lower arm during flexion and extension. Patterns and signs are similar with difference in peaks of 10 to 50°/s in velocity level and 50 to 1500°/s² in acceleration level. The differences are smaller in velocity but can reach around 30% for the accelerations.

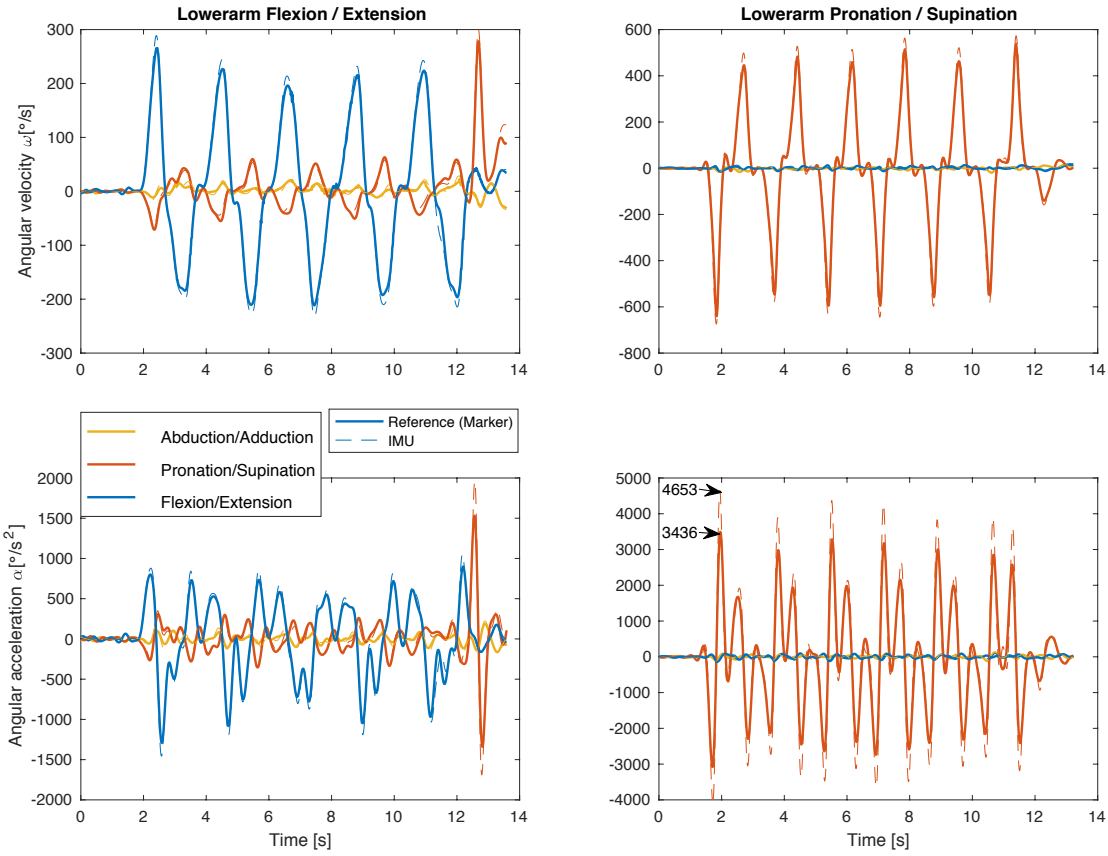

Figure 5-6 lower arm's angular velocity and accelerations during flexion and extension

5.2.2 Joint's angular velocity and acceleration

Joint's angular velocity and accelerations are also compared. This comparison is done in the joints coordinate system.

It is also interesting that the joint's angular velocities and accelerations (Figure 5-6) which is computed from the differentiations of quaternions ($\omega_q = 2\dot{q} \otimes \overline{q}$ and $\alpha_q = 2\left(\ddot{q} \otimes \overline{q} + \dot{q} \otimes \dot{\overline{q}}\right)$), is similar to segments angular velocity and accelerations (Figure 5-7) which is computed by multiplications of the gyroscope data and the rotation matrix from IMU to the segment ($\omega_{FCS} = R_{FCS \to MCS} * \omega_{MCS}$ and $\alpha_{FCS} = R_{FCS \to MCS} * \dot{\omega}_{MCS}$).

The similarities of, Figure 5-6 and Figure 5-7 confirms the correctness of the results either via differentiation or direct from the recorded data.

Figure 5-7 shows the angular velocity and accelerations of elbow during flexion and extension. In this trial, since the upper arm was kept still and only the lower arm was flexing and extending and therefore the elbow joint velocity and accelerations is almost equal to the elbow's velocity and accelerations (Figure 5-6).

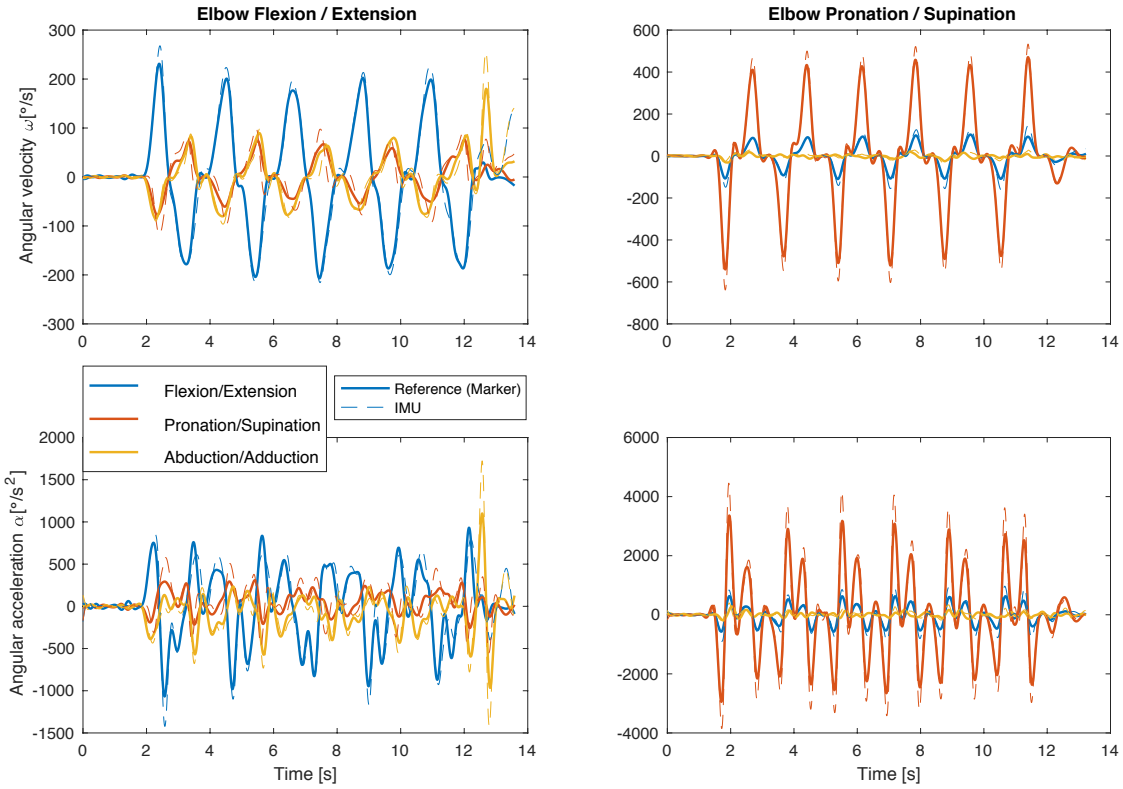

Figure 5-7 Elbow joint's angular velocity and accelerations during flexion and extension

Figure 5-7 shows similarly to the segment velocities and accelerations, the marker and IMU also have tracked the joint angular velocity and accelerations of the lower arm during flexion and extension with the same signs and pattern. However the peaks are different. The difference in peaks are around 10 to 50°/s in velocity level and 50 to 1500°/s² in acceleration level. The differences are smaller in velocity but can reach around 30% for the accelerations.

The velocities and accelerations of joints during different movements have been computed and compared with the Optitrack reference ones.

Table 5-2 Comparison of the angular velocity and accelerations computed by the IMU-based method (50% ωmax) with the Optitrack reference measurements

Joint	Motion	Motion Type	Angular velocity $[°/s]$						Angular acceleration $[°/s^2]$					
			ROV		MAX		MD	RMSD	ROA		MAX		MD	RMSD
			Optitrack	IMU	Optitrack	IMU			Optitrack	IMU	Optitrack	IMU		
Shoulder	Flexion / Extension	slow	276	208	170	122	49	17	892	1093	506	383	708	66
		fast	391	291	231	161	83	26	1616	1201	780	614	558	144
Elbow	Flexion / Extension	slow	234	261	123	137	25	8	1015	981	470	378	240	72
		fast	438	483	231	268	154	25	1999	2272	932	850	478	148
	Supination / Pronation	slow	408	411	195	204	33	7	1462	1642	860	870	311	76
		fast	1012	1171	471	533	98	27	6309	8303	3361	4454	1248	391
Wrist	Flexion / Extension	slow	105	184	51	77	81	22	517	1259	298	690	907	202
		fast	191	294	89	127	73	25	1228	2024	707	1298	674	223
	Radial / Ulnar Deviation	slow	172	351	89	199	121	28	784	2071	343	706	924	136
		fast	364	723	198	410	279	65	2514	4693	1519	2511	1946	552
Hip	Abdaction/ Adduction	slow	209	223	104	114	38	10	1123	1126	599	589	254	83
		fast	300	300	144	154	23	8	4174	1750	1457	871	2648	136
	Internal / External Rotation	slow	312	265	169	144	34	13	1784	1481	859	811	278	101
		fast	453	417	236	216	29	13	3293	3190	1594	1642	1109	168
Knee	Flexion / Extension	slow	260	271	154	161	69	20	1053	1320	599	555	561	146
		fast	357	362	202	204	124	25	1759	1779	849	710	803	174
Lumbar joint	Internal / External Rotation	slow	13	22	7	11	10	4	135	226	77	62	164	29
		fast	22	58	9	28	27	12	165	449	85	261	231	87
	Flexion / Extension	slow	92	55	54	28	35	15	556	1586	295	1334	1333	87

Table 5-2 shows an overview of computed ROM, MD and RMSD between joint rotations by Optitrack and IMU measurements. ROV is the range of the velocities changing and MAX presents the absolute maximum velocity or acceleration.

As you can see in Table 5-2, faster trials have larger RMSD than the slower ones. This means, in slower joint rotations, the angular velocities and accelerations better fit the Optitrack reference data.

The numerical differentiation works as a high pass filter, which means any errors in the 3D positions will be amplified with each differentiation step. Indeed, the IMU measures the angular velocity and need one differentiation step to compute the angular acceleration. Where the marker data needs respectively one and two differentiation steps to compute the angular velocity and acceleration. Thus, the IMU results are expected to be more accurate at velocity and accelerations level. This fact makes it difficult to analyses of the results presented in Table 5-2.

5.3 Segment length estimation

Figure 5-8 shows the computation of the distance between the two adjacent IMU (of lower and upper arm) and the elbow joint during five flexion/extension of the elbow. The mean of these results is the position of joint with respect to the elbow joint.

The computation of the position of IMU with respect to the joint is based on the angular velocity and linear accelerations measurements. Indeed, if the segment is almost not moving, the noise from the IMU sensor will have more influence. When the upper arm is not moving, the recordings of IMU are mostly noises, and thus the computation of the distance of joint and IMU would not be accurate. This is presented in Figure 5-8, by uncertainty in the results of the optimization search for the position of the joint with respect to the IMU.

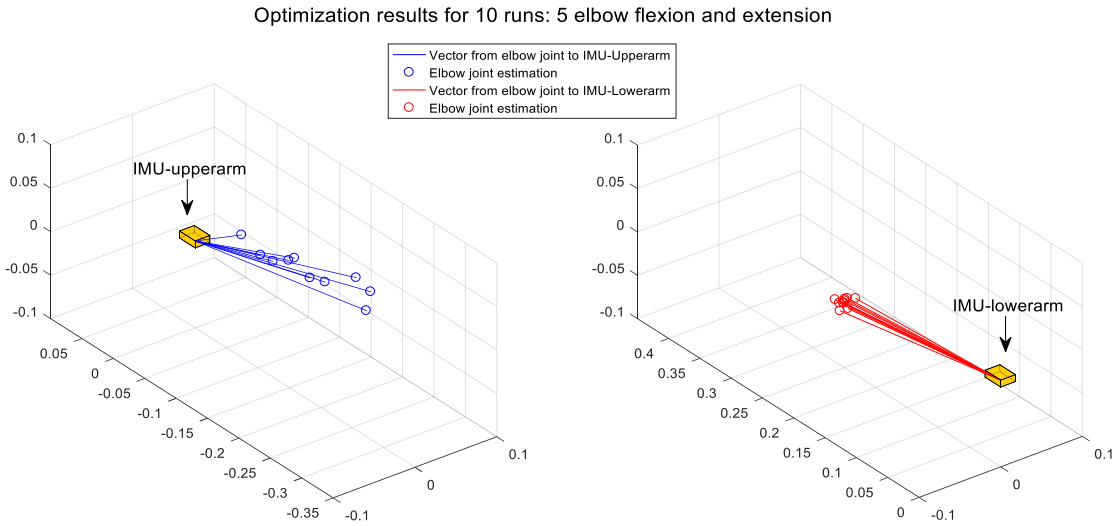

Figure 5-8 Computing the distance between the two adjacent IMU (of lower and upper arm) and the elbow joint during 5 flexion and 5 extension. The mean of these results is the position of the joint with respect to the IMU sensor. Here the upper arm has low speed and lower arm has high speed.

Figure 5-9 shows the distribution of this optimization. Here it is better visible that the distribution is narrow in x and z direction of the IMU axis and the wide distribution is presented along the y-axis. This is an evidence that the optimization process works and is able to find the position of joint to be on an line through the IMU but the distance of the joint with respect to the IMU on this line was not found perfectly, since the IMU was not moving (and recording) enough acceleration and velocity data.

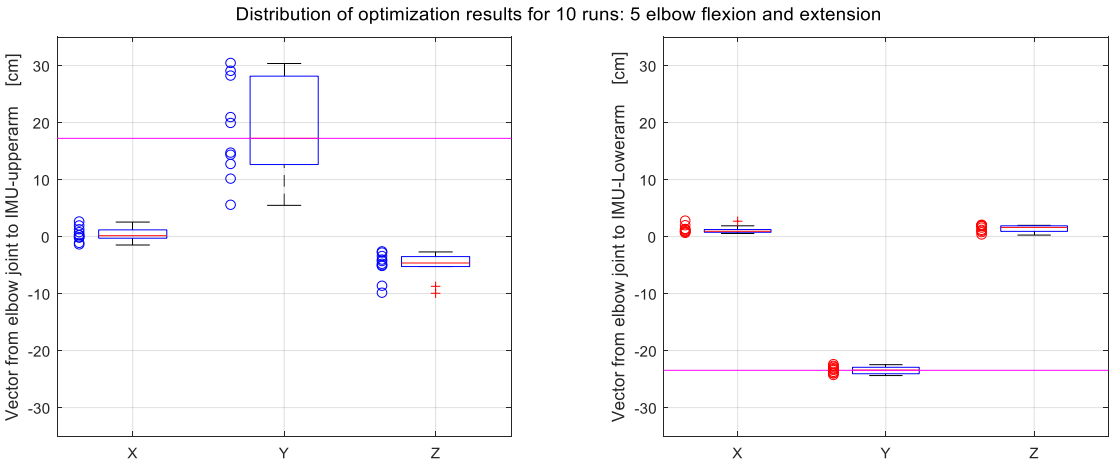

Figure 5-9 Distribution of optimization results of the IMU with respect to the joint of a not moving segment is not adequate (10 runs= 5 flexion + 5 extension).

Besides, Figure 5-9 shows, although the distribution of upper arm IMU to the elbow joint is wide, the mean value of it (17.23 cm) is similar to the one from Optitrack data (16.1 cm) in slow flexion/extension of elbow trial. But this is a matter of having enough repetition of the motions in the measurements. For a better computation of joint position with respect to the IMU, it is better to choose the data from the trials in which the joint is moving.

Using two series of such optimizations, each segment length can be computed. Table 5-3 shows the segments length computed from IMU measurements against the Optitrack one.

Table 5-3 Segments length [cm]

		Optitrack		IMU	
Hand	**IMU to WJC**	7.5		1	Wrist flexion/extension
Lower arm	**EJC to WJC**	26.7		24.5	Squat
Upper arm	**SJC to EJC**	31		31.3	Squat
Trunk	**SJC to Sagittal plane**	22.8		18	Shoulder flexion/extension
Pelvis	**HJC to Sagittal plane**	13.1	Stand	13.3	Hip adduction / abduction
	HJC to IMU	22		17.2	
Thigh	**HJC to KJC**	43		37.3	Lunge + Knee flexion/extension
Shank	**IMU to KJC**	11		12.2	Knee flexion/extension

The segment lengths are estimated with small difference from the Optitrack reference measurements. The largest difference is on the hand IMU, which was expected since all the measurements on the hand IMU indicate that this IMU probably had a technical issue. The other large difference is the thigh length, with an error of 7% of its length, which is reasonable. It was not possible to estimate the total length of shank and hand, where as there is no other segments attached with an IMU at their distal end.

Note that the IMU's segment lengths are estimated during calibration movements using the above optimization process when both segments are moving around each joint. The segment lengths from the Optitrack measurements are based on the joint distances during standing position when the segments are not moving. For trunk and pelvis the position of SJC and HJC to the sagittal plane is estimated by regression equations (Dumas, Cheze et al. 2007) which are prone to errors that can be up to 3 cm (Fiorentino, Kutschke et al. 2016). Thus, the estimation from the IMU functional calibration could lead to a more accurate value than the regression.

5.4 Pitching and Power flow

In this section we want to analyse the power estimated by IMU-based measurements. This analysis needs to be done on the pitching measurements. Although, the subject of this project was not a real baseball pitcher, we measured two kind of pitching motions; first a pitch with the whole body moving, second a pitching motion where only the arm is moving. Analysing these motions will help to understand if our method is valid to track a baseball pitcher motion.

Since the ultimate goal of this project is tracking the pitching motion in baseball, it is interesting to look at the internal rotation of shoulder when the arm is flexed and the lower arm is horizontal. If the method is able to track this motion, it is evidence that the pitch could also be tracked.

5.4.1 Kinematic results

Figure 5-10 shows the internal rotation of shoulder estimated by both $50\%\,\omega_{max}$ and Optimization methods fit the Optitrack reference.

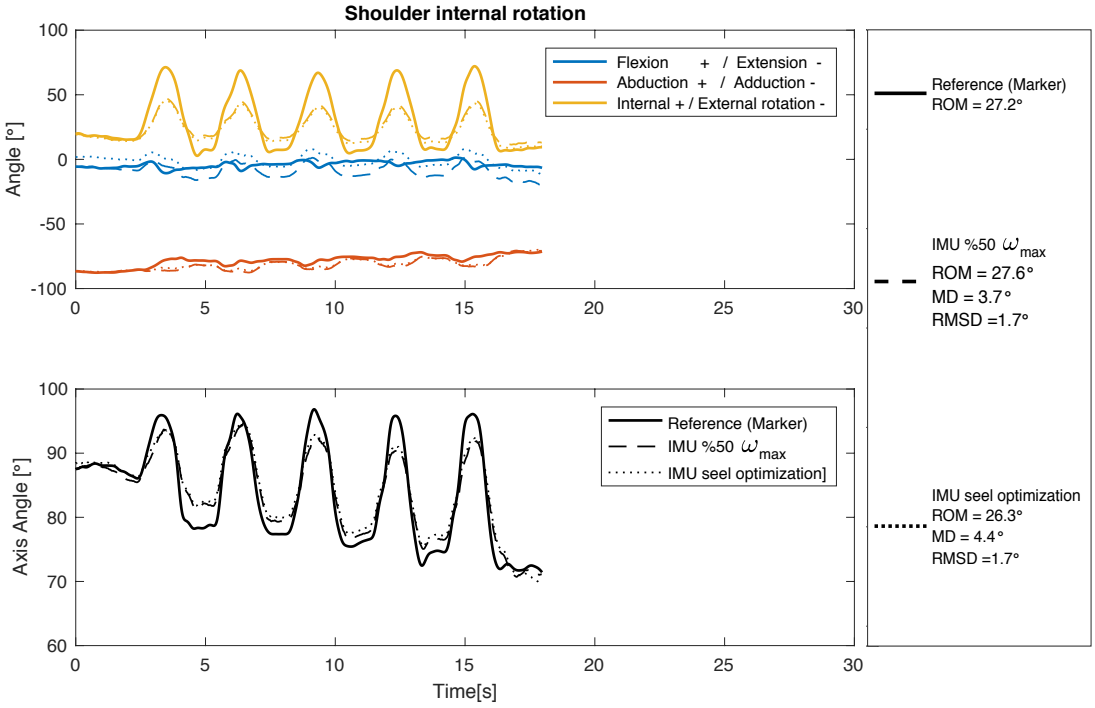

Figure 5-10 Small shoulder internal rotation estimated by IMU, using both $50\%\omega_{max}$ and the Optimization fits the Optitrack reference

Figure 5-10 shows that the internal/external rotation of the shoulder is tracked using both IMU methods are similar (RMSD = 1.7°). The maximum deviation is smaller using the $50\%\,\omega_{max}$ method (MD=3.7°) than the optimization method (MD=4.4°). This is logic since the $50\%\,\omega_{max}$ method uses the frames with larger velocities than the optimization method for estimation the orientation of the axis. The range of the movement (ROM) is tracker better by the $50\%\,\omega_{max}$ method.

The next step is looking into the pitch motion. Note that the subject was not a real baseball pitcher and the results are a proof of concept. Figure 5-11 shows that the changes of Euler angles align with the axis angle for the shoulder, elbow and wrist during 5 repeated pitching motions where the subject stands still and only tries to pitch the ball with his arm.

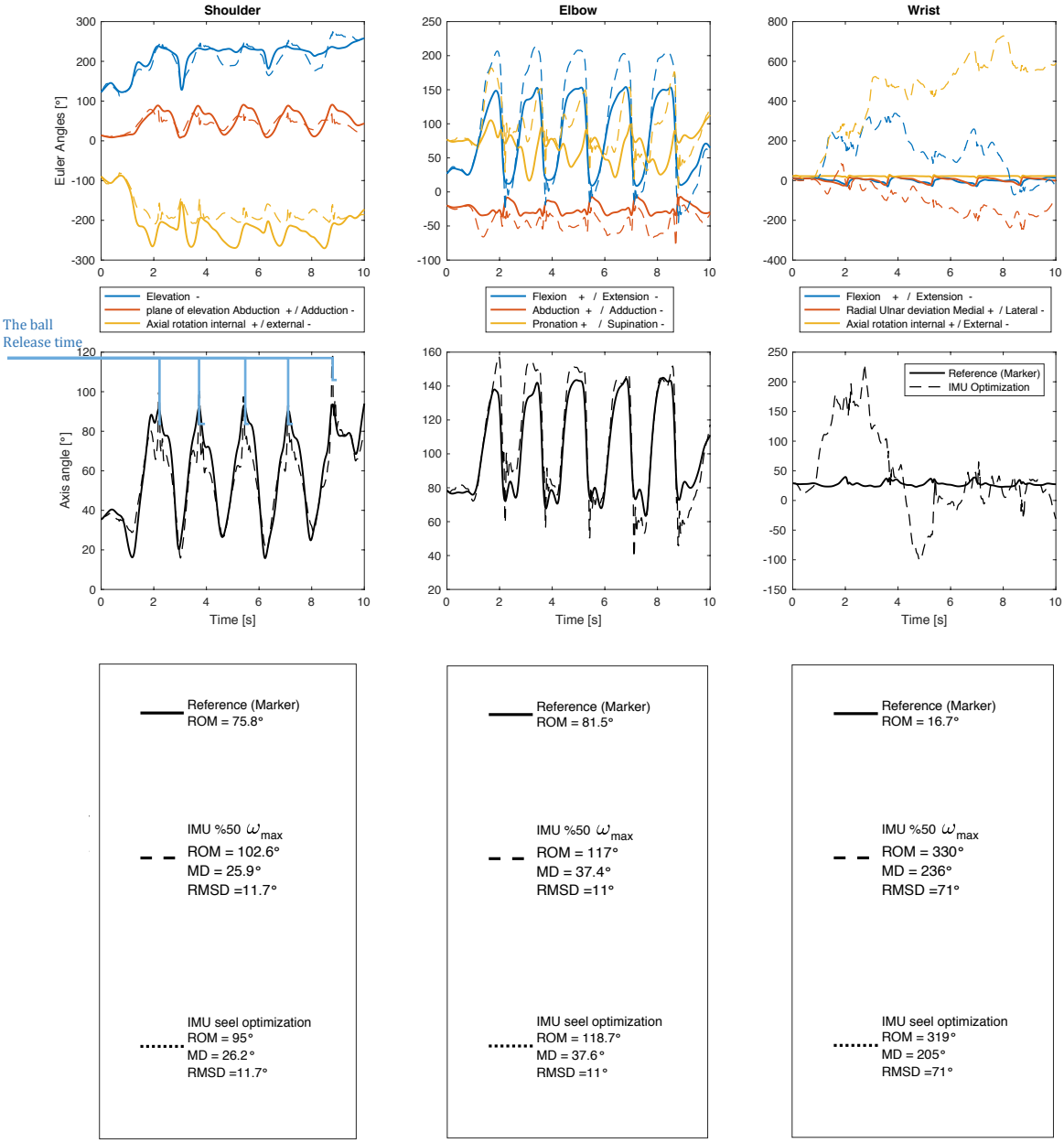

Figure 5-11 shoulder, elbow and wrist rotation angles during 5 pitches

Figure 5-11 shows that the IMU based measurement resulted in an overestimated elbow flexion (above 180°). In general we would expect under 180° elbow flexion/extension. The angular velocities and accelerations measured by IMU did encounter data clipping. This should be the reason for this angle overestimation. However, it is interesting that the axis angle changes are between 40 and 160°which is reasonable. The elbow joint has mainly 2 degree of rotation; flexion/extension and pronation/supination and a small abduction/adduction. It is possible that this problem is due to miscalculation of segment coordinate system. In that case the question is how did we then acquire a low RMSD = 3 to 8° for the elbow flexion/extension and pronation/supination? This is evidence that this error is most likely related to the high speed of motion during pitching movement and subsequently the data clipping.

The shoulder and elbow joint rotation estimated by IMU sensors, using both methods fits the Optitrack reference (RMSD = 11.7 and 11°). Again, this result confirms the maximum deviation is smaller using the $50\%\,\omega_{max}$ method (MD=25.9 and 37.4°) than using the optimization method (MD=26.2 and 37.6°). Although the difference is not large, the $50\%\,\omega_{max}$ method does better than the optimization method.

The IMU shows some peaks, which can be related to the fast angle changes an data clipping close to the pitch moment. The Optitrack did not record these peaks, which can be due to lower frame rate in Optitrack (Optitrack measurement with 120Hz vs. IMU measurement with 500Hz).

The wrist Joint rotation dose not fit the reference, which was expected since it looks as if this IMU had some technical problem. Besides, the motion is so fast that the IMU reaches the threshold of gyroscope and accelerometer (data clipping).

Figure 5-12 shows the data clipping in the linear acceleration recording of IMU on the lower arm during pitching.

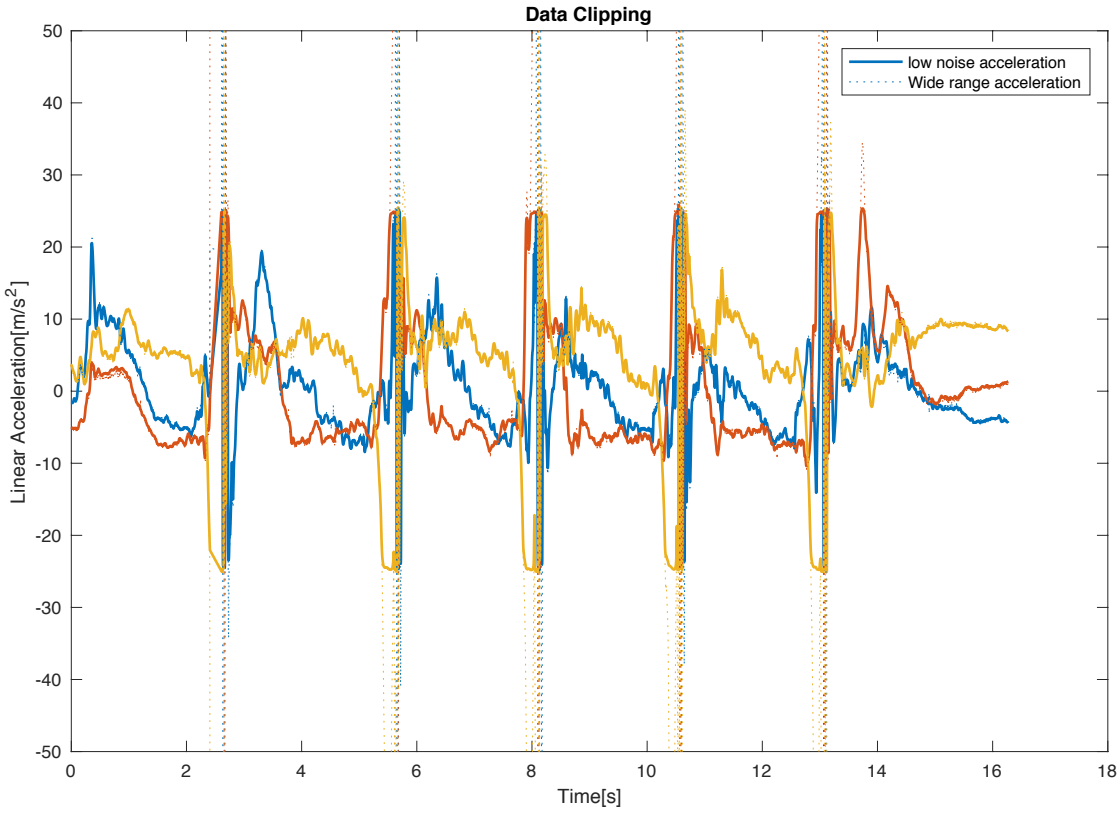

Figure 5-12 data clipping of accelerometer during pitching.

5.4.2 Kinetic results

5.4.2.1 Kinetic energy

The segments kinetic energy estimated based on Optitrack a measurement is depicted in Figure 5-13.

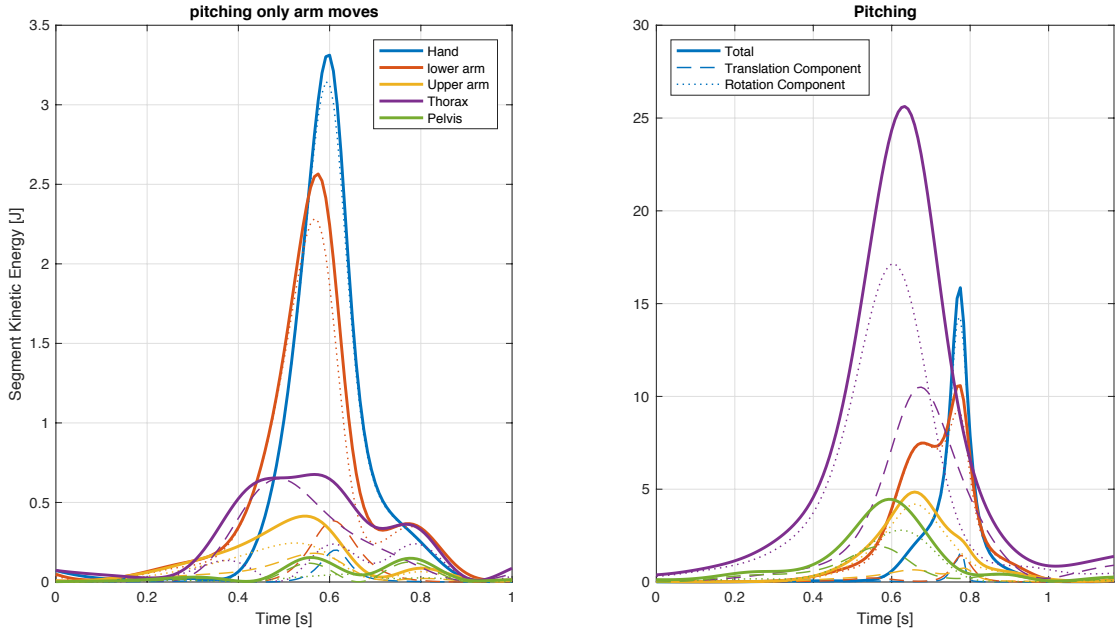

Figure 5-13 Segment's kinetic energy based on Optitrack measurements.

In Figure 5-13, the left graph is a pitching motion where only the arm is moving. Here it is visible that the pelvis energy is almost zero since it is not moving. The thorax energy is a bit larger due to the heavy mass of thorax, which is appeared more in the translation component. Upper arm velocity is larger but its mass is smaller than thorax. The lower arm builds up more energy due to its rotational and translational speed and this speed is transformed to the hand too. The hand has the largest energy at the moment of ball release. The right graph shows a pitch with the whole body moving. The increase of kinetic energy is significant, compared with when the whole body is not moving in the left graph. Thorax gains the highest energy due to its large mass. The peak in hand shows the ball release moment. After the ball release the energy is decreasing to the static condition of around zero.

The total kinetic energy of each segment is the sum of translational and rotational kinetic energy of the segment. Since the linear velocity of centre of mass was not estimated adequately using IMU measurements, we attempt to compare only the rotational part of kinetic energy in Figure 5-14.

This attempt is not presenting the expected results. The rotational part of kinetic energy of thorax is around 17% underestimated. The upper arm is around 50% overestimated. The lower arm and hand present two consecutive peaks, which should be due to data clipping. From the magnitude of the peaks, it is predictable that the lower arm and hands rotational kinetic energy was overestimated if there was no data clipping. Indeed it is also possible that the marker-based measurement did underestimate the energy.

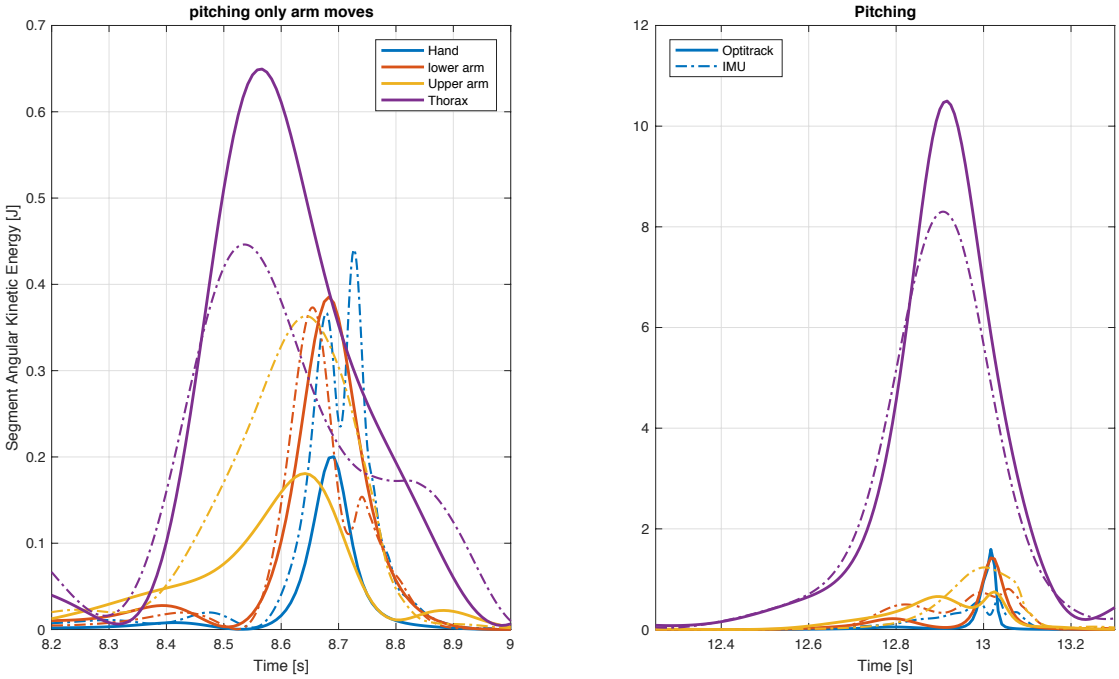

Figure 5-14 Rotational component of the segment's kinetic energy based on Optitrack and IMU measurements.

5.4.2.2 Power

The segments power estimated based on Optitrack measurements is depicted in Figure 5-15.

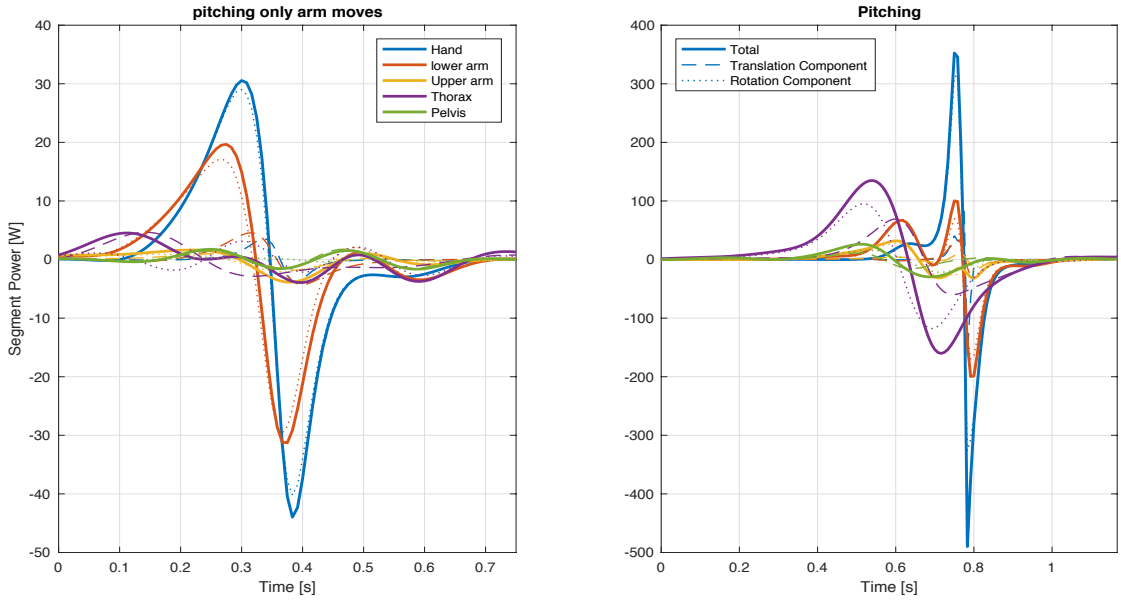

Figure 5-15 Segment's power based on Optitrack measurements.

Since the pitches were not preform by a real pitcher, the results are not exactly depicting the event sequences and the magnitude of power during pitching. Yet it is visible the power is building up in segments from pelvis to hand to preform the pitch.

The total power of each segment is the sum of translational and rotational power of the segment. Since the linear velocity of centre of mass was not estimated adequately using IMU measurements, we compare only the rotational part of power in Figure 5-16.

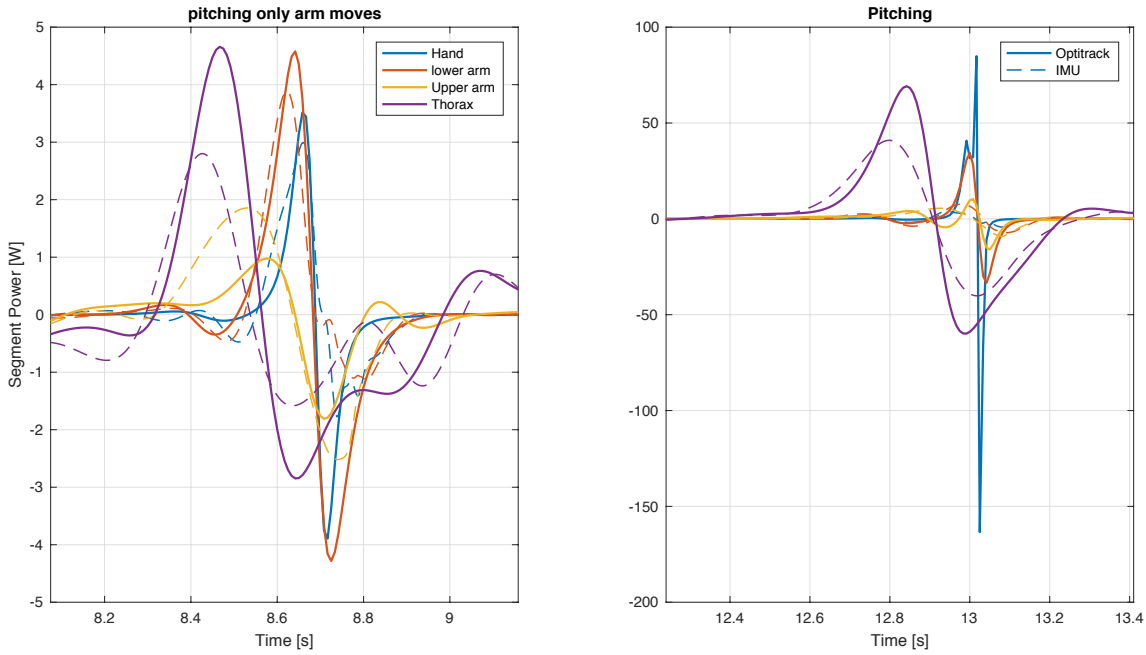

Figure 5-16 Rotational component of the segment's power based on Optitrack and IMU measurements.

The rotational component of the hand, lower arm and upper arm's power computed by the IMU based measurements are reasonably fitted with the marker-based reference. This is not the case for thorax. For thorax the sign and pattern of changes are similar but the magnitude difference is large. This should be due to the position of the thorax and the scapula movements.

The joints power estimated based on Optitrack and IMU measurements are depicted in Figure 5-17.

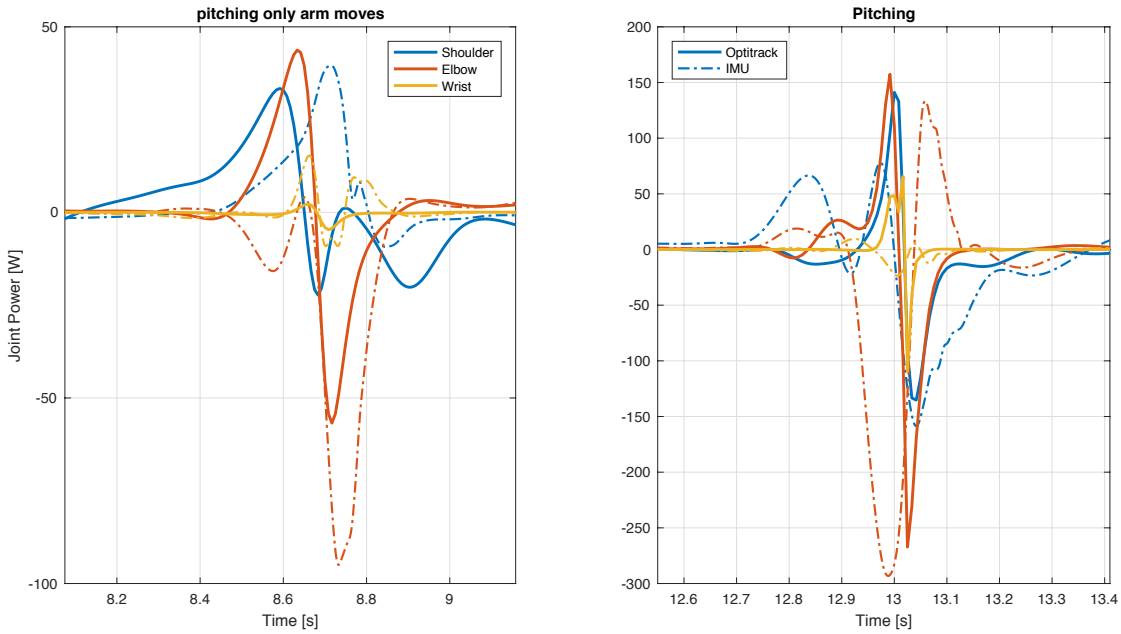

Figure 5-17 joints power

Figure 5-17 shows the difference in the peak timing and magnitude difference between the

IMU and marker based estimated joint powers. The reason to this is the errors in computation of forces and moments applied at joints and the linear velocity of the CoM of the segments from the integration of the linear acceleration recorded by the IMU. The data clipping can also be a source of error. The following sections present a short overview of this miscalculation.

5.4.2.3 Velocity

The linear velocities of the segments are computed by one step integration, which results a drift in the computed velocity. The drift can be linear, and we can compensate it having some workaround. For example, knowing that at the beginning and end of the measurement the segment is not moving and the velocity is zero (Figure 5-18).

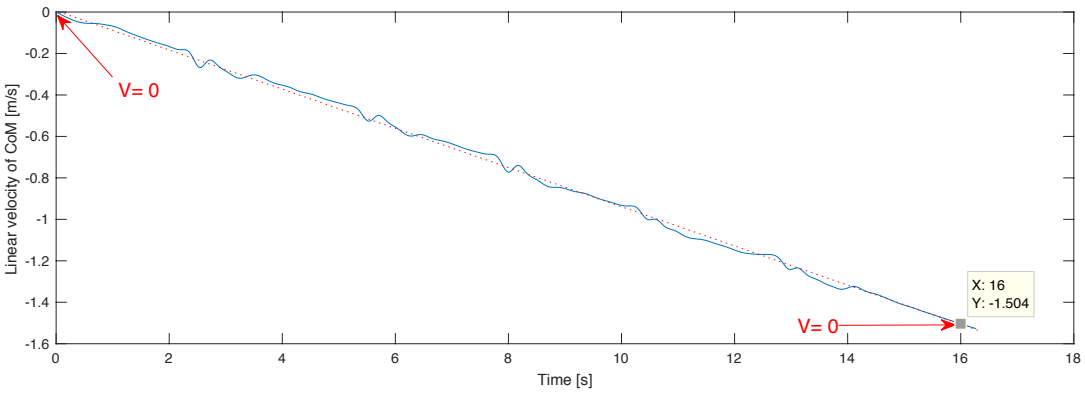

Figure 5-18 Drift in velocity due to computation of velocity by integration of acceleration (norm of the velocity of upper arm centre of mass)

However, even though this drift is linear, we face another problem especially for the lower arm and hand. The reason to this should be the data clipping due to the limit of accelerometer; we are not able to compensate for the integration drift. The problem existed on both low noise and wide range accelerometer sensors. Figure 5-16 shows the data clipping results the error in linear velocity computation.

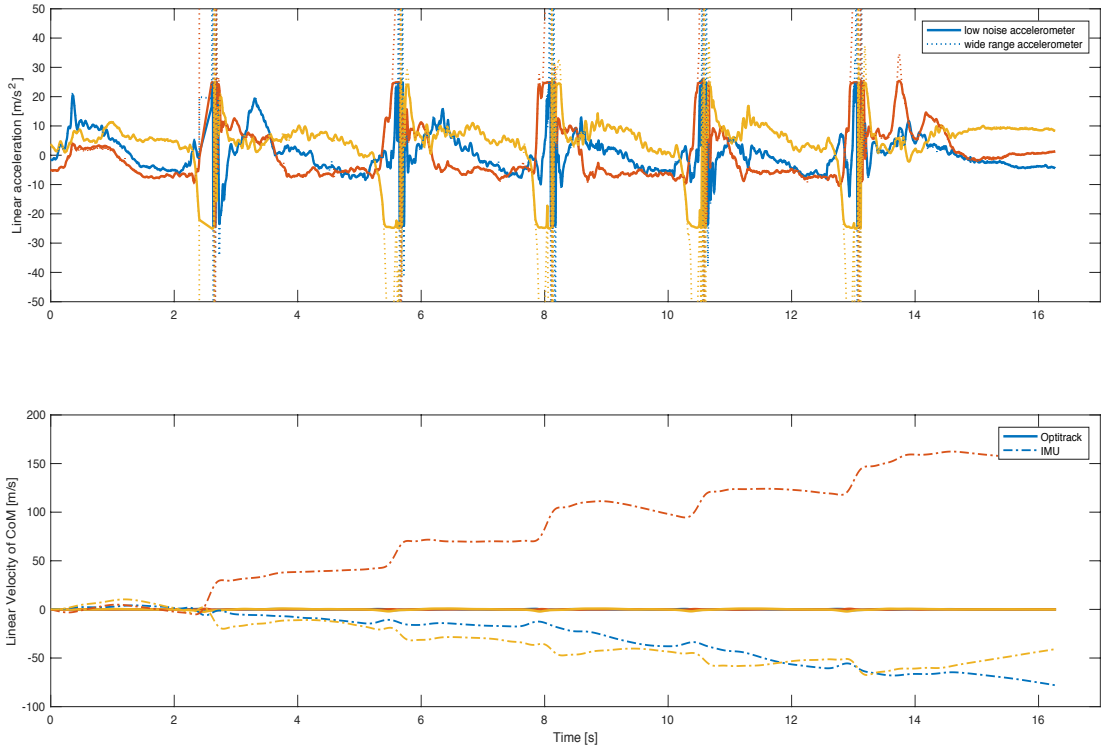

Figure 5-19 Drift in velocity due to computation of velocity by integration of acceleration of lower arm due to data clipping of accelerometer during pitching.

5.4.2.4 Joint force and moment

Joints forces and moments are estimated for both IMU and Optitrack measurements. The results show the forces at the wrist with IMU are similar to the Optitrack measurements, however its moments are much lower. This could be due to underestimating of the hand length by IMU as it was presented in table 5-3. As the forces and moments are computed respectively starting from hand and then elbow and shoulder, this error would also effect the estimation of forces and moments at elbow and shoulder. Also all the errors in accelerations affect this computation.

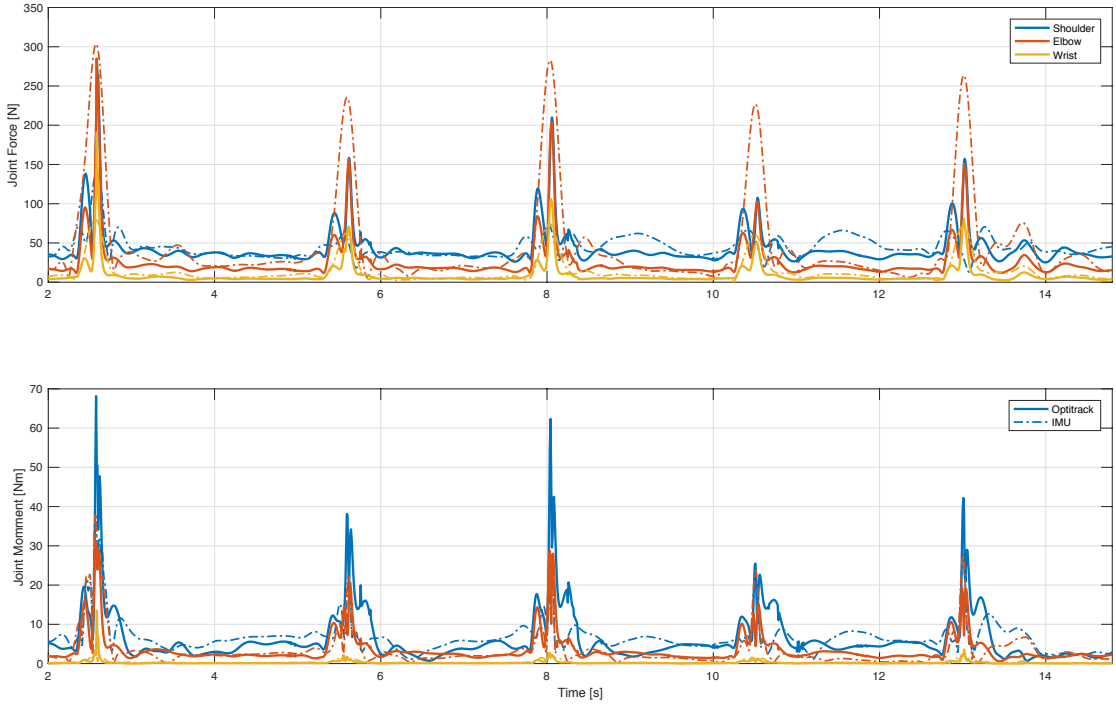

Figure 5-20 joints forces and moments during 5 pitches

Chapter 6

Conclusion & Recommendations

The aim of this study was development and validation of an IMU's motion tracking system for measurements of baseball pitcher kinematics, having the marker-based motion capture data as the reference. The method development and evaluation are discussed in the previous chapters. This chapter presents gives an overview of the achievements of this study and the concluded outcomes from the discussed results in the previous chapters and recommendations for future studies.

☑ A comprehensive validation of IMU-based motion tracking is done.

The most interesting thing about this project is that for the first time to our knowledge the measurements has been done and validated at the same time on upper and lower extremities and trunk on many joints and segments. The kinematic analysis has been validated at different levels of segments and joints rotation angle, angular velocities and accelerations. The results are verified with the marker-based measurements and with another well-known method from literature (Seel, Schauer et al. 2012).

☑ The segment lengths are estimated.

For the first time, the kinematic analysis of the human body is followed by the segment lengths estimation using both IMU sensor data method for kinetic computation. These estimated segment lengths are validated against the marker-based measurements. Subsequently the segment lengths have been used as the scaling factors in an anthropometric human body model, to estimate the mass and inertia of the segments.

☑ A convenient functional calibration protocol was established.

An IMU-based human motion tracking system has been developed. A practical measurement protocol for placement of the IMU sensors and calibration procedure has been established in which there was no need of specific placements and orientation of the IMU sensors with respect to the anatomical axes of the segments, as needed in most of previous studies. Specific tips are

introduced to find the orientation of the IMU regarding known standard static positions, like looking into the gravity direction presented in the accelerometer data or comparing the changes of gyroscope angular velocity against the direction of the movement. This information could potentially provide us the necessary knowledge to get the axis direction. The functional calibration motions are specified to define the coordinate system of each body segment. This area still needs more work and functional calibration protocol could be improved further to minimal set of movement (such as a squat with upper limb extension as has been shown in Figure 6-1, where ankle, knee, hip, shoulder and elbow are rotating together).

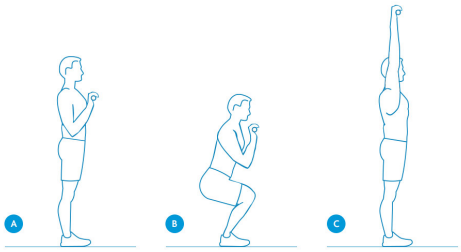

Figure 6-1suggested squat motion with upper limb extending as calibration motion

☑ A fast and convenient method is introduced to compute the joint axis.

Functional calibration method used in previous studies was performed by different routines to rotate the joint in a way to minimize the out of plane rotations. For example, by passive controlled rotation (van den Noort, Ferrari et al. 2013), or by narrowing the rotation angle (Seel, Raisch et al. 2014) or randomly choosing a few (4 to 10) frames which the accuracy of the results would be random (Seel, Schauer et al. 2012). In this study we presented a novel method to find the functional coordinate system of joint, which exclusively use the frames with higher angular velocity during a number of repeating large joint rotation preforming actively by subject (see Figure 4-11).

☑ The 50% ω_{max} method has been verified.

The results show that the 50% ω_{max} functional calibration method is verified for joint axis computation. The 50% ω_{max} method is even more reliable than a time-consuming optimization routine, in reducing the effect of cross talk between the axes (as you can see in Figure 5-2) and matching with the marker-based measurements.

It was noticed that the slower the joint rotation, the more noise in the measured data by the IMU sensor and that could results in less accurate functional calibration. In the case of using optimization method with a random frame selection over repeated joint rotations, it is suggested to select the data from higher angular velocities in which the joint is rotating smoothly. However, the comparison of the RMSD of slow and fast joint rotation in Table 5-1 indicates that the faster movements are less successful in tracking the movement. Therefore the conclusion is that a smooth joint rotation is desired not a fast one. And the purpose of removing frames with lower velocities is to discard the not smooth parts. The advantage of the 50% ω_{max} method is that the method comprises simple and fast calibration movements. The method could compute joint axis based on repeated movements in two directions and remove the frames, in which the joint rotation direction is changing.

Moreover, the computation for the ω_{max} method over a 10 s data of 500 Hz, takes around 12 ms while the optimization method takes around 500 s. Comparing the results of the IMU-based measurements against the marker-based measurements shows that the root-mean-square deviation (RMSD) of the joint angles has been 2 to 27°, angular velocities 4 to 180°/s and angular acceleration 29 to 599 m/s^2. The only joint angle with an error of larger than 20° was the wrist, which was due to the hand's IMU calibration error.

☑ The results of the 50% ω_{max} method have been validated.

In order to validate the kinematic measurements, the method is verified with Seel et al. 2012 to 2016 optimization methods. The results of our method are similar to the optimization method of Seel and in some cases it is even better in tracking the joint angles. Table 5-1 shows that the difference between the 50% ω_{max} method and the optimization method is in most of the cases smaller that 2°. Besides, it is noticeable that the 50% ω_{max} method has in most of the cases a smaller RMSD than the optimization method. Therefore, the 50% ω_{max} method is validated based on the similarities of the results of these two functional calibration methods.

At velocity and accelerations level the IMU measurements are more trustable not only due to avoiding differentiation amplification inaccuracy but also due to the higher sampling frequency of the used IMU sensors. Therefore, the fact that the results show a smaller RMSD for tracking the slower motions, where the marker data are more reliable than the faster motion is also validating the results.

☑ A dual synchronized measurements method was developed.

The human motion has been captured using two systems; IMU and Optitrack. The analysis confirmed that the measurements are accurately synchronized. A method has been developed to assess the kinematics and kinetics of the joints and segments based on both measurement systems. Furthermore, the synchronization method can be used in following studies.

☑ Some suggestions are given to improve the quality of following studies.

The largest dissimilarities are at wrist joint, which is due to miscomputation of the hand's orientation. It is suggested to use a better IMU on hand (wider range of sensor detection and lighter). The shoulder joint's rotation was not fitted also very satisfactory (RMSD=14°). This was expected since the shoulder and scapula have complex movements and in this study we had only one IMU tracking motion of thorax and one IMU tracking the motion of upper arm. It is suggested to also track the clavicle and scapula (one IMU can get either clavicle or scapula).

☑ The distance between IMU and the joints are estimated.

The distance between IMU and segments where computed based on the physical fact that: "when a joint is moving, the acceleration of the joint centre is identical in both IMU's coordinate systems". Based on this statement, the distance between the joint and the two IMU on two adjacent segments is computed using optimization of the recorded data.

This method is used by Seel et al. studies on the functional calibration movements where the joint is kept still. Since when one IMU sensor is kept almost still, the IMU records zero angular velocity and the optimization results are random and the results shows that the joint can be anywhere with respect to a not moving IMU and the estimation is based on noise from IMU. For solving this problem Seel suggest to find the shortest distance and salehi suggest to project the point to the joint plane. Our experiments show, this optimization searching for a global minimum works optimal when both IMU sensors are moving.

☑ An IMU-based motion capture system has been developed to measure the kinematic of baseball pitcher and compute the dynamics of the full body.

We developed and validated an IMU-based motion tracking system for kinematics and kinetics measurements of human body, with a marker-based motion capture data as the reference. The method is verified and gives encouraging results. By slight improvement of some technical limitations, the method could be applicable to measure baseball pitcher motion in field. These are one step forward to the final goal of screening and direct feedback to the pitchers in baseball field for injury prevention and improving pitching performance.

This study allowed us to define a method of functional calibration with the aim of measuring baseball pitching on the field. During this research we faced various issues and problems that depends on understanding of the method and technology. Here are our recommendations for the future study:

- More advanced IMU are needed for tracking the motion of baseball pitchers.

Using the IMU that we have used in this project we were not able to track the motion of real baseball pitchers. During baseball pitching the upper limb internally rotates with an angular velocity of 4000 to 9000°/s and the hand can reach acceleration of 60G or above. The IMU that we used were able to track angular velocities up to 2000°/s and accelerations of under 16G. Therefore, to track the pitcher upper limb in the following studies there is a need to use IMU sensors with wider range of measurements.

- The error in tracking the faster motion is overall larger than the slower motions.

The fact that the results show a larger RMSD for tracking the faster motions, indicate the inertia effect. Therefore we suggest selecting a lighter IMU in the following studies.

- The method used in this project can be easily used in future studies.

IMU sensors do not measure translations and position of segments. Thus new methods need to be developed to measure the motion. Note that this project used the initial orientation of the segments from the Optitrack data. An initial calibration base can be used to set the initial orientation of IMU sensors to zero. This plate would allow the definition of a single initial coordinate system for all IMU sensors and make it possible to determine the relative orientation of the IMU sensors with respect to each other in a simple way. Using such a base the method of this project can be used easily in future studies, as follow:

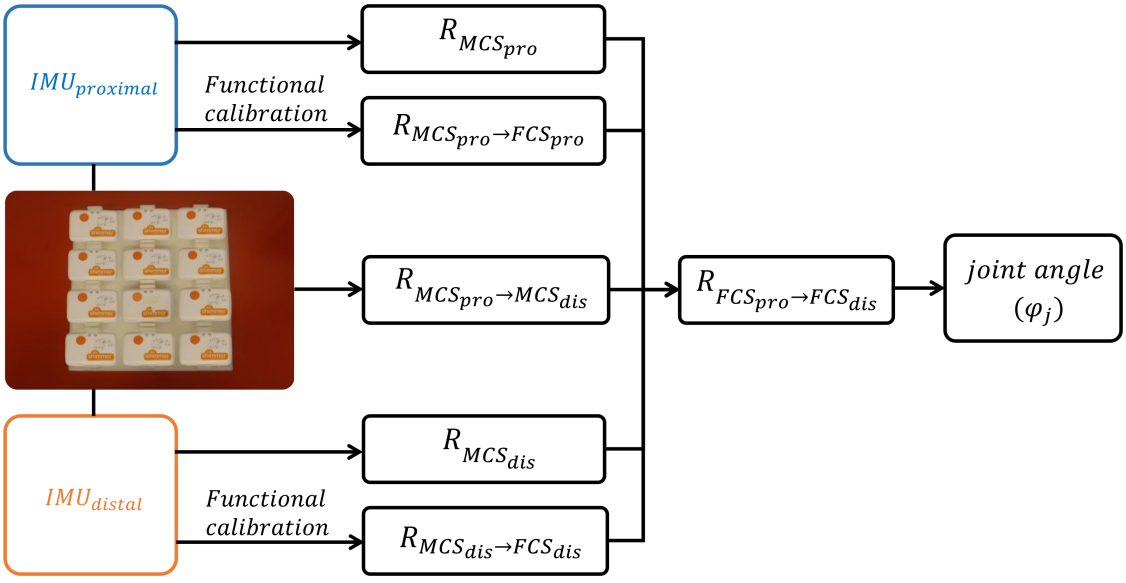

$$R_{FCS_{pro}\rightarrow FCS_{dis}} = R^{-1}_{MCS_{pro}\rightarrow FCS_{pro}} . R^{-1}_{MCS_{pro}} . R_{MCS_{pro}\rightarrow MCS_{dis}} . R_{MCS_{dis}} . R_{MCS_{dis}\rightarrow FCS_{dis}}$$

Figure 6-2 an initial calibration base to start IMU recordings and then attach the IMU sensors to the body segments. As the algorithm show, having this initial rotation known, make it possible to compute joint angle. Where, the $R_{MCS_{pro}\rightarrow MCS_{dis}}$ is the orientation of the IMU on the distal with respect to the IMU on the proximal segment. The $R_{MCS\rightarrow FCS}$ is the orientation of the IMU with respect to the segment, which is defined via functional calibration, and the R_{MCS} is the orientations of the IMU sensor recorded by IMU. Having these rotation of distal segment with respect to the proximal segment $R_{FCS_{pro}\rightarrow fCS_{dis}}$ can be defined and subsequently from that the joint angle is to be estimated.

□ Further method development is needed for estimation of linear velocities and translations.

The linear velocities and translations computed by the IMU-based method using the integration of linear acceleration recorded by the accelerometer needs to be improved.

□ Kinetic energy computation and the power flow estimation method need to be validated.

In this study only a proof on concept for kinetic computation using the IMU-based method is done. Further validation of the results of this method is needed.

 A full body power analysis in the future works is needed.

The optimal pitching mechanism needs to be yet quantified using real pitcher measurements. For the whole body power analysis, the ground reaction force and the ball and gloves masses are also need to be measured and added to the model. By quantifying the interactions between the segments of the full body model through a power analysis, the significant mechanical parameters associated to high pitching velocity can be identified.

Appendices

Appendix 1: Quaternion formulas

For a rotation matrix R, there exist a unit vector $\hat{e}$ that is unchanged by R:

$$R\hat{e} = \hat{e} \tag{62}$$

The rotation angle φ can be expressed in terms of unit vector $\hat{e}$ and the rotation matrix R:

$$\hat{e} = \begin{bmatrix} e_x \\ e_y \\ e_z \end{bmatrix} \quad \rightarrow \quad \begin{aligned} e_x &= (R_{23} - R_{32}) / (2\sin\varphi) \\ e_y &= (R_{31} - R_{13}) / (2\sin\varphi) \\ e_z &= (R_{12} - R_{21}) / (2\sin\varphi) \end{aligned} \tag{63}$$

In terms of a rotation about axis $\hat{e}$ and an angle φ, the quaternion is defined by

$$q = \begin{bmatrix} q_\omega \\ q_x \\ q_y \\ q_z \end{bmatrix} \quad \rightarrow \quad \begin{aligned} q_\omega &= \cos(\varphi / 2) \\ q_x &= e_x \sin(\varphi / 2) \\ q_y &= e_y \sin(\varphi / 2) \\ q_z &= e_z \sin(\varphi / 2) \end{aligned} \tag{64}$$

Conjugate of quaternion is defined as:

$$q = \begin{bmatrix} q_\omega & q_x & q_y & q_z \end{bmatrix}^T \quad \rightarrow \quad \overline{q} = \begin{bmatrix} q_\omega & -q_x & -q_y & -q_z \end{bmatrix}^T \tag{65}$$

Quaternion multiplication is preformed in the same manner of the multiplication of complex numbers.

$$q \otimes p = \begin{bmatrix} q_\omega \\ q_x \\ q_y \\ q_z \end{bmatrix} \otimes \begin{bmatrix} p_\omega \\ p_x \\ p_y \\ p_z \end{bmatrix} = \begin{bmatrix} p_\omega & -p_x & -p_y & -p_z \\ p_x & p_\omega & p_z & -p_y \\ p_y & -p_z & p_\omega & p_x \\ p_z & p_y & -p_x & p_\omega \end{bmatrix} \begin{bmatrix} q_\omega \\ q_x \\ q_y \\ q_z \end{bmatrix} \tag{66}$$

Going from a quaternion (q) to a rotation matrix (R) is straightforward. Rotation of a vector P=[x y z]' with the quaternion q is done by the following operation (Markley 1980):

$$\begin{aligned} q \otimes \begin{bmatrix} 0 \\ x \\ y \\ z \end{bmatrix} \otimes \overline{q} = QP\overline{Q} = \begin{bmatrix} q_\omega & -q_x & -q_y & -q_z \\ q_x & q_\omega & q_z & -q_y \\ q_y & -q_z & q_\omega & q_x \\ q_z & q_y & -q_x & q_\omega \end{bmatrix} \begin{bmatrix} q_\omega & q_x & q_y & q_z \\ -q_x & q_\omega & -q_z & q_y \\ -q_y & q_z & q_\omega & -q_x \\ -q_z & -q_y & q_x & q_\omega \end{bmatrix} \begin{bmatrix} 0 \\ x \\ y \\ z \end{bmatrix} \\ QP\overline{Q} = \begin{bmatrix} 1 & 0 & 0 & 0 \\ 0 & q_\omega^2 + q_x^2 - q_y^2 - q_z^2 & 2(-q_\omega q_z + q_x q_y) & 2(-q_\omega q_y + q_x q_z) \\ 0 & 2(q_\omega q_z + q_x q_y) & q_\omega^2 - q_x^2 + q_y^2 - q_z^2 & 2(-q_\omega q_x + q_y q_z) \\ 0 & 2(-q_\omega q_y + q_x q_z) & 2(q_\omega q_x + q_y q_z) & q_\omega^2 - q_x^2 - q_y^2 + q_z^2 \end{bmatrix} \begin{bmatrix} 0 \\ x \\ y \\ z \end{bmatrix} \end{aligned} \tag{67}$$

Further we used the Shepherd algorithm described in (Markley 2008) with a condition to avoid jumps in the quaternion signal (introduced by R. Dumas) due to a sign ambiguity in the quaternion computation.

The first derivative of the quaternion is estimated with a centred finite difference method. However, for the first frame a forward method is used and for the last frame a backward method is used:

$$\begin{aligned} &\text{Forward method:} && \frac{dq_i}{dt} \approx \frac{q_{i+1} - q_i}{2.\Delta t} \\ &\text{Centered method:} && \frac{dq_i}{dt} \approx \frac{q_{i+1} - q_{i-1}}{2.\Delta t} \\ &\text{Bacward method:} && \frac{dq_i}{dt} \approx \frac{q_i - q_{i-1}}{2.\Delta t} \end{aligned} \tag{68}$$

The 2nd derivative is also computed via a centred finite difference method as follows:

$$\frac{d^2 q_i}{dt^2} \approx \frac{q_{i+1} - 2q_i + q_{i-1}}{\Delta t^2} \tag{69}$$

Forward and backward method for the 1st and last frames lead to singularity, thus, a mirror condition is used for those frames. This condition consist in using a symmetry around the first/last frame of the signal to extrapolate i.e. $\mathbf{q}(1)$ will be the symmetry of $\mathbf{q}(3)$ around $\mathbf{q}(2)$ and $\mathbf{q}(n)$ is the symmetry of $\mathbf{q}(n\text{-}2)$ around $\mathbf{q}(n\text{-}1)$:

$$\begin{aligned} &\text{First frame:} && \frac{d^2 q_{(1)}}{dt^2} = 2.\frac{d^2 q_{(2)}}{dt^2} - \frac{d^2 q_{(3)}}{dt^2} \\ &\text{Last frame:} && \frac{d^2 q_{(n)}}{dt^2} = 2.\frac{d^2 q_{(n-1)}}{dt^2} - \frac{d^2 q_{(n-2)}}{dt^2} \end{aligned} \tag{70}$$

with *n* the number of frames.

Appendix 2: Anthropometric model

In this study, first we made a model from 15 segments as it is shown in Figure 7-1. To simplify the model, the non-throwing lower arm and hand that wears a glove, are assumed to be one segment.

1) Neck and head
2) Thorax
3) Abdomen
4) Pelvis
5) Right upper arm
6) Right lower arm
7) Right hand
8) Left upper arm
9) Left lower arm and left hand
10) Right thigh
11) Right shank
12) Right foot
13) Left thigh
14) Left shank
15) Left foot

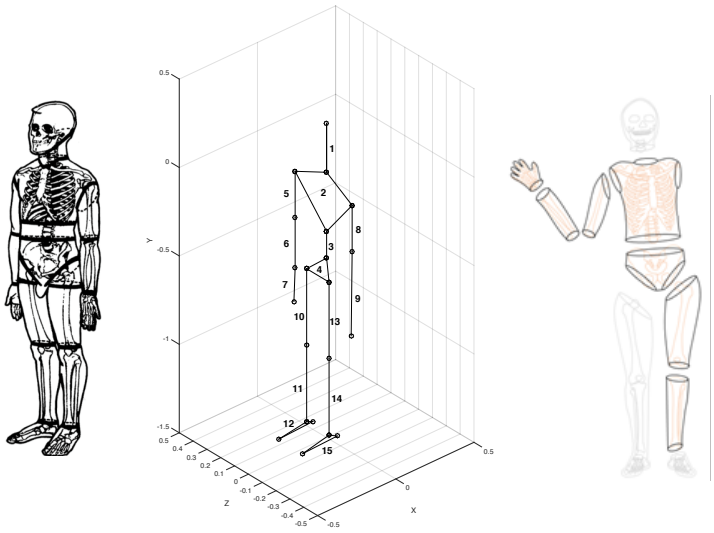

Figure 7-1 Left: Body segmentation outline (McConville, Clauser et al. 1980), middle: The model of this study body segmentation, right: measured body segments in this study.

The head is quite heavy and have some influence, but the head and neck exact movement has less effect on motion. Besides in baseball pitching, the power flow generation during pitching starts mainly from left foot and goes through body to the right hand. Therefore, for further simplification of the model we neglected the head and neck, right foot, shank, thigh and left upper arm, lower arm and hand.

Here under is the anthropometric model of Dumas et al 2007. This model is scalable and can be used to extract the mass and inertia parameters. In the original article there was a few mistakes that was corrected in contact with the writer. Therefore here I bring the whole correct parameters that could be used in the following studies.

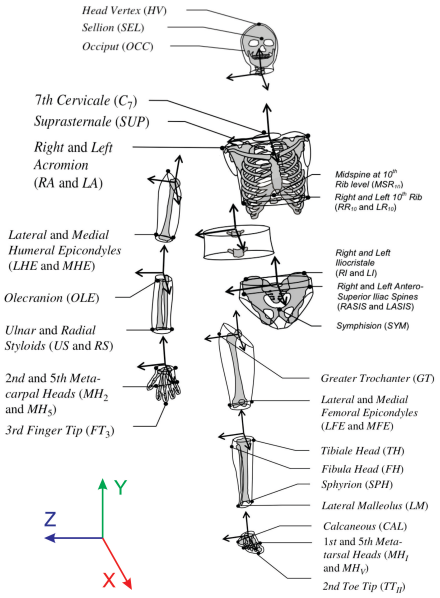

Figure 7-2 Locations of selected anatomical landmarks and orientations of the segment coordinate system (SCSs) built from these landmarks (Dumas, Chèze et al. 2007, Dumas, Cheze et al. 2007)

Table 7-1 Anatomical landmarks and centre of masses positions

Segment	Anatomical landmarks	X [m]	Y [m]	Z [m]	Length definition	Length [m]	Mass scaling factor (%)
Head and neck	1) Head Vertex (HV)	0	0.277	0	CJC to HV	0.277	6.7
	2) Sellion (SEL)	0.105	0.173	0			
	3) Occiput (OCC)	-0.073	0.1	0			
	♦ Centre of mass (COM)	-0.006	0.149	0			
Thorax	4) Suprasternale (SUP)	0.051	-0.039	0	CJC to LJC	0.334	30.4
	5) Right Acromion (RA)	-0.027	-0.045	0.206			
	6) Left Acromion (LA)	-0.027	-0.045	-0.206			
	7) 7th Cervicale (C7)	-0.072	0.026	0			
	❖ Thoracic joint centre (TJC)	0	-0.334	0			
	❖ Right Shoulder joint centre (RSJC)	0.019	0.083	0.206			
	❖ Left Shoulder joint centre (LSJC)	0.019	0.083	-0.206			
	♦ Centre of mass (COM)	0	0.185	0.001			
Abdomen	❖ Lumbar joint centre (LJC)	0	-0.151	0	TJC to LJC	0.151	2.9
	♦ Centre of mass (COM)	0.026	-0.055	0			
Pelvis	8) Right Anterior Superior Iliac Spine (RASIS)	0.078	0.007	0.112	Length: LJC to projection of HJC in sagittal plane Width: RASIS to LASIS	Length: 0.0936 Width: 0.224	14.6
	9) Left Anterior Superior Iliac Spine (LASIS)	0.078	0.007	-0.112			
	❖ Right Hip joint centre (RHJC)	0.056	-0.075	0.81			
	❖ Left Hip joint centre (LHJC)	0.056	-0.075	-0.81			
	10,11) Middle of Right and left Posterior Superior Iliac Spine (RPSIS and LPSIS)	-0.102	0.007	0			
	♦ Centre of mass (COM)	0.003	-0.026	0			
Right upper arm	5) Right Acromion (RA)	-0.025	0.054	0.003	SJC to EJC	0.261	2.4
	12) Right Lateral Humeral Epicondyle (RLHE)	0	-0.258	0.041			
	13) Right Medial Humeral Epicondyle (RMHE)	0	-0.264	-0.041			
	❖ Right Elbow joint centre (REJC)	0	-0.261	0			
	♦ Centre of mass (COM)	0.005	-0.118	-0.007			
Right lower arm	14) Right Ulnar Styloid Process (RUS)	0	-0.284	-0.033	EJC to WJC	0.284	1.7
	15) Right Radial Styloid Process (RRS)	0	-0.284	0.033			
	❖ Right Wrist joint centre (RWJC)	0	-0.284	0			
	♦ Centre of mass (COM)	0.003	-0.118	0.004			
Right hand	14) Right Ulnar Styloid Process (RUS)	-0.007	0	-0.032	WJC to FT3	0.1891	0.6
	15) Right Radial Styloid Process (RRS)	0.007	0	0.032			
	16) Right Hand 2nd Metacarpal Head (RMH2)	0	-0.086	0.046			
	17) Right Hand 5th Metacarpal Head (RMH5)	0	-0.075	-0.046			
	18) Right Hand 3rd finger middle phalanges (RFMP3)	0.007	-0.189	0.001			
	♦ Centre of mass (COM)	0.007	-0.068	0.006			
Left upper arm	6) Left Acromion (LA)	-0.025	0.054	-0.003	SJC to EJC	0.261	2.4
	19) Left Lateral Humeral Epicondyle (LLHE)	0	-0.258	-0.041			
	20) Left Medial Humeral Epicondyle (LMHE)	0	-0.264	0.041			
	❖ Left Elbow joint centre (LEJC)	0	-0.261	0			
	♦ Centre of mass (COM)	0.005	-0.118	0.007			
Left lower arm & left hand	21) Left Ulnar Styloid Process (LUS)	0	-0.284	0.033	EJC to FT3	0.4731	2.3
	22) Left Radial Styloid Process (LRS)	0	-0.284	-0.033			
	23) Left Hand 3rd finger middle phalanges (LFMP3)	0.007	-0.473	-0.001			
	❖ Right Wrist joint centre (RWJC)	0	-0.284	0			
	♦ Centre of mass (COM)	0.004	-0.179	-0.0045			
Right thigh	24) Right Greater Trochanter (RGT)	-0.040	0.006	0.101	HJC to KJC	0.4315	12.3
	25) Right Lateral Femoral Epicondyles (RLFE)	0	-0.431	0.057			
	26) Right Medial Femoral Epicondyles (RMFE)	0	-0.432	-0.057			
	❖ Right Knee joint centre (RKJC)	0	-0.4315	0			
	♦ Centre of mass (COM)	-0.018	-0.185	0.0142			
Right shank	27) Right Fibula Head (RFH)	0	-0.023	0.047	KJC to AJC	0.4335	4.8
	28) Right Shyrion (RSPH)	0.021	-0.434	-0.033			
	29) Right Lateral Malleous (RLM)	-0.021	-0.433	0.033			
	❖ Right Ankle Joint Centre (RAJC)	0	-0.4335	0			
	♦ Centre of mass (COM)	-0.021	-0.178	0.003			
Right foot	30) Right Calcaneous (RCAL)	-0.046	-0.021	0.007	AJC to midpoint MHI and MHV	0.1388	1.2
	31) Right Foot 1th Metatarsal Head (RMH1)	0.146	-0.021	-0.047			
	32) Right Foot 5th Metatarsal Head (RMH5)	0.128	-0.021	0.060			
Left thigh	33) Left Greater Trochanter (LGT)	-0.040	0.006	-0.101	HJC to KJC	0.4315	12.3
	34) Left Lateral Femoral Epicondyles (LLFE)	0	-0.431	-0.057			
	35) Left Medial Femoral Epicondyles (LMFE)	0	-0.432	0.057			
	❖ Left Knee joint centre (LKJC)	0	-0.4315	0			
	♦ Centre of mass (COM)	-0.018	-0.185	-0.0142			
Left shank	36) Left Fibula Head (LFH)	0	-0.023	-0.047	KJC to AJC	0.4335	4.8
	37) Left Shyrion (LSPH)	0.021	-0.434	0.033			
	38) Left Lateral Malleous (LLM)	-0.021	-0.433	-0.033			
	❖ Right Ankle Joint Centre (RAJC)	0	-0.4335	0			
	♦ Centre of mass (COM)	-0.021	-0.178	-0.003			
Left foot	39) Left Calcaneous (LCAL)	-0.046	-0.021	-0.007	AJC to midpoint MHI and MHV	0.1388	1.2
	40) Left Foot 1th Metatarsal Head (LMH1)	0.146	-0.021	0.047			
	41) Left Foot 5th Metatarsal Head (LMH5)	0.128	-0.021	-0.060			

❖ Joint centres are estimated based on the location of specific markers

♦ Centre of masses are estimated based on scaling vector of position of centre of masses From (Dumas, Cheze et al. 2007)

Appendix 3: Description of the Optitrack system

1. Specifications

USB Modes Supported	USB2.0: High-Speed (480Mbps), Full-Speed (12Mbps), Low-Speed (1.5Mbps)
USB Ports	Uplink: 1 Downlink: 6
Power Input	OptiHub 1 : 12V @ 3.0A OptiHub 2 : 12V @ 3.8A
Power Output	OptiHub 1 : 3.5W (700mA @ 5V) max per port OptiHub 2 : 5.0W (1000mA @ 5V) max per port
Status LEDs	• Power • Uplink Port Status • Downlink Port Status • Sync Activity
Sync Input Sources	1. Internally Generated 2. Cascaded OptiHub Output 3. External Digital Input 4. Software Trigger (from PC via USB)
External Sync Input	Opto-isolated Input, (LV)TTL compatible V_{il}(max) : 0.8V V_{ih}(min) : 2.5V V_{ih}(max) : 13V Max Freq : 10kHz
External Sync Output	LV-TTL Digital Output
External Sync Output Types	1. Exposure Pulse 2. External Sync Input Pass-Through
	3. Recording Active – Level Output 4. Recording Active – Frame Pulse
External Sync Output Polarity	Normal or Reverse
External Sync Input Divider	1:1 – 1:15
External Sync Input Trigger Modes	1. Rising-Edge 2. Falling-Edge 3. Either-Edge 4. High-Level Gated 5. Low-Level Gated
External Sync Input Trigger Delay	0 – 65ms
Internally Generated Trigger Rate	8 – 100 Hz
OptiTrack™ Camera Sync Modes	1. OptiSync (sync signaling is carried using out-of-band signaling on the power conductors of standard USB cables) 2. WiredSync (dedicated camera-to-camera daisy-chain cables provided by NaturalPoint)
Compatible Stereo-Vision Systems	1. Stereographics CrystalEyes ™ 2. NuVision 60GX 3. NuVision APG6000 Refresh Rates: 60/90/96/100/120/200 FPS

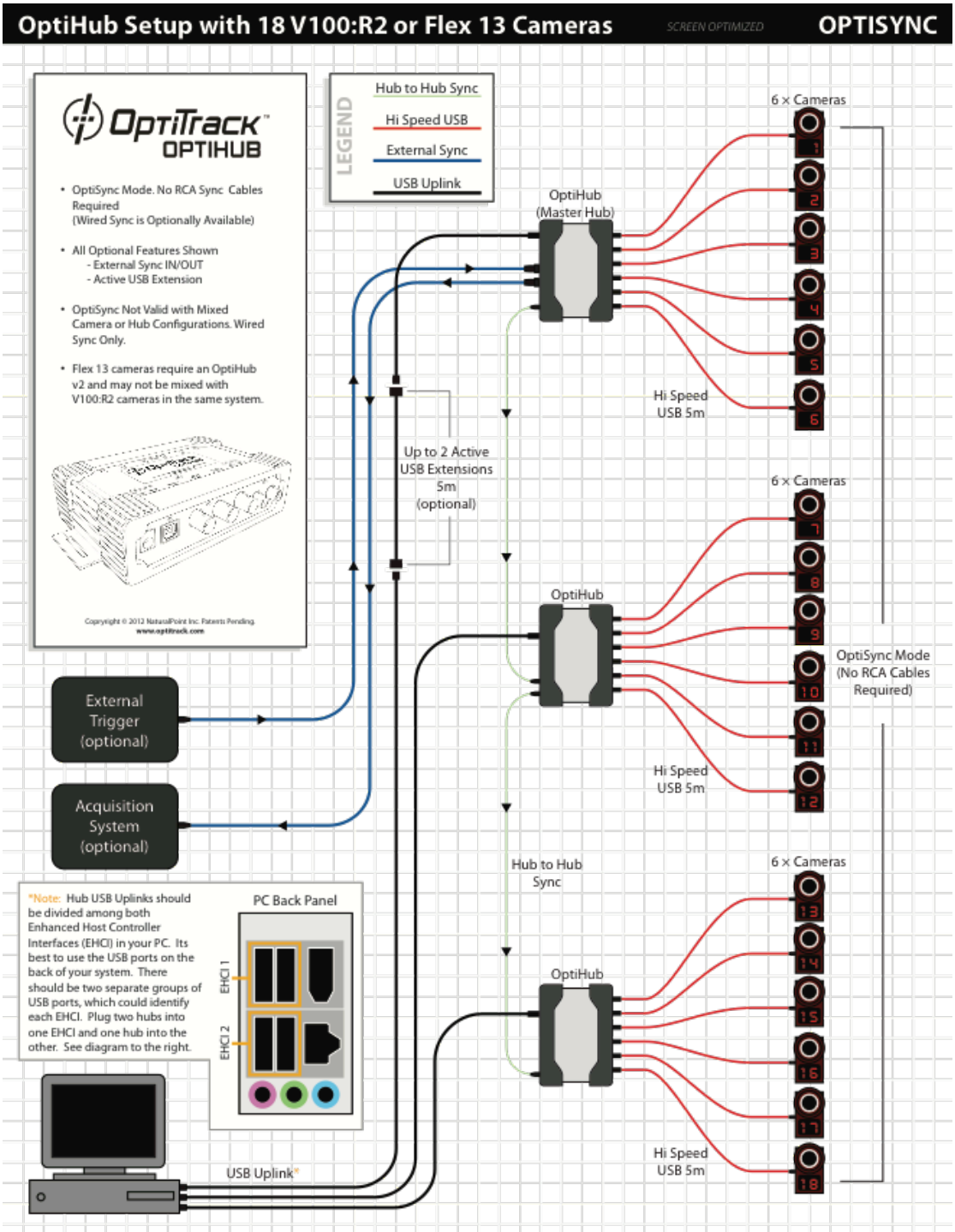
OptiHub Setup with 18 V100:R2 or Flex 13 Cameras
SCREEN OPTIMIZED
OPTISYNC
OptiTrack
OPTIHUB
• OptiSync Mode. No RCA Sync Cables Required (Wired Sync is Optionally Available)
• All Optional Features Shown
- External Sync IN/OUT
- Active USB Extension
• OptiSync Not Valid with Mixed Camera or Hub Configurations. Wired Sync Only.
• Flex 13 cameras require an OptiHub v2 and may not be mixed with V100:R2 cameras in the same system.
Copyright © 2012 NaturalPoint Inc. Patents Pending.
www.optitrack.com
LEGEND
Hub to Hub Sync
Hi Speed USB
External Sync
USB Uplink
6 × Cameras
OptiHub (Master Hub)
Hi Speed USB 5m
Up to 2 Active USB Extensions 5m (optional)
6 × Cameras
OptiHub
OptiSync Mode (No RCA Cables Required)
Hi Speed USB 5m
External Trigger (optional)
Acquisition System (optional)
Hub to Hub Sync
6 × Cameras
OptiHub
Hi Speed USB 5m
*Note: Hub USB Uplinks should be divided among both Enhanced Host Controller Interfaces (EHCI) in your PC. Its best to use the USB ports on the back of your system. There should be two separate groups of USB ports, which could identify each EHCI. Plug two hubs into one EHCI and one hub into the other. See diagram to the right.
PC Back Panel
EHCI 1
EHCI 2
USB Uplink*

FLEX 13

TECHNICAL SPECIFICATIONS

CAMERA BODY

- Width: 2.12 inches (53.8 mm)
- Height: 3.19 inches (81 mm)
- Depth: 1.67 inches (42.4 mm)
- Weight: 6.60 ounces (187 g)
- Mounting: 1/4"-20 tripod thread
- Status Indicators:
  - 2 digit numeric LEDs
  - 1 bicolor status LED

IMAGE SENSOR

- Pixel Size : 4.8 µm × 4.8 µm
- Imager Size : 6.144 mm × 4.9152 mm
- Imager Resolution : 1280 × 1024 (1.3 MP)
- Frame Rate: 30-120 FPS (adjustable)
- Accuracy: Sub-millimeter
- Latency: 8.3 ms
- Shutter Type: Global
- Shutter Speed:
  - Default: 500 µs
  - Minimum: 20 µs
  - Maximum: 7.5 ms (at 120 FPS)

IMAGE PROCESSING TYPES

- Object (Centroids)
- Precision (Grayscale)
- Segment (Thresholded)
- MJPEG Grayscale
- Raw Grayscale

LENS & FILTER

- Default Lens: 5.5mm F#1.8
  - Horizontal FOV: 56°
  - Vertical FOV: 46°
- Optional Lens: 8 mm F#1.8
  - Horizontal FOV: 42°
  - Vertical FOV: 34°
- M12 Lens Mount
- Adjustable focus w/ spring assist
- 800 nm IR pass filter
- Optional: 800nm IR pass filter w/ Filter Switcher

LED RING

- 28 LEDs
- 850 nm IR
- Adjustable brightness
- Strobe or Continuous Illumination
- Removable

INPUT/OUTPUT & POWER

- Data: USB 2.0
- Camera Sync: USB 2.0 (via OptiSync)
- Power: USB 2.0 @ 1A

SYSTEM REQUIREMENTS

- Windows XP/Vista/7
- 1GHz processor
- 1GB of RAM
- 50MB of available disk space
- USB 2.0 Hi-speed port
- OptiHub 2 (required for IR LED power)

IN THE BOX

- 1 Flex 13 camera (part number: FL-13)
- 1 Quick Start guide

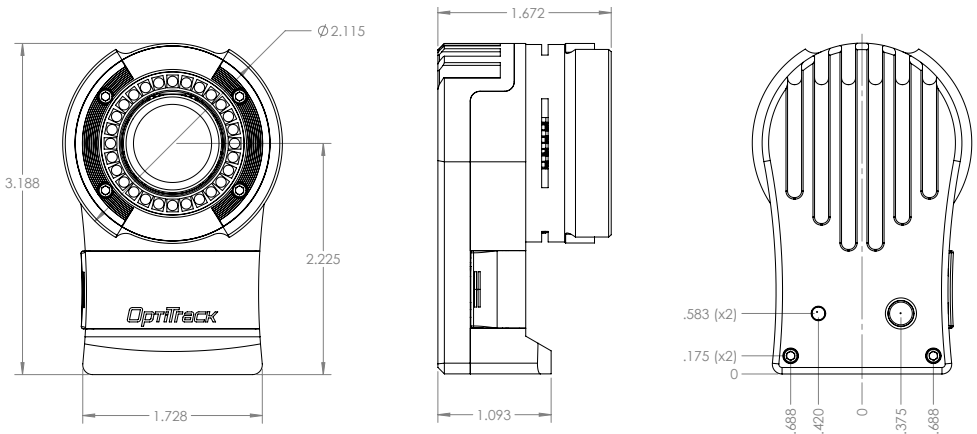

P: +1-888-865-5535 • www.optitrack.com • support@naturalpoint.com • sales@naturalpoint.com

Appendix 4: Description of the Shimmer3

Shimmer3
Wireless Sensor Platform

shimmer
DISCOVERY IN MOTION

INTRODUCTION

Shimmer3 is the smallest, slimmest and most robust wearable wireless sensor created by Shimmer to date. The module boasts a 24MHz CPU with a precision clock subsystem, making it three times faster than its predecessor, Shimmer2r

PRODUCT OVERVIEW

In developing Shimmer3, we have focussed on creating a powerful and elegant wearable wireless sensor which will provide superior data quality, adding value to your data collection process. We've created a smarter enclosure which allows for straps to be quickly clicked into place for a range of wearable applications.

Shimmer3 offers best data quality with integrated 9 DoF inertial sensing via accel, gyro, mag and altimeter, each with selectable range. Shimmer3 also boasts an integrated motion processor for on-board 3D orientation estimation. 5 coloured LEDs indicate device status and operating mode, as well as indicating Bluetooth streaming functionality.

For existing customers, Shimmer3 modules are backward compatible with the Shimmer2r Dock and Multi Charger. All current development tools and enabling applications are compatible with the Shimmer3 platform.

KEY FEATURES

- Very low power consumption, light weight, and small form factor
- Slide-switch for powering on/off
- Readily connects via Bluetooth or local storage via a microSD card
- SD data bypass
- 24MHz MSP430 CPU
- Internal and External connectors for expansion (Expansion modules include ECG, EMG, GSR+, and others)
- Best data quality - Integrated 10 DoF inertial sensing via accelerometer, gyroscope, magnetometer, and altimeter, each with selectable range
- Two accelerometers give choice between ultra-low noise or wide range
- Integrated motion processor for on-board 3D orientation estimation
- 5 coloured LEDs across 2 locations to indicate device status and operating mode
- Integrated Li-ion battery management
- JTAG debugging mode available
- Expansion header for alternative radio

APPLICATIONS

Shimmer is designed for wearable and remote sensing applications. The Shimmer unit is designed to be highly flexible and adaptable, easily integrating into existing systems and technologies. Shimmer is frequently used in activity monitoring, sport science, and intelligent building applications to name but a small few. Due to is flexibility, the Shimmer platform is generally application agnostic. Shimmer is currently used in the following areas:

- Human Health Monitoring
- Activities of Daily Living
- Connected Health Solutions
- Sports Science
- Structural Monitoring
- Intelligent Buildings
- Environmental and Habitat Monitoring

www.ShimmerSensing.com info@ShimmerSensing.com

Shimmer3
Wireless Sensor Platform

shimmer
DISCOVERY IN MOTION

TECHNICAL SPECIFICATIONS	
Microcontroller	**TI MSP430**
A/D Resolution	11 Channels of 12-bit A/D: 7 free for expansion
RAM	16KB
Flash	256KB
Frequency	24MHz
Wide Range Accel.	**STMicro LSM303DLHC**
Range	±2g, ±4g, ±8g, ±16g
Sensitivity	1000 LSB/g at +/-2g
Numeric Resolution	16-bit
Typical Operating Current	110 µA (Running Mag @ 7.5 Hz & Accel @ 50 Hz)
RMS Noise*	27.5 x 10^{-3} m/s²
Low Noise Accel.	**Kionix KXRB5-2042**
Range	±2g
Sensitivity	600 ±18 mV/g
Typical Operating Current	500 µA
RMS Noise*	5.09 x 10^{-3} m/s²
Digital Mag	**STMicro LSM303DLHC**
Range	±1.3; ±1.9; ±2.5; ±4.0; ±4.7; ±5.6; ±8.1 Ga
Sensitivity	1100 LSB/Ga at ±1.3
Numeric Resolution	16-bit
RMS Noise*	0.0081 normalised local flux
Gyro	**Invensense MPU9150**
Range	±250; ±500; ±1000; ±2000 dps
Sensitivity	131 LSB/dps at ±250
Numeric Resolution	16-bit
Typical Operating Current	3.5 mA
RMS Noise*	0.0481 dps
Pressure Sensor	**Bosch BMP180**
Range	300 - 1100 hPa
Numeric Resolution	16-bit
Typical Operating Current	1 µA at 1 Hz
RMS Noise (Standard mode)	0.4 m (from Datasheet)

*@ 100Hz Bandwidth

SHIMMER3 ROADMAP	
Shimmer3 Platform	Now Available
Biophysical	ECG, EMG, & GSR + Heart Rate: Now Available
Expansions	PROTO3 Mini Expansion board and PROTO3 Deluxe Expansion board: Now Available Strain Guage Amplifier: Now Available
Weight	23.6 Grams

SUPPORTING SOFTWARE
Shimmer ConsensysPRO & ConsensysBASIC Software
ShimmerCapture for Android
Shimmer 9DoF Calibration for Android
Shimmer LabVIEW Instrument Driver
Shimmer MATLAB Instrument Driver
Shimmer Java/Android API
Shimmer C# API
Multi Shimmer Sync for Android

CLASS LEADING WEARABLE WIRELESS SENSING
Dimensions: 51mm x 34mm x 14mm
Improved straps and quick snap clips provide full mobility, unrestricted movement and comfort for the wearer
Highly flexible and adaptable sensor platform can be applied to specific end user requirements
Highly accurate and scientifically reliable raw or calibrated data offers complete control over capture and interpretation of signals in real-time

CONTACT US

Shimmer
Dublin, Ireland
Boston, USA

E: info@ShimmerSensing.com
W: www.ShimmerSensing.com

Appendix 5: Description of Xsens suit

XSENS

XSENS MVN BIOMECH IS THE NUMBER ONE CHOICE FOR MEASURING 3D KINEMATICS EVERYWHERE, UNDER ANY CIRCUMSTANCE. THE MINIATURE MOTION TRACKERS DEVELOPED BY XSENS ARE ABLE TO CAPTURE FROM THE SLIGHTEST TWITCHES TO HIGH DYNAMICS. XSENS' PROVEN BIOMECHANICAL MODEL AND SENSOR FUSION ALGORITHMS ENSURE THE HIGHEST QUALITY MOTION ANALYSIS, EVEN IN CHALLENGING ENVIRONMENTS.

MVN BIOMECH HIGHLIGHTS

Ease of use
- Small robust trackers
- Quick and easy setup
- Intuitive software
- Miniature trackers worn over or under clothing

Accurate real-time data. Effortlessly
- 3D character visualization
- 3D kinematic graphs
- Patented signal pipelines
- No post processing, instant export

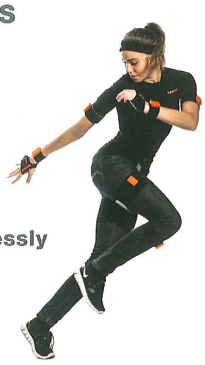

Robust and reliable
- Superior algorithms ensure measurements in any condition, including magnetic disturbances
- < 10µs inter-tracker time synchronization essential for accurate joint angles

Integration
- Easy sync with 3rd party devices
- Data streamed or imported to many digital environments
- Works with Siemens PLM Software, Dassault Delmia & Catia, Unity3D, Autodesk

MVN STUDIO BIOMECH SOFTWARE (MVN STUDIO BIOMECH)

Features
- Intuitive software interface
- Calibration routines
- Scalable biomechanical model
- Record and playback
- Sync setup
- Supports up to 4 hardware setups
- Real-time 3D view, graphs and video

Output
- Joint angles
- Segment kinematics
- Segment global positions
- Body center of mass
- Sensor data

Export formats
- ASCII (XML)
- C3D
- BVH, FBX
- Movie (AVI, M4V)

MVN Studio BIOMECH graphs

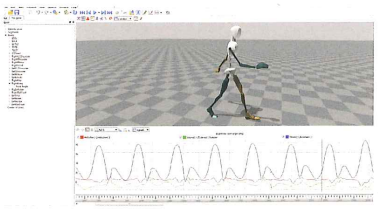

MVN Studio BIOMECH reference camera

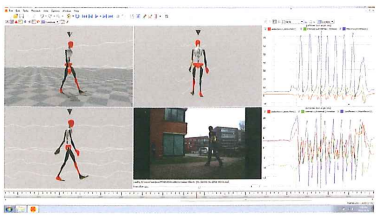

MVN BIOMECH Hardware

	MVN BIOMECH Awinda	MVN BIOMECH Link
	Completely wireless, extremely lightweight. Ideal for subject interchangeability	High update rate. Ideal for high dynamic movement tracking
System contents	• MVN Studio BIOMECH license • 17 wireless motion trackers (MTw) • 1 spare/prop MTw • Full-body set of straps (incl. M/L/XL T-shirt) • Awinda Station (for data transmission, docking and sync) • Awinda Dongle • MVN Ethernet Camera • Transport backpack	• MVN Studio BIOMECH license • 17 motion trackers (MTx) • 1 spare/prop MTx • 1 Lycra suit (incl. shorts) (size options: S/M/L/XL/XXL) • Body Pack • WiFi Access Point • Sync Station • MVN Ethernet Camera • Transport suitcase
Trackers	Wireless motion trackers	Wired motion trackers
Tracker placement	Easy fastening with Velcro straps	Tight and secure fastening in Lycra suit
Internal update rate	1000 Hz	1000 Hz
Update rate	60 Hz	240 Hz
Latency	30 ms	20 ms
Buffer time (retransmissions)	10 s	120 s
Battery life	6 Hours	10 Hours
Dimensions		
Motion trackers	47 x 30 x 13 mm (20 g)	36 x 24.5 x 10mm (10 g)
Body pack	N/A	160 x 72.5 x 25 mm (150 g)
Battery	N/A	94.7 x 58.5 x 25 mm (70 g)
Communication		
Range open space	Up to 50 m	Up to 150 m
Range office space	Up to 20 m	Up to 50 m
Wireless protocol	Xsens patented Awinda protocol	WiFi 2 and 5 GHz (subject to PC)
Receiver	Awinda Station / Awinda Dongle	WiFi Access Point

MVN BIOMECH Motion Tracker Performance

Orientation	
Static accuracy (Roll/Pitch)	0.2 deg
Static Accuracy (Heading)	0.5 deg
Dynamic Accuracy	1 deg RMS

Tracker components			
	Angular velocity	**Acceleration**	**Magnetic field**
Dimensions	3 axes	3 axes	3 axes
Full scale	± 2000 deg/s	± 160 m/s2	± 1.9 Gauss

Appendix 6: Description of Analog devices IMU

ANALOG DEVICES

Fast Starting, ±20,000°/sec Vibration Rejecting Rate Gyro

Data Sheet **ADXRS649**

FEATURES

High vibration rejection over wide frequency
Ultrafast startup: 3 ms
Measurement range extendable to ±50,000°/sec
10,000 *g* powered shock survivability
Ratiometric to referenced supply
5 V single-supply operation
Z-axis (yaw rate) response
−40°C to +105°C operation
Self-test on digital command
Ultrasmall and light (<0.15 cc, <0.5 gram)
Temperature sensor output
RoHS compliant

APPLICATIONS

Sports equipment
Industrial applications
Platform stabilization
High speed tachometry

GENERAL DESCRIPTION

The ADXRS649 is a complete angular rate sensor (gyroscope) that uses the Analog Devices, Inc., patented high volume BiMOS surface-micromachining process to make a complete gyro on one chip. An advanced, differential, quad sensor design rejects the influence of linear acceleration, enabling the ADXRS649 to offer rate sensing in harsh environments where shock and vibration are present.

The output signal, RATEOUT (B1, A2), is a voltage proportional to the angular rate about the axis normal to the top surface of the package. The output is ratiometric with respect to a provided reference supply. An external capacitor is used to set the bandwidth. The measurement range is extendable to ±50,000°/sec by adding an external resistor.

Low power consumption (3.5 mA) enables very low power consumption, and ultrafast startup (3 ms) allows for quick power cycling of the gyro. At 10 samples per second, a pair of CR2032 coin cells can power the ADXRS649 for three months.

A temperature output is provided for compensation techniques. Two digital self-test inputs electromechanically excite the sensor to test proper operation of both the sensor and the signal conditioning circuits. The ADXRS649 is available in a 7 mm × 7 mm × 3 mm CBGA chip scale package.

FUNCTIONAL BLOCK DIAGRAM

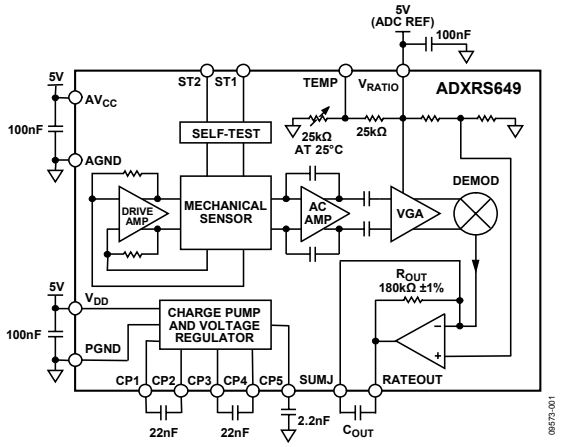

Figure 1.

Rev. B Document Feedback

One Technology Way, P.O. Box 9106, Norwood, MA 02062-9106, U.S.A.
Tel: 781.329.4700
Technical Support www.analog.com

SPECIFICATIONS

All minimum and maximum specifications are guaranteed. Typical specifications are not guaranteed.

T_A = −40°C to +105°C, $V_S = AV_{CC} = V_{DD} = V_{RATIO}$ = 5 V, angular rate = 0°/sec, bandwidth = 80 Hz (C_{OUT} = 0.33 µF), I_{OUT} = 100 µA, ±1 g, unless otherwise noted.

Parameter	Test Conditions/Comments	Min	Typ	Max	Unit
SENSITIVITY[1]	Clockwise rotation is positive output				
Measurement Range[2]	Full-scale range over specifications range	±300	±320		°/sec
Initial and over Temperature	−40°C to +105°C	0.1	0.12	0.14	mV/°/sec
Temperature Drift[3]			±2		%
Nonlinearity	Best fit straight line, 25°C		0.1		% of FS
NULL, BITS[1]					
Null Bias	−40°C to +105°C	2.4	2.5	2.6	V
Linear Acceleration Effect	Any axis		0.1		°/sec/g
Vibration Rectification	40 g rms, 50 Hz to 27 kHz		0.0006		°/sec/g^2
NOISE PERFORMANCE					
Rate Noise Density	T_A = 25°C		0.25		°/sec/√Hz
	T_A = 105°C		0.4		°/sec/√Hz
Resolution Floor	T_A = 25°C, 1 minute to 1 hour in-run		200		°/hr
FREQUENCY RESPONSE					
Bandwidth	±3 dB user adjustable up to specification		2000		Hz
Sensor Resonant Frequency		15.5	17.5	20	kHz
SELF-TEST					
ST1 RATEOUT Response	ST1 pin from Logic 0 to Logic 1		−1300		°/sec
ST2 RATEOUT Response	ST2 pin from Logic 0 to Logic 1		1300		°/sec
ST1 to ST2 Mismatch[5]			±2		%
Logic 1 Input Voltage		3.3			V
Logic 0 Input Voltage				1.7	V
Input Impedance	To common	40	50	100	kΩ
TEMPERATURE SENSOR[1]					
V_{OUT} at 25°C	Load = 10 MΩ	2.3	2.4	2.5	V
Scale Factor[6]	T_A = 25°C, V_{RATIO} = 5 V		9		mV/°C
Load to V_S			25		kΩ
Load to Common			25		kΩ
TURN-ON TIME[7]	Power on to ±90% of final output, CP5 = 2.2 nF		3		ms
OUTPUT DRIVE CAPABILITY					
Current Drive	For rated specifications			200	µA
Capacitive Load Drive				1000	pF
POWER SUPPLY					
Operating Voltage (V_S)		4.75	5.00	5.25	V
Quiescent Supply Current			3.5		mA
TEMPERATURE RANGE					
Specified Performance		−40		+105	°C

[1] Parameter is linearly ratiometric with V_{RATIO}.
[2] Measurement range is the maximum range possible, including output swing range, initial offset, sensitivity, offset drift, and sensitivity drift at 5 V supplies.
[3] From +25°C to −40°C or +25°C to +105°C.
[4] Adjusted by external capacitor, C_{OUT}. Reducing bandwidth below 0.01 Hz does not result in further noise improvement.
[5] Self-test mismatch is described as (ST2 + ST1)/((ST2 − ST1)/2).
[6] Scale factor for a change in temperature from 25°C to 26°C. V_{TEMP} is ratiometric to V_{RATIO}. See the Temperature Output and Calibration section for more information.
[7] Based on characterization.

ABSOLUTE MAXIMUM RATINGS

Table 2.

Parameter	Rating
Acceleration (Any Axis, 0.5 ms)	
Unpowered	10,000 g
Powered	10,000 g
V_{DD}, AV_{CC}	−0.3 V to +6.0 V
V_{RATIO}	AV_{CC}
ST1, ST2	AV_{CC}
Output Short-Circuit Duration (Any Pin to Common)	Indefinite
Operating Temperature Range	−55°C to +125°C
Storage Temperature Range	−65°C to +150°C

Stresses above those listed under the Absolute Maximum Ratings may cause permanent damage to the device. This is a stress rating only; functional operation of the device at these or any other conditions above those indicated in the operational section of this specification is not implied. Exposure to absolute maximum rating conditions for extended periods may affect device reliability.

Drops onto hard surfaces can cause shocks of greater than 10,000 g and can exceed the absolute maximum rating of the device. Care should be exercised in handling to avoid damage.

RATE SENSITIVE AXIS

The ADXRS649 is a z-axis rate-sensing device (also called a yaw rate-sensing device). It produces a positive going output voltage for clockwise rotation about the axis normal to the package top, that is, clockwise when looking down at the package lid.

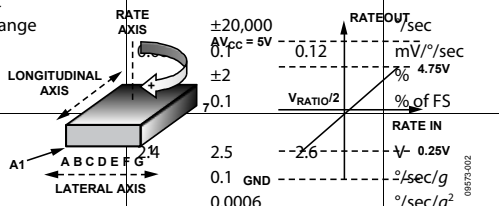

Figure 2. RATEOUT Signal Increases with Clockwise Rotation

ESD CAUTION

ESD (electrostatic discharge) sensitive device. Charged devices and circuit boards can discharge without detection. Although this product features patented or proprietary protection circuitry, damage may occur on devices subjected to high energy ESD. Therefore, proper ESD precautions should be taken to avoid performance degradation or loss of functionality.

References

Lapinski Ackland, D., F. Keynejad and M. Pandy (2011). "Future trends in the use of X-ray fluoroscopy for the measurement and modelling of joint motion." Proceedings of the Institution of Mechanical Engineers, Part H: Journal of Engineering in Medicine.

Ahmadi, A., D. D. Rowlands and D. A. James (2010). "Development of inertial and novel marker-based techniques and analysis for upper arm rotational velocity measurements in tennis." Sports Engineering **12**(4): 179-188.

Arroyo, B. (2015). "cover's pictures are from the Curveball pitch." from https://www.dylancoulter.com/Anatomy-of-a-Pitch/1/thumbs/.

Arthur, R. (2015, March 27). "At least all these Tommy john surgeries aren't rotator cuff surgeries." Retrieved 2017-07-30, from https://fivethirtyeight.com/features/at-least-all-these-tommy-john-surgeries-arent-rotator-cuff-surgeries/.

Bajd, T., M. Mihelj, J. Lenarčič, A. Stanovnik and M. Munih (2010). Homogenous transformation matrices. Robotics, Springer**:** 9-22.

Cavallo, A., A. Cirillo, P. Cirillo, G. De Maria, P. Falco, C. Natale and S. Pirozzi (2014). "Experimental comparison of sensor fusion algorithms for attitude estimation." IFAC Proceedings Volumes **47**(3): 7585-7591.

Chen, X. (2013). Human motion analysis with wearable inertial sensors PHD, University of Tennessee.

Cherveny, P. (2015, February 18). "Optical Motion Capture." System technologies: Motion tracking Retrieved 2017-07-30, from http://bestperformancegroup.com/?page_id=31.

Cloete, T. and C. Scheffer (2008). Benchmarking of a full-body inertial motion capture system for clinical gait analysis. Engineering in Medicine and Biology Society, 2008. EMBS 2008. 30th Annual International Conference of the IEEE, IEEE.

Deblonde, A. (2011). Inertial and Video Data Integration. Master of Science in Engineering, KTH, School of Computer Science and Communication (CSC).

Desroches, G., R. Dumas, D. Pradon, P. Vaslin, F.-X. Lepoutre and L. Chèze (2010). "Upper limb joint dynamics during manual wheelchair propulsion." Clinical Biomechanics **25**(4): 299-306.

Dirkx, D. (2011). Continuous Shape Optimization of Entry Vehicles MSc thesis, Delft University of Technology, (Unpublished).

Dumas, R., R. Aissaoui, D. Mitton, W. Skalli and J. A. d. Guise (2005). "Personalized body segment parameters from biplanar low-dose radiography." IEEE Transactions on Biomedical Engineering **52**(10): 1756-1763.

Dumas, R., L. Chèze and J.-P. Verriest (2007). "Corrigendum to "Adjustments to McConville et al. and Young et al. body segment inertial parameters"[J. Biomech. 40 (2007) 543–553]." Journal of Biomechanics **40**(7): 1651-1652.

Dumas, R., L. Cheze and J. P. Verriest (2007). "Adjustments to McConville et al. and Young et al. body segment inertial parameters." J Biomech **40**(3): 543-553.

Favre, J., R. Aissaoui, B. M. Jolles, J. A. de Guise and K. Aminian (2009). "Functional calibration procedure for 3D knee joint angle description using inertial sensors." Journal of Biomechanics **42**(14): 2330-2335.

Favre, J., B. M. Jolles, R. Aissaoui and K. Aminian (2008). "Ambulatory measurement of 3D knee joint angle." Journal of Biomechanics **41**(5): 1029-1035.

Favre, J., F. Luthi, B. Jolles, O. Siegrist, B. Najafi and K. Aminian (2006). "A new ambulatory system for comparative evaluation of the three-dimensional knee kinematics, applied to anterior cruciate ligament injuries." Knee Surgery, Sports Traumatology, Arthroscopy **14**(7): 592-604.

Fiorentino, N. M., M. J. Kutschke, P. R. Atkins, K. B. Foreman, A. L. Kapron and A. E. Anderson (2016). "Accuracy of functional and predictive methods to calculate the hip joint center in young non-pathologic asymptomatic adults with dual fluoroscopy as a reference standard." Annals of biomedical engineering **44**(7): 2168-2180.

Kim, S. J. and B. K. Kim (2013). "Dynamic ultrasonic hybrid localization system for indoor mobile robots." IEEE Transactions on Industrial Electronics **60**(10): 4562-4573.

Knudson, D. (2007). Fundamentals of biomechanics, Springer Science & Business Media.

Lafortune, M., P. R. Cavanagh, H. Sommer and A. Kalenak (1992). "Three-dimensional kinematics of the human knee during walking." Journal of biomechanics **25**(4): 347-357.

Lai, D. T., E. Charry, R. Begg and M. Palaniswami (2008). A prototype wireless inertial-sensing device for measuring toe clearance. 2008 30th Annual International Conference of the IEEE Engineering in Medicine and Biology Society, IEEE.

Lapinski, M., E. Berkson, T. Gill, M. Reinold and J. A. Paradiso (2009). A distributed wearable, wireless sensor system for evaluating professional baseball pitchers and batters. Wearable Computers, 2009. ISWC'09. International Symposium on, IEEE.

Lapinski, M. T. (2013). A Platform for High-Speed Biomechanical Analysis Using Wearable Wireless Sensors. Doctor of Philosophy in Media Arts and Sciences, Massachusetts Institute of Technology.

Leardini, A., L. Chiari, U. Della Croce and A. Cappozzo (2005). "Human movement analysis using stereophotogrammetry: Part 3. Soft tissue artifact assessment and compensation." Gait & posture **21**(2): 212-225.

Li, Q. and J. T. Zhang (2014). "Post-trial anatomical frame alignment procedure for comparison of 3D joint angle measurement from magnetic/inertial measurement units and camera-based systems." Physiol Meas **35**(11): 2255-2268.

Lin, J. F. S. and D. Kulic (2012). "Human pose recovery using wireless inertial measurement units." Physiological Measurement **33**(12): 2099-2115.

Luinge, H. J., P. H. Veltink and C. T. Baten (2007). "Ambulatory measurement of arm orientation." Journal of biomechanics **40**(1): 78-85.

Madgwick, S. O. (2010). "An efficient orientation filter for inertial and inertial/magnetic sensor arrays." Report x-io and University of Bristol (UK).

Madgwick, S. O., A. J. Harrison and R. Vaidyanathan (2011). Estimation of IMU and MARG orientation using a gradient descent algorithm. 2011 IEEE International Conference on Rehabilitation Robotics, IEEE.

Markley, F. L. (1980). ParameterizationoftheAttitude. SpacecraftAttitude Determination and Control. J. R. Wertz. **Dordrecht, The Netherlands**, D. Reidel publishing company**:** 414–416.

Markley, F. L. (2008). "Unit quaternion from rotation matrix." Journal of guidance, control, and dynamics **31**(2): 440-442.

McConville, J. T., C. E. Clauser, T. D. Churchill, J. Cuzzi and I. Kaleps (1980). Anthropometric relationships of body and body segment moments of inertia, DTIC Document.

O'Donovan, K. J., R. Kamnik, D. T. O'Keeffe and G. M. Lyons (2007). "An inertial and magnetic sensor based technique for joint angle measurement." Journal of biomechanics **40**(12): 2604-2611.

Palermo, E., S. Rossi, F. Marini, F. Patane and P. Cappa (2014). "Experimental evaluation of accuracy and repeatability of a novel body-to-sensor calibration procedure for inertial sensor-based gait analysis." Measurement **52**: 145-155.

Reed, M., M. A. Manary and L. W. Schneider (1999). Methods for measuring and representing automobile occupant posture, SAE Technical Paper.

Roetenberg, D., H. Luinge and P. Slycke (2009). "Xsens MVN: full 6DOF human motion tracking using miniature inertial sensors." Xsens Motion Technologies BV, Tech. Rep.

Rogowski, I., T. Creveaux, L. Chèze, P. Macé and R. Dumas (2014). "Effects of the Racket Polar Moment of Inertia on Dominant Upper Limb Joint Moments during Tennis Serve." PLoS ONE **9**(8): e104785.

Salehi, S., G. Bleser, A. Reiss and D. Stricker (2015). Body-IMU autocalibration for inertial hip and knee joint tracking. Proceedings of the 10th EAI International Conference on Body Area Networks, ICST (Institute for Computer Sciences, Social-Informatics and Telecommunications Engineering).

Schauer, T. and T. Seel (2016). Alignment-free, self-calibrating elbow angles measurement using inertial sensors. 2016 IEEE-EMBS International Conference on Biomedical and Health Informatics (BHI), IEEE.

Schrauwen, M. (2015). OptiTrack Handleiding. H. hoogschool. The Hage, Bewegingstechnologie.

Seel, T. (2016). Learning control and inertial realtime gait analysis in biomedical applications, Improving Diagnosis and Treatment by Automatic Adaption and Feedback Control. PHD, Technischen Universität Berlin.

Seel, T., J. Raisch and T. Schauer (2014). "IMU-based joint angle measurement for gait analysis." Sensors (Basel) **14**(4): 6891-6909.

Seel, T., T. Schauer and J. Raisch (2012). Joint axis and position estimation from inertial measurement data by exploiting kinematic constraints. Control Applications (CCA), 2012 IEEE International Conference on, IEEE.

Shimmer (2014). IMU User Guide. R. T. Ltd, Shimmer.

Song, S., B. Li, W. Qiao, C. Hu, H. Ren, H. Yu, Q. Zhang, M. Q.-H. Meng and G. Xu (2014). "6-D magnetic localization and orientation method for an annular magnet based on a closed-form analytical model." IEEE Transactions on Magnetics **50**(9): 1-11.

Takeda, R., S. Tadano, A. Natorigawa, M. Todoh and S. Yoshinari (2009). "Gait posture estimation using wearable acceleration and gyro sensors." Journal of Biomechanics **42**(15): 2486-2494.

Takeda, R., S. Tadano, M. Todoh, M. Morikawa, M. Nakayasu and S. Yoshinari (2009). "Gait analysis using gravitational acceleration measured by wearable sensors." Journal of Biomechanics **42**(3): 223-233.

Thalmann, N. M. and D. Thalmann (1993). Models and Techniques in Computer Animation, Springer.

van den Noort, J. C., A. Ferrari, A. G. Cutti, J. G. Becher and J. Harlaar (2013). "Gait analysis in children with cerebral palsy via inertial and magnetic sensors." Medical & biological engineering & computing **51**(4): 377-386.

van der Helm, F. C. and G. M. Pronk (1995). "Three-dimensional recording and description of motions of the shoulder mechanism." Journal of biomechanical engineering **117**(1): 27-40.

Wang, L., Z. Zhang and P. Sun (2015). "Quaternion-based Kalman filter for AHRS using an adaptive-step gradient descent algorithm." International Journal of Advanced Robotic Systems **12**.

Woodman, O. J. (2007). "An introduction to inertial navigation." University of Cambridge, Computer Laboratory, Tech. Rep. UCAMCL-TR-696 **14**: 15.

Wu, G. and P. R. Cavanagh (1995). "ISB recommendations for standardization in the reporting of kinematic data." J Biomech **28**(10): 1257-1261.

Wu, G., S. Siegler, P. Allard, C. Kirtley, A. Leardini, D. Rosenbaum, M. Whittle, D. D D'Lima, L. Cristofolini and H. Witte (2002). "ISB recommendation on definitions of joint coordinate system of various joints for the reporting of human joint motion—part I: ankle, hip, and spine." Journal of biomechanics **35**(4): 543-548.

Wu, G., F. C. Van Der Helm, H. D. Veeger, M. Makhsous, P. Van Roy, C. Anglin, J. Nagels, A. R. Karduna, K. McQuade and X. Wang (2005). "ISB recommendation on definitions of joint coordinate systems of various joints for the reporting of human joint motion—Part II: shoulder, elbow, wrist and hand." Journal of biomechanics **38**(5): 981-992.